Micromagnetic Study of Composite Media for High Density Heat Assisted Magnetic Recording

A DISSERTATION
SUBMITTED TO THE FACULTY OF THE GRADUATE SCHOOL
OF THE UNIVERSITY OF MINNESOTA
BY

ZENGYUAN LIU

IN PARTIAL FULFILLMENT OF THE REQUIREMENTS
FOR THE DEGREE OF
DOCTOR OF PHILOSOPHY

RANDALL H. VICTORA, ADVISOR

JUNE, 2017

Acknowledgements

First of all, I want to thank my advisor, Professor Randall Victora. He shows me the world of magnetic recording and magnetic materials. His insightful observation and profound knowledge inspire me to find the beauty of truth. He always offers valuable suggestions and comments on my research. He is patient with me and my research progress which make me gain deep understanding about my research goal. These encourage me a lot as a young researcher. I know how to be a researcher who should be strict, passionate and active with everything you are doing. I believe all these will benefit me in the future.

I also would like to thank Prof. Bethanie Stadler, Prof. Jianping Wang, Prof. Randall Victora and Prof. Xiaojia Wang, for their time and efforts on serving in my committee.

Here, I want to thank my manager Ganping Ju and my mentor Pin-Wei Huang during my two summer internships at Seagate Fremont Research Center. Their help, trust and encouragement help me starting my career in the magnetic recording industry successfully.

During my stay at University of Minnesota, I really have a good time with my colleagues at the MINT center. I want to give my thanks to Tao Qu, Ali Ghoreyshi, Rizvi Ahmed, Ziran Wang, Xiaowei Zhang, Yinglong Feng, Kai Wu, Yipeng Jiao, Zhengyang Zhao, Hongshi Li, Yang Lv, Wei-Heng Hsu, Niranjan Natekar, Aneesh Venugopal, and many other friends for their suggestions, help and comments.

I would like to thank Seagate Technology for funding.

Lastly, I would like to thank my wife, parents-in-law and my parents. Without their love, support and advice, I would have never gone so far.

Dedication

With gratitude to my parents and my wife.

Abstract

The hard disk drive industry is a market with around 25 billion revenue each year. The annual average areal density growth rate is about 40% before 2012. With cloud computing and storage technology emerge, hard disk drives with high area density and low price are required. However, the areal density of current perpendicular magnetic recording technology tends to saturate at 1 Tb/in^2. Therefore, new technologies like Heat Assisted Magnetic Recording (HAMR) are needed. On the other hand, the Solid State Drive (SSD) has developed quickly as another candidate for high density and high speed information media which makes this situation urgent. In this thesis, micromagnetic simulations of HAMR media are conducted based on the renormalized Landau-Lifshitz-Gilbert (LLG) method. $L1_0$ FePt is one promising recording media candidate for HAMR. The transition noise and transition jitter are calculated through magnetic recording simulation accelerated by GPU parallel computing. Thermal fluctuations and Curie temperature variance are verified to be two import noise sources for FePt recording media besides the grain size distribution and anisotropy variance. A more easily implemented method called thermal switching probability distribution (SPD) is proposed. It can provide two important factors for evaluating the recording performance: σ_{SPD} and write temperature. Under a certain fabrication technology (certain average grain size), the transition jitter can be estimated by σ_{SPD}. Furthermore, the grain volume dependence of σ_{SPD} and write temperature are investigated. The dependence follows $1/V$ and $1/\sqrt{V}$ power law respectively. This knowledge greatly helps the noise analysis and new media design. To mitigate the noise from thermal fluctuations and Curie temperature variance, a new composite media design

based on a bilayer structure with two different Curie temperatures is proposed. The substantial anisotropy of the write layer differentiates this design with respect to previous work. This ensures that the composite structure has small transition noise and high areal density. The user density can reach 3.4 Tb/in^2 under traditional recording and 4.7 Tb/in^2 with shingled magnetic recording (SMR) technology. The interlayer exchange coupling effects are found to affect the energy barrier during the dynamic recording process. Both the thermal effects and write temperature can be tuned by optimizing the interlayer exchange coupling effects. Further research verified that this is due to the linear temperature dependence of energy barrier at temperatures close to Curie temperature. More research need to be done to offer a good explanation of the high areal density achieved by PMR-ECC-like structure for HAMR. Possible directions include the effective field temperature gradient and switching speed during the recording process as the temperature changes.

Table of Contents

List of Tables

List of Figures

Chapter 1

Introduction

Electronic information storage has been attracted people's attention since the first computer named Electronic Numerical Integrator And Computer (ENIAC) was made in 1946. Because the calculation process always creates data which needs to be stored for future retrieving. As early as 1956, 10 years after ENIAC appeared, International Business Machines (IBM) created the first general-purpose commercial computer (RAMAC) to feature magnetic disk storage. The system's magnetic disk memory unit had storage capacity of 5 megabytes with 1200 revolutions per minute. Beginning in the late 1960s, the Internet began to enter people's life. The connection via TCP/IP created a huge amount of data. The demand for high density information storage devices expanded greatly. The hard disk drive (HDD) met this demand and became a commercialized magnetic storage industry. Based on market statistics, in Q3 of 2016, the shipment of hard disk devices reached as high as 115 million units. In 2016, the HDD industry had a history of over 60 years. Today, cloud computing and storage have entered Big Data. This technology will also act as brains for the artificial intelligence of the future. On the other hand, the internet

creates more data than ever before which requires companies, like Facebook, Google and Amazon, to build data centers. However, both the cost and areal density of HDD tend to saturate with increasing demands for suitable storage devices. Furthermore, in 2015, the Solid State Drive (SSD) begin to play a role in storage media for mobile devices like personal computers (PCs), tablet and cell phones. It would be no exaggeration to say that the hard disk industry is experiencing one of the most challenging situations. The future goal of HDD is to further increase areal density and decrease cost.

1.1 Current HDD Industry

Figure 1.1 shows the product performance and development history of HDD industry. The figure on the top left shows the $/Gbpsi versus time. The “Gbpsi” stands for Gb per square inch. This evaluation parameter describes the cost of information storage. By increasing the number of hard disk drives, the storage capacity can be increased. At the same time, the areal density also need to be improved by new technology and process development. By striking a balance between these two factors, the cost per bit needs to be considered. After so many years of product development, the cost per bit tends to saturate around 0.05/Gbpsi. The other figure shows that there are a tremendous number of inventions and techniques which have contributed to increasing the areal density. This ensures the fast growth of the HDD industry. From year 1956 to year 2007, the annually average growth rate of HDD areal density is about 60%. In 2007, the Nobel Prize in Physics was awarded to the Giant Magnetoresistance (GMR). It achieved great success in the HDD industry by improving the signal sensitivity in high areal density storage. In 2005, the HDD industry

was experiencing a transition from longitudinal magnetic recording (LMR) to perpendicular magnetic recording (PMR). With the help of GMR, PMR, exchange coupled media (ECC) and shingled magnetic recording (SMR), the annual average growth rate of areal density has maintained 40% since 2007. After 2010, the annual average growth rate has slowed down and the areal density tends to saturated around 1 Tb/in^2.

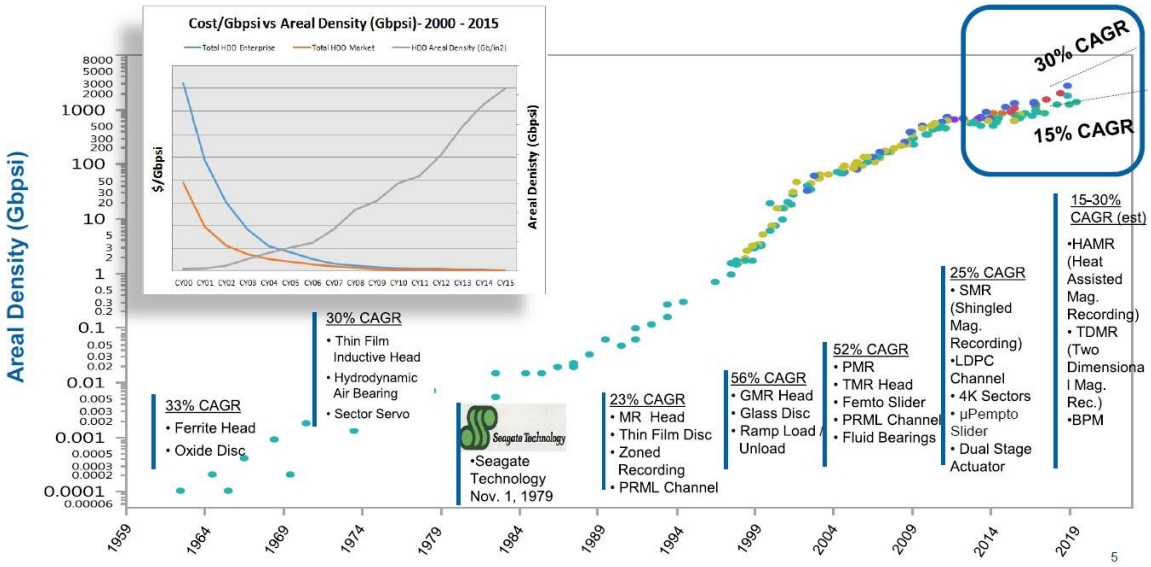

Fig. 1.1 The evolution of product performance and development history of HDD industry

As we have talked about, with the development of cloud storage and cloud computing, data centers have been built to meet the requirement of data storage from the internet company. For example, the Google cloud provides cloud storage services. The Amazon Web Services (AWS) provides cloud computing services. The Cloud concept starts to change our life. The cost of data centers mainly focus on two aspects. One counts on the evaluation parameter $/Gbpsi mentioned above. The other one is the power efficiency. Each data

center will have thousands of hard disk drives, the electricity charges represent part of the cost of operation. The main reason that HDD occupies the cloud storage market (stores 90% of the information in today's data center) is the outstanding performance in $/Gbpsi. Companies like Seagate and WD are two HDD providers of cloud storage solutions. Recently, the Solid State Drive (SSD) developed quickly due to fast data processing speed and high density comparable to the HDD. The "hot" data which need to be transferred frequently through Internet to local devices are stored in the SSD. Figure 1.2 shows the comparison of areal density of SDD and HDD over recent years.

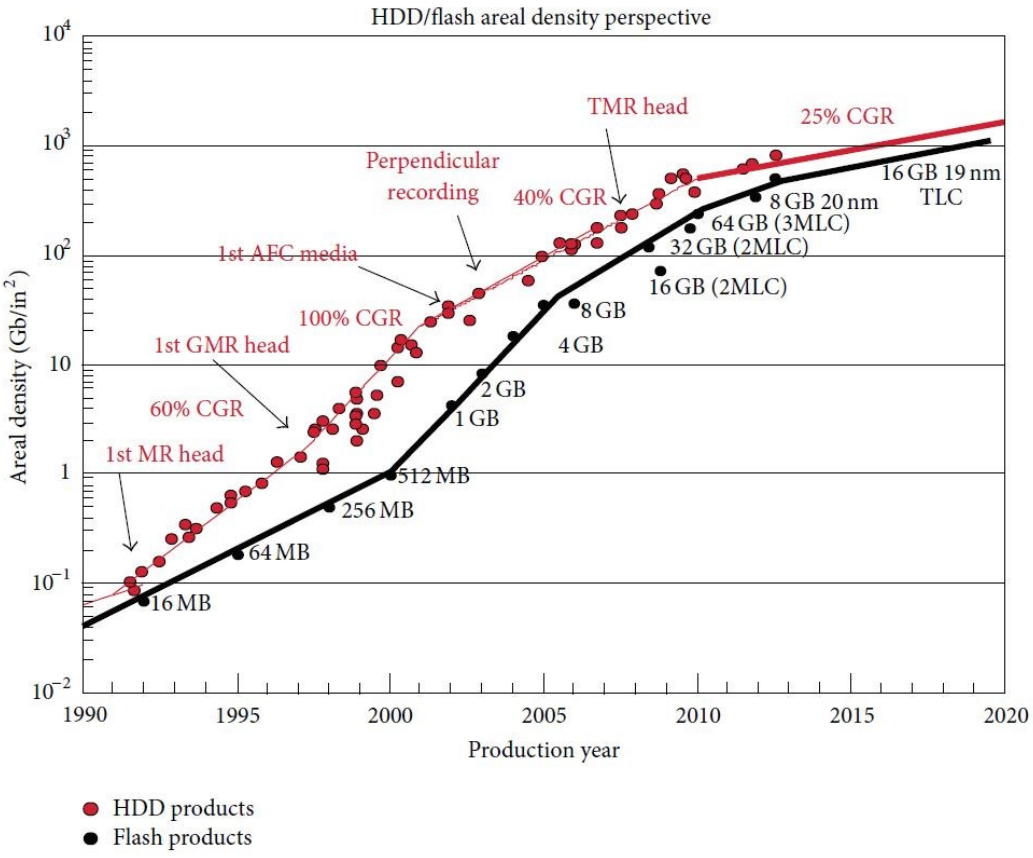

Fig. 1.2 The comparison of areal density of SDD and HDD over years.

Figure 1.2 shows that both the areal density of SSD and HDD tend to saturate. The areal density of SSD starts to catch up with that of HDD after 2015. To date, in terms of $/Gbpsi, the HDD still outperforms the SDD products. Inspired by the potential market brought by SSD, in 2016, Seagate released the world largest SSD product with surprising storage capacity of 60 TB. In 2015, Western Digital acquired SandDisk who is a global leader of flash memory (SSD) storage solutions. Seagate also take a step forward to integrate SSD and HDD together by creating hybrid drives. This hybrid drives, which offers high data storage/retrieving speed and low-cost high storage capacity, can make use of advantages of SSD and HDD separately. It has been commercialized and put into market.

Being limited by areal density saturation of current HDD technology, facing the challenges brought by SSD products and increasing demands of low-cost higher areal density from cloud storage and computing, new technology is needed for the HDD industry. Heat Assisted Magnetic Recording (HAMR) is taken as the most promising technology that can bring light to the HDD industry. Based on the roadmap (Figure 1.3) presented by Advanced Storage Technology Consortium (ASTC), the areal density of HAMR-based HDD technology will reach 2 Tb/in^2 in around 2019. The areal density growth rate can reach 30% with the new magnetic recording technology such as HAMR, Bit Patterned Magnetic Recording (BPMR) and Heated Dot Magnetic Recording (HDMR). The shingled magnetic recording (SMR) allows the recorded track width to be smaller than the recording head width. If there are certain overlaps for two adjacent tracks, the information can still be accurately recorded. To avoid the effects from adjacent tracks, two dimensional magnetic recording (TDMR) needs to be implemented. Both TDMR and SMR technology can

further increase the areal density of the current PMR product. The rest of this chapter focus on several important parts of the magnetic recording technology and its development. Firstly, the transition from longitudinal magnetic recording (LMR) to perpendicular magnetic recording (PMR) is summarized. Then, the well-known exchanged coupled composite media (ECC media) for perpendicular magnetic recording is summarized.

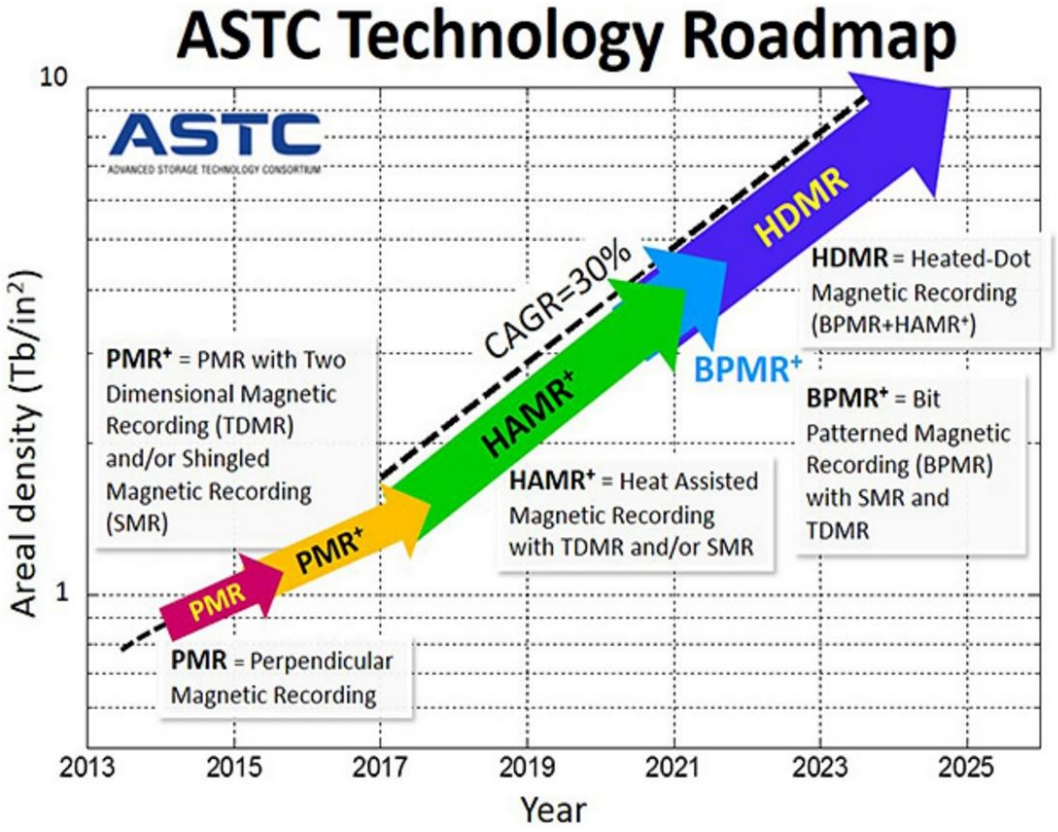

Fig. 1.3 Areal density roadmap of hard disk drive presented by Advanced Storage Technology (ASTC).

1.2 From LMR to PMR

Perpendicular magnetic recording (PMR) can provide higher recording density with low cost and good stability than longitudinal magnetic recording (LMR). Therefore, the magnetic recording technology transferred from longitudinal magnetic recording to perpendicular magnetic recording in around 2005. The implementation of a monopole head, the soft under layer (SUL) and development of a CoCrPt media fabrication process contributed to this successful technology evolution. Figure 1.4 shows the configuration of a perpendicular magnetic recording media.

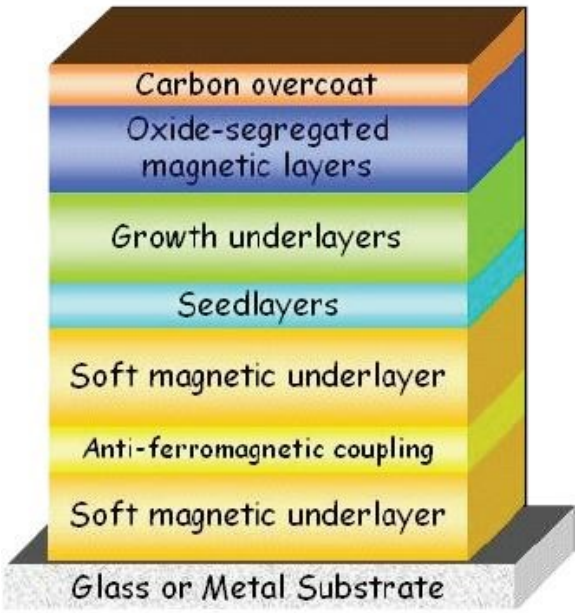

Fig. 1.4 The configuration of PMR media with a single storage layer marked as oxide-segregated magnetic layers. The carbon over coat layer is used for protecting the head-disk interface.

Fig. 1.5 (a) and (b) aim to show the differences between longitudinal magnetic recording and perpendicular magnetic recording. The big difference lies in the direction of the

magnetized spins after the information is stored. For longitudinal magnetic recording, the magnetization aligns in-plane direction. However, for perpendicular magnetic recording, the magnetization is perpendicular to in-plane direction.

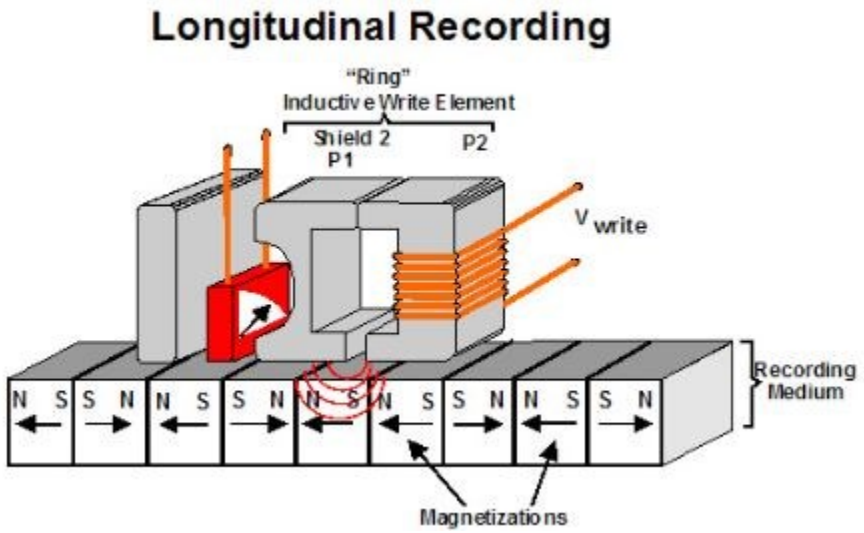

Fig. 1.5 (a) Schematic view of LMR recording system

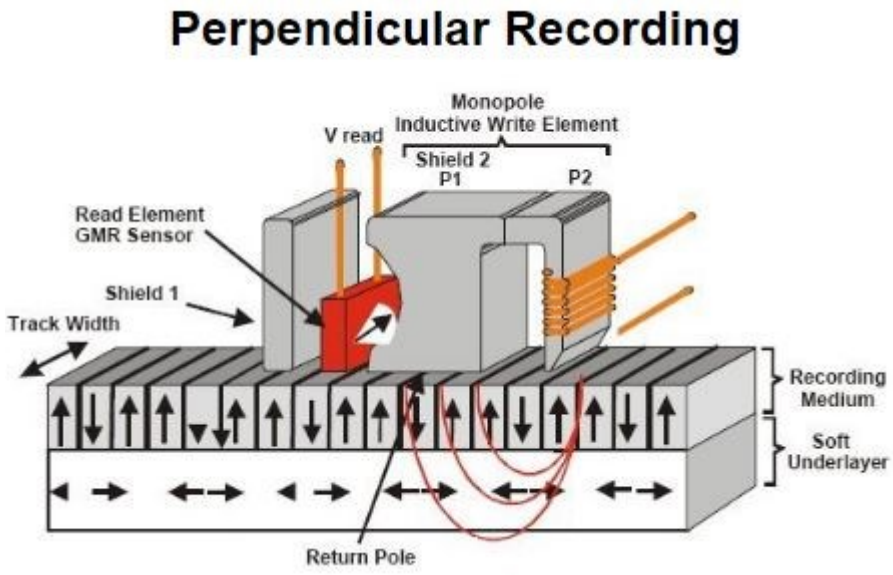

Fig. 1.5 (b) Schematic view of PMR recording system

The recording material of either perpendicular magnetic recording or longitudinal magnetic recording can be permanently magnetized, which allows the information to be stored magnetically. To meet the requirement of magnetization direction in longitudinal magnetic recording, the "ring" recording head which is basically an electromagnet with a gap is used. It needs to be located near the media. For perpendicular magnetic recording, the magnetization direction requirement is solved by forming a close loop of magnetic flux through the monopole recording head, magnetic storage media and the soft under-layer (SUL). The closed loop helps stabilizing the information that has been magnetically stored and strengthening the read back signals. Generally, the soft under layer tends to have large magnetization. The monopole recording head include a tip pole and a return pole. The magnetic field is intense in the short gap between the pole tip and soft under-layer. This helps increase the achieved magnetic field magnitude which may allow the further decrease of the grain size.

In the history of magnetic recording, new technologies pushed this industry forward. The areal density is increased with decreased price of magnetic storage devices. The magnetic recording technology has maintained its prosperity since 1956. In the years before 2003, perpendicular magnetic recording technique (PMR) encountered the magnetic recording trilemma with continuously increasing areal density. "Trilemma" means three conflicting requirements [1] including the media SNR, thermal stability and write-ability shown in figure 1.6. Here, H_c is the switching field or coercivity field. H_{head} is the magnetic field provided by magnetic poles of the recording head. The SNR is the signal-to-noise ratio. N is the number of grains per bit. K_u is the anisotropy. V is the grain volume of the media.

k_B is the Boltzmann constant. T is the temperature at which the information is stored. Higher recording density requires smaller bits. To maintain reasonable SNR, the grain volume V should be smaller if N represents a sufficient number of grains. However, this will deteriorate the thermal stability defined by $K_u V / K_B T$. For instance, if the stored information is required to be stable for 10 years, this ratio should be larger than 60. Therefore, to further improve the areal density, the anisotropy K_u needs to be increased. But this increase will induce higher H_c which makes write-ability worse. The maximum magnetic field that can be achieved by magnetic recording head is limited by the material. Therefore, this trilemma limits further increase of magnetic recording density.

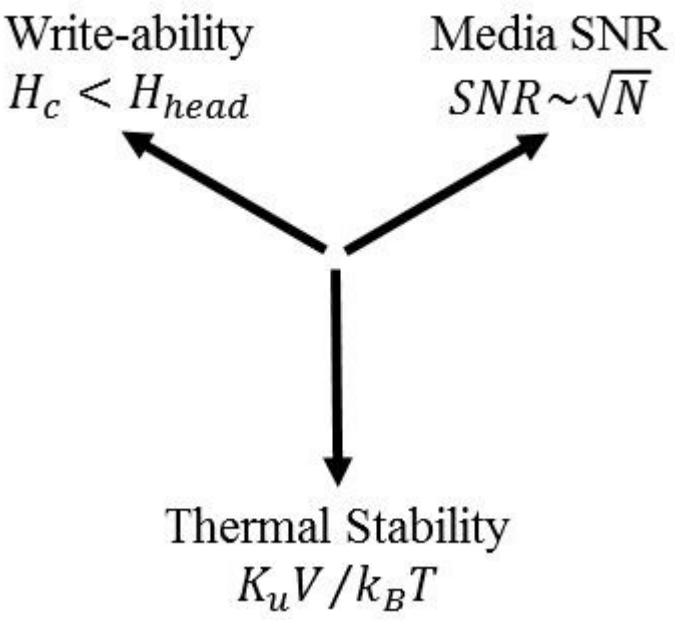

Fig. 1.6 The magnetic recording trilemma for magnetic recording media design.

1.3 Exchanged Coupled Composite Media for PMR: ECC

Based on the history of magnetic recording industry, many advances can be regarded as different approaches to breaking the trilemma or resolving the contradictions within these three requirements. The exchanged coupled composite media (ECC media) with a magnetically hard and soft layer was the breakthrough made for perpendicular magnetic recording. The ECC media breaks the magnetic recording trilemma by substantially decreasing the switching field, which is mainly determined by the anisotropy of the hard layer, of the composite media. In other words, the ECC media yields a significant increase of maximum switchable anisotropy for a fixed applied field. This will greatly enhance the energy barrier to thermal fluctuations. This also means that the grain size reduction is possible with higher anisotropy. Hence it results in areal density improvement.

To better analytically describe the total effects from switching field and energy barrier, the definition of ratio $\xi = 2\Delta E / M_s H_s V$ aims to separate thermal stability and write-ability. Bigger ratio means higher recording density. ΔE is the energy barrier to thermal fluctuations. H_s is the switching field which is the magnetic field necessary to switch the magnetization. In the history of perpendicular magnetic recording, new media designs tried to follow the essence of the ξ definition which is the consideration that thermal stability and write-ability relate to two different processes. One is the recording process. The other is the storage issue. The media design principle aims to decrease the switching field while maintaining thermal stability. In around 2003, two groups proposed the idea of tilted media where the easy axis points at $\pi/4$ to the perpendicular direction [2] [3]. The tilted media

has lower switching field with increased anisotropy. Ideally for a single grain with perpendicular easy axis, the ratio ξ has value of one. By using tilted media, it is increased to two. However, the impractical fabrication process limited the further development of tilted media. In early 2004, about one year later after the tilted media was proposed, both Victora's group and Suess's group proposed the exchanged coupled composite media for perpendicular magnetic recording independently [4] [5] [7]. Shen and Wang's group did the first experiment demonstration at the same time. [6] Figure 1.7 shows the design concept of exchange coupled composite media [4]. It was proposed for 1 Tb/in^2 perpendicular magnetic recording.

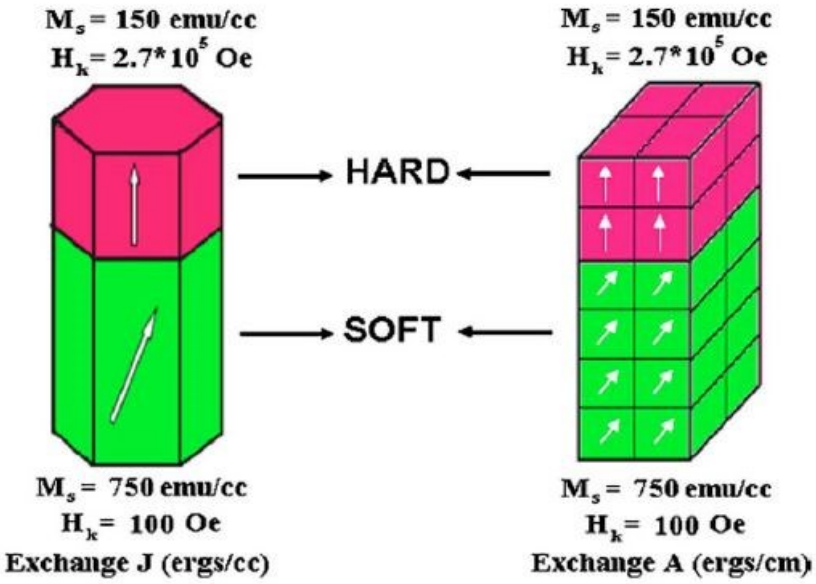

Fig 1.7 shows the version proposed by Victora and Shen. The left one is the two spin model. The right one is the discretized model for micromagnetic simulation.

The exchanged coupled composite media consists of magnetically soft (low anisotropy) and hard (high anisotropy) materials. The magnetically hard layer with high anisotropy

provides good thermal stability which also means a large energy barrier ΔE. When the soft layer experiences the reversible switching under applied magnetic field, the quantum mechanical exchange coupling between these two layers exerts a magnetic torque to the magnetic spin of the hard layer. Therefore, the soft layer assists the switching of the hard layer which decreases the switching field of the composite media. Therefore, the composite media is predicted to increase the ratio ξ. The switching field reduction of hard/soft layer was firstly found by Aharoni who tried to find a mechanism to explain Brown's paradox [8]. He found that the switching field can be decreased by 4 times for an abrupt anisotropy field change at the hard/soft interface and a further switching field reduction for a structure with linearly decreasing anisotropy field [4].

In 2008, Victora and Shen reviewed the previous work about the exchange coupled composite media since it was firstly proposed in 2004 [4]. In this review, the optimization of the composite media was investigated. It involves carefully chosen ratio $M_{ss}t_s / M_{sh}t_h$ where M_{ss} and M_{sh} are magnetization of soft and hard layers. t_s and t_h are thickness of both layers. Bigger ratio of $M_{ss}t_s / M_{sh}t_h$ tends to offer bigger value of ξ. The ratio of K_{uh} / K_{us} can also affect ξ. K_{uh} and K_{us} are the anisotropy of hard and soft layers. The ξ is continuously increased before K_{uh} / K_{us} reaches 10 times. By using optimal magnetic property combinations, the value of ξ can be increased to two from one. It has also been reported that slight intergranular exchange helps cancel magnetostatic fields and increases the thermal stability of the media. The switching field calculation shows lower dependence of coercivity on applied magnetic field angle with easy axis comparing to Stoner-Wolfarth

model (Figure 1.8). This improves the cross-track performance which may increase the signal-to-noise ratio (SNR). The optimization of ξ shows that the thermal stability and switching field can be tuned separately.

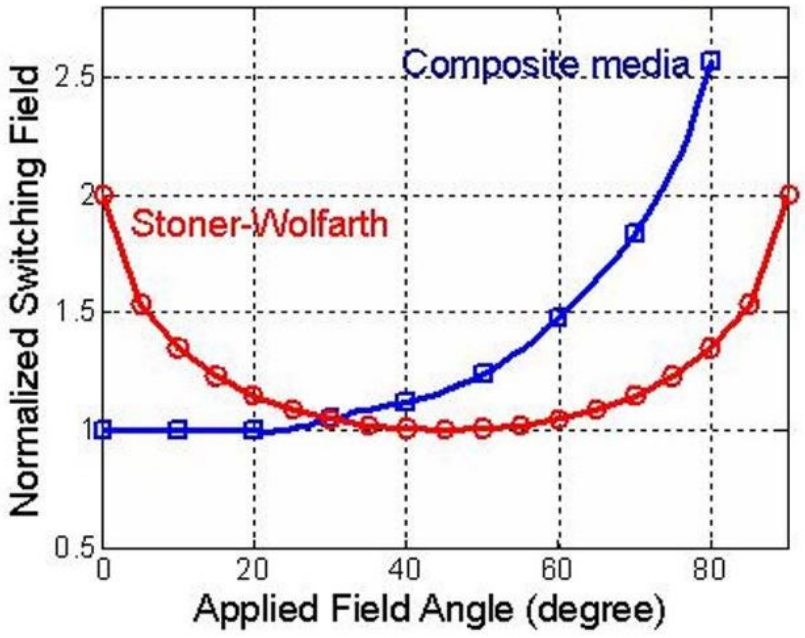

Fig. 1.8 Switching field angular dependence versus applied field angle.

In the 1990s, the exchange spring magnets were investigated. The soft layer with high magnetization is exchanged coupled to the hard layer with low magnetization. This work was done for permanent magnets. Earlier work also tried to get analytical expression of coercivity field [10] [11]. The assumption made was that the thickness of both layers are infinite. Based on the continuum theory of micromagnetism shown in Figure 1.9, the coercivity field is obtained after complicated mathematic derivation (equation 1.1). The

superscripts or subscripts stand for two different phases with different magnetic properties including magnetization, anisotropy and exchange constant.

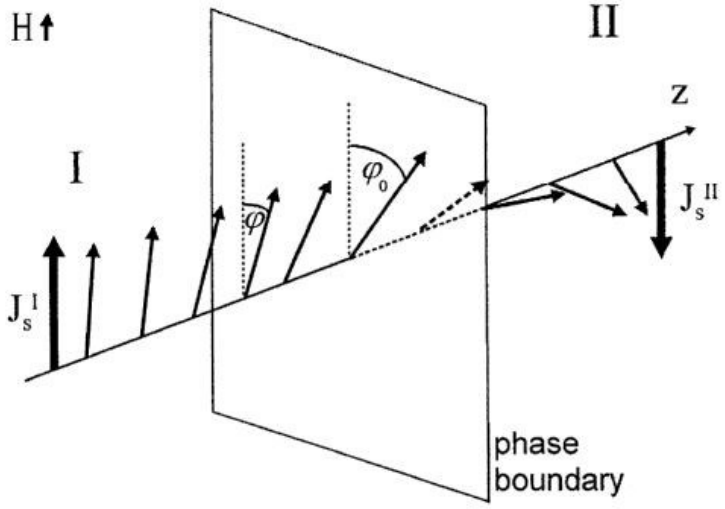

Fig. 1.9 Spin configuration of a domain wall pushed by an applied field against the phase boundary.

$$H_C = \frac{2K_1^{II}}{J_s^{II}} \frac{1-\varepsilon_K \varepsilon_A}{(1-\sqrt{\varepsilon_A \varepsilon_J})^2} \qquad 1.1$$

Here, the ratios are

$$\varepsilon_A = \frac{A_I}{A_{II}}, \quad \varepsilon_J = \frac{J_s^I}{J_s^{II}}, \quad \varepsilon_K = \frac{K_1^I}{K_1^{II}}$$

A. Yu. Dobin proposed the domain wall assisted switching mechanism for the PMR magnetic recording ECC media (Figure 1.10). The coercivity reduction is due to domain

wall motion at the hard/soft interface [12] [13]. This reduction is bad for permanent magnetics, but magnetic recording media can benefit from it.

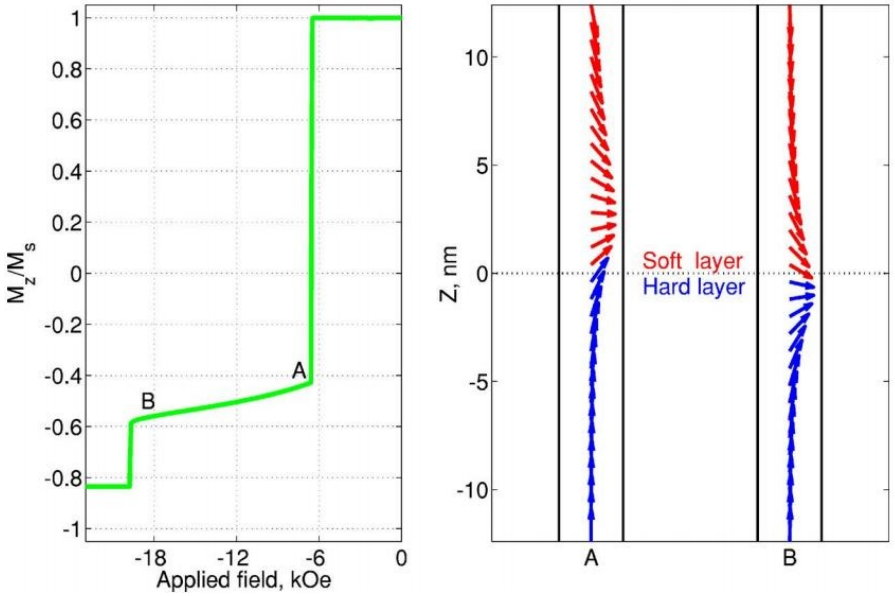

Fig. 1.10 M-H loop and magnetization configuration for hard/soft composite film [12].

In 2005, Suess proposed a similar argument to show the benefits of the perpendicular magnetic recording ECC media based on the domain wall theory and coercivity reduction [14] [15]. They called this exchange spring media. Based on their simulation results, the energy barrier can be increased by factor of 2. Furthermore, the energy barrier tends to decrease with less exchange coupling between soft/hard layers. Regarding low angular dependence shown by Victora and Shen, Suess mentioned that the interfacial behavior of the exchange spring media is controlled by the domain-wall pinning. Based on the Stoner-Wohlfarth model, the single-phase media shows strong angular dependence of the coercivity. However, for domain-wall pinning, the angular dependence of the coercive field follows $H_c(\alpha) = H_c(0)/\cos(\alpha)$. If the applied field angle α is from 0° to 40°, the

deviation of coercivity is less than 5%. When the applied field exceeds the coercive field, the domain wall depins from the interface and propagates through the hard layer.

Since the exchange coupled media was proposed for the perpendicular magnetic recording, it has achieved great success in the hard disk industry for the past 12 years. The current PMR recording media benefits from the basic principles of the exchange coupled composite media. As shown in Figure 1.11, the commercial PMR multilayer media will include COC layer, cap layer, exchange coupled layer (ECL), storage layer and SUL. [16]

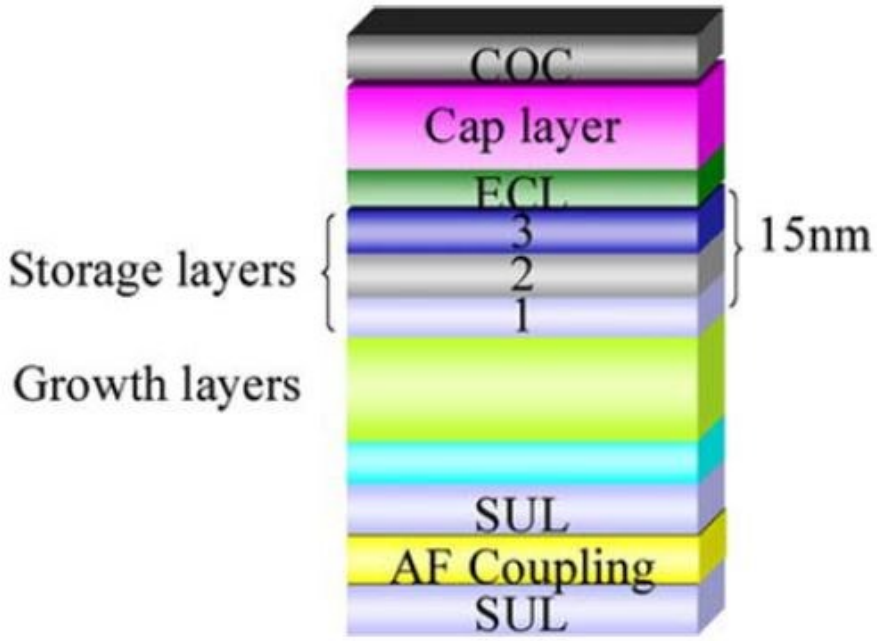

Fig. 1.11 The schematic view of current multilayer media structure for PMR product

The SUL layer is the soft under layer to stabilize the magnetization of storage layer. The COC layer is carbon overcoat layer used to protect the cap layer. The thickness of the

exchange coupled layer is used for tuning the exchange coupling strength between cap layer and storage layer. The optimization of exchange coupling strength is required to maximize the performance of the composite media by modifying the switching behavior of both layers. The cap layer acts as the magnetically soft layer of the composite media. It has low anisotropy. Besides the ECC effects, there exists the CGC effects provided by the lateral exchange coupling of the cap layer. The practical way to adjust the CGC effects is changing the thickness of the cap layer. It is well known now that the lateral exchange coupling in the cap layer will improve the write-ability. However, in turn, the lateral exchange tends to increase the cluster size which will deteriorate the signal-to-noise ratio (SNR).

By making use of the exchanged coupled media and many other techniques (optimization) at system level, current recording density of perpendicular magnetic recording density tends to reach 1 Tb/in^2. To date, Western Digital released 12 TB hard disk drive (HDD) product by using Helium technology in late 2016. This beats the product (10 TB) released by Seagate Technology previously. Seagate Technology plans to get 18 TB HDD drives into the market in the next 18 months.

1.4 Summary

The current HDD industry is overviewed by presenting the challenges and opportunities. The technology transition from LMR to PMR is introduced. The magnetic trilemma is shown to be an important rule to break when designing new recording media. The basic principles, history and success of exchange coupled composite media are summarized.

Chapter 2

Heat Assisted Magnetic Recording

Even with exchanged coupled composite media, the areal density of perpendicular magnetic recording will likely saturate in 2020. Heat Assisted Magnetic Recording (HAMR) is considered as the most promising candidate for the next generation hard disk industry. Comparing to exchange coupled composite media, HAMR also tries to break the magnetic recording trilemma by reducing the switching field and provide good thermal stability. However, the ECC media reduced the switching field by introducing the magnetically soft layer. The HAMR technology reduces the switching field of the high anisotropy material by a local heating process provided by a laser.

2.1 Heat Assisted Magnetic Recording System Overview

Figure 2.1 shows the overview of the HAMR system [17]. The development of novel parts for HAMR involve the light delivery system, the writer integrated with a near field transducer (NFT), a robust head disk interface and high areal density recording media. The

other components, like the slider's fabrication, the air bearing system and the magnetoresistive reader are similar to those used for current PMR product.

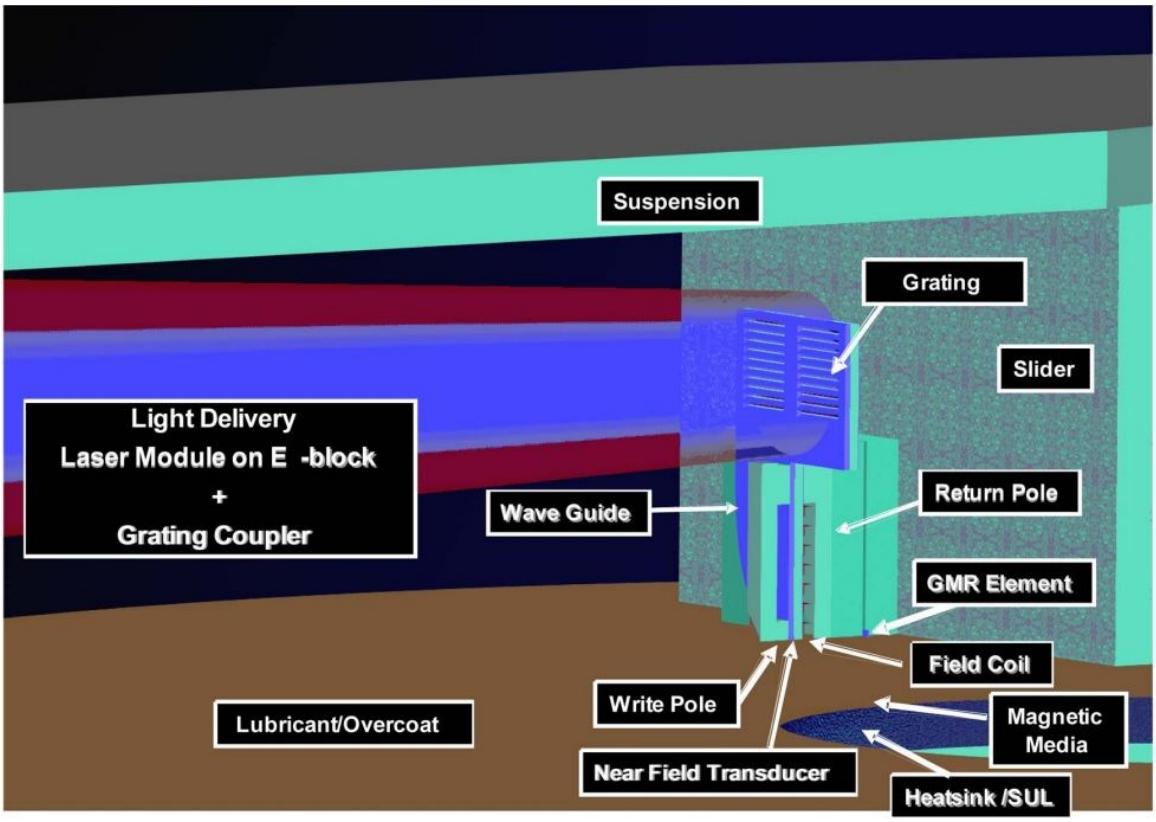

Fig. 2.1 Schematic overview of HAMR recording system

Being different from perpendicular magnetic recording, HAMR needs the laser to provide heat and magnetic field to encode the information "1" and "0". For HAMR, the bit size is limited by the spot size created by laser on the media. However, there exists the diffraction limit which limits further increase of areal density. The diffraction limit of a focusing lens can be calculated by equation (2.1).

$$d = \frac{0.51\lambda}{NA} \tag{2.1}$$

Here, λ is the wavelength and NA is the numerical aperture of the light at the location of focusing lens. The resulting spot size is evaluated by d. For example, even we use the laser in today's DVD Blue-Ray with wavelength of 405 nm and NA of the focusing objective of 0.85. The corresponding spot size is around 240 nm. It is impossible for such a system to achieve areal density higher than 1 Tb/in^2. A 30nm~60nm bit size along cross track direction is needed. One reasonable assumption when considering the bit size is that magnetic field distribution region is much larger than temperature distribution generated by NFT on the media. This means the spot size generated by the laser on the media should be around 30 nm ~ 60nm. The surface plasmon can offer helps here.

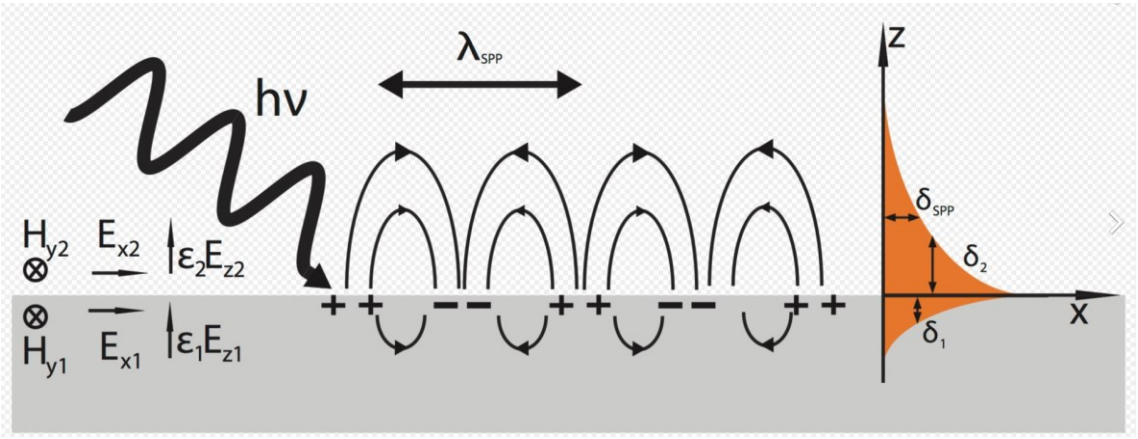

Fig. 2.2 Schematic view of the concept of surface plasma effects [Wikipedia].

A lot of work have been done based on the surface plasmon effects which can break the diffraction limit and provide narrow spot size. Figure 2.2 shows the concept of the surface plasmon. We can understand this effect by imagining that there is AC current at the metal surface. The current design of NFT is similar to the one proposed in reference [18]. They use a gold disk with a peg close to the media. A planar solid immersion mirror with dual grating is used to focus light (waveguide mode) on the NFT. The peg generated small spot size on the media. The general structure of a planar solid immersion mirror and NFT is shown in Figure 2.3.

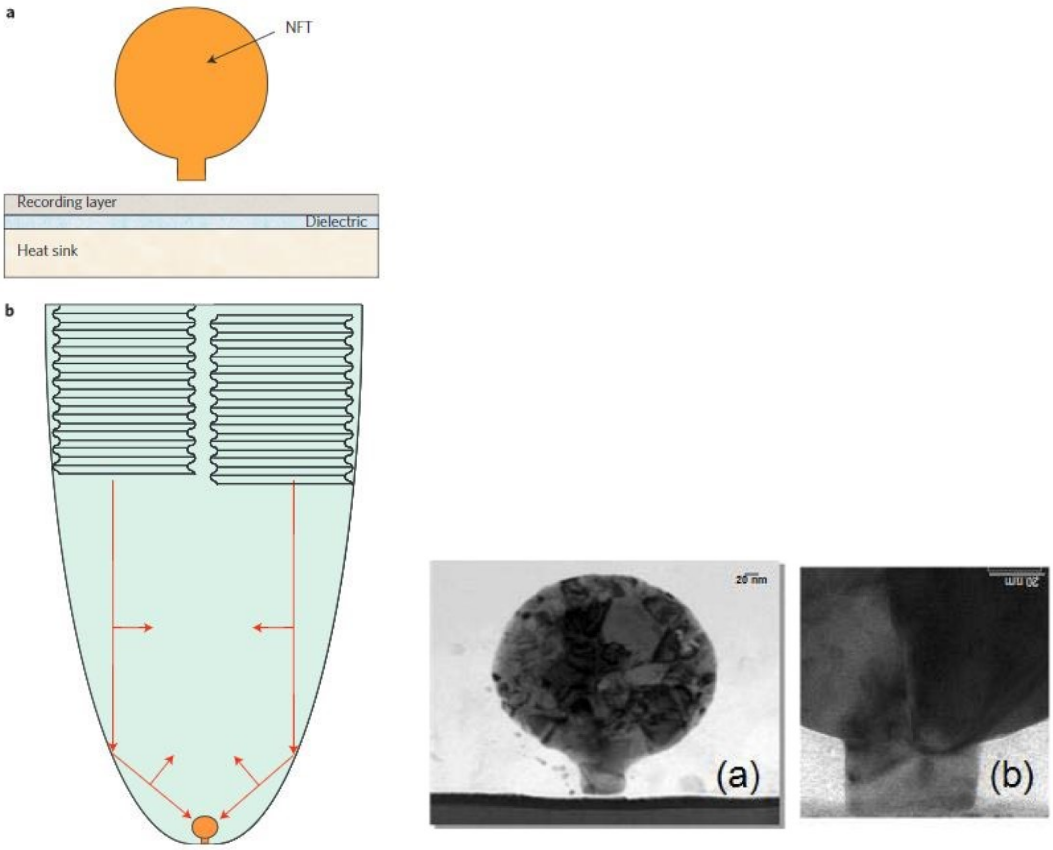

Fig. 2.3 A planar immersion mirror and Au disk NFT. The right one shows the TEM image of the fabricated NFT and zoom-in peg.

2.2 Heat Assisted Magnetic Recording Process

The areal density can be increased by decreasing the average grain size of the recording grains. To main the stability of the recorded information, the magnetic anisotropy should be increased to maintain the product of $K_u V$. For example, L10 phase FePt is a potential candidate for the magnetic recording material which has high anisotropy ($\sim 10^7 erg/cm^3$) and potentially small grain size. To reduce the switching field to improve the write-ability, the locally heating process is provided by the near-field transducer (NFT). The general write process of HAMR is shown in Figure 2.4 [17].

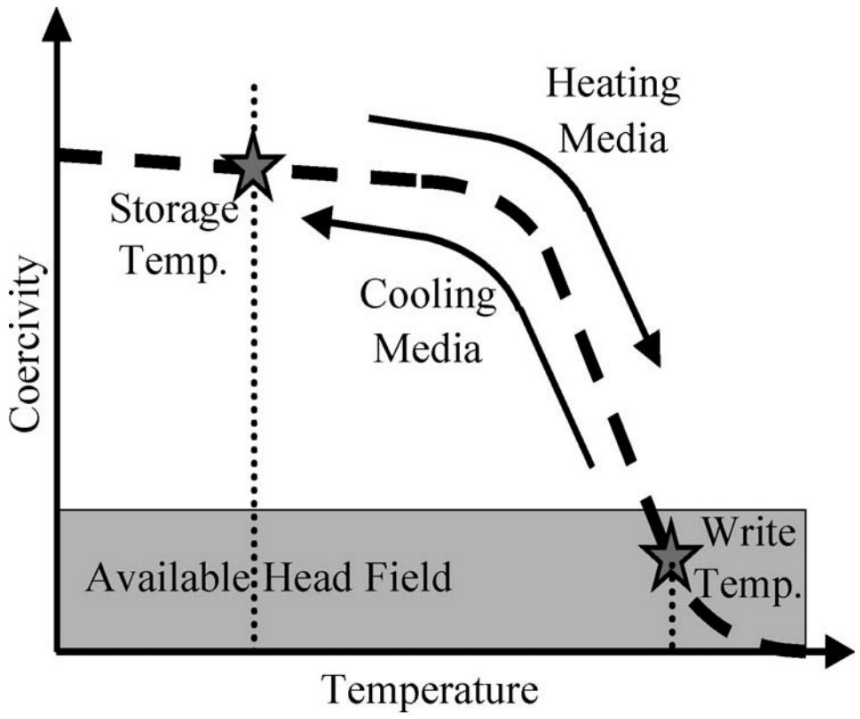

Fig. 2.4 Heat assisted magnetic recording write process.

The recording media is first heated to the write temperature where the switching field (coercivity) is low and available head field is higher than the switching field. The information is recorded into the recording media at the write temperature. Then the temperature is cooled to storage temperature while maintaining the direction of applied magnetic field. Certain direction of the applied magnetic field corresponds to specific information represented by "1"s or "0"s. When the temperature is below the storage temperature, the write process finishes. At room temperature, the information will be stable due to high anisotropy provided by recording materials like FePt. Therefore, the magnetic trilemma is broken by the heating process mentioned above. Figure 2.5 shows a quadrilemma proposed for HAMR in reference [19].

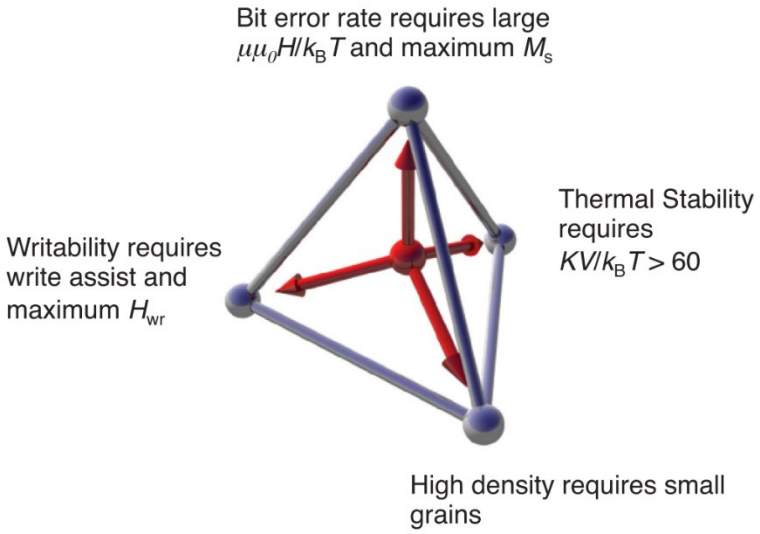

Fig. 2.5 Schematic of the "quadrilemma" of magnetic recording. μ is magnetic permeability and the other definitions are same with those in trilemma.

2.3 Noise Sources for HAMR

Usually, the writing happens at an elevated temperature which is close to the Curie temperature of the recording media. The magnetization M_s and anisotropy K_u have small values at the high temperatures. Thus, we get low Zeeman energy $M_s HV/k_B T$ and bad thermal stability $K_u V/k_B T$. These two terms together result in low energy barrier. Therefore, both the thermal fluctuation and Curie temperature variance σT_c can greatly affect the recording performance.

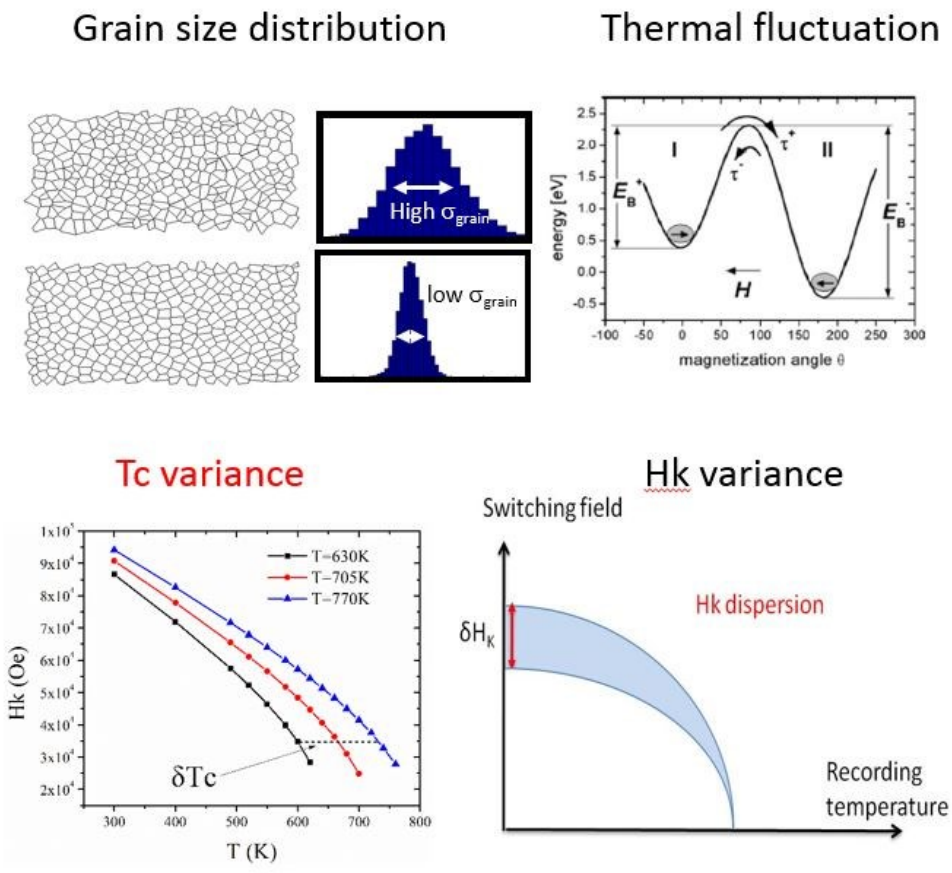

Fig. 2.6 Possible noise sources for heat assisted magnetic recording [20] [21].

Generally, HAMR is still a type of perpendicular magnetic recording technology. Therefore, anisotropy variance σH_k and grain size distribution existing in current HDD media can also contribute to the total noise of HAMR. The difference is that thermal fluctuation and Tc variance are two new noise sources which are pertinent to HAMR media. Figure 2.6 shows the overview of noise sources of HAMR media. The total noise in magnetic recording include transition noise and remanence noise. One useful parameter which can evaluate the transition noise is called transition jitter [22] [23] [24] [25].

Grain size distribution is induced by variance during the fabrication process and surface shape variance of single crystal structure in thin film. At elevated write temperature, the energy barrier under applied magnetic field tends to be low. It is comparable to thermal fluctuations. Therefore, the thermal fluctuation field can cause the magnetic spin direction opposing the correct direction defined by the applied magnetic field. Therefore, this will introduce noise and increase the bit error rate. In other words, the ultimate recording density is limited by the thermal stability of the recording grains during the dynamic writing process. Similar arguments about the thermal fluctuation and quantitative description of bit error rate and areal density can be found in reference [26]. The anisotropy variance here means the intrinsic anisotropy variance. The essence of anisotropy variance is investigated by researchers from HGST (Hitachi Global Storage Technologies). The paper [27] describes the effects from H_k variance using switching field distribution (SFD: one important parameter for media characterization in perpendicular magnetic recording technology). The current understanding of Curie temperature variance is due to the chemical and magnetic ordering. Papers [28] [29] discussed the grain-size dependence of

Curie temperature. The size dependence results are shown in Figure 2.7. The dashed line is a guide to the eye and the solid lines are made by fitting the data. Therefore, the figure tells that the grain size distribution induces the Tc variance σT_c [30].

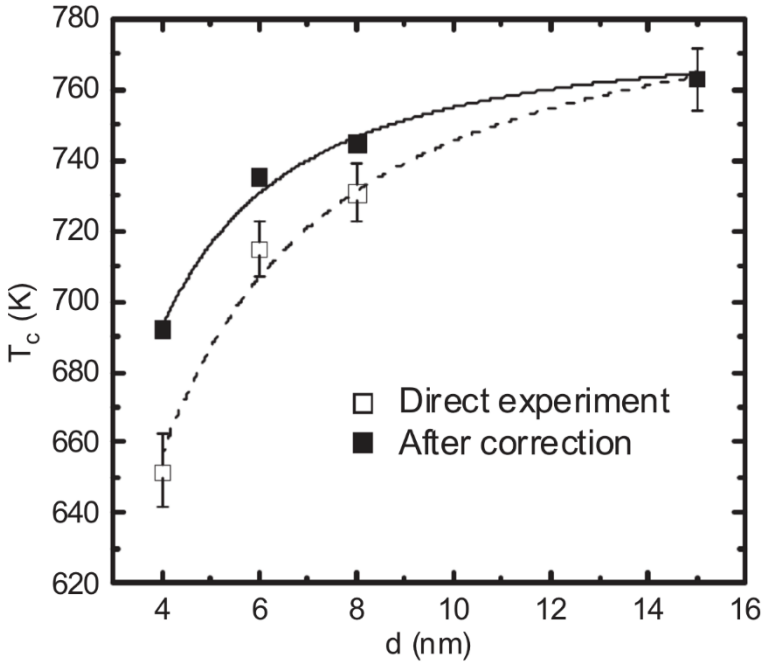

Fig. 2.7 The dependence of Curie temperature on grain size.

In summary, all these four noise sources can broaden the transition width which will degrades the areal density. However, few investigations have been done to quantitatively analysis the effects from these four different noise sources on the media noise (transition noise or remanence noise). In terms of H_k variance σH_k and T_c variance σT_c, H. Li and J. Zhu from CMU published the paper that shows the domination of T_c variance over H_k

variance. However, further comparisons of the effects from these four noise sources and investigations on the relationship among noise sources are still needed.

2.4 Heat Assisted Magnetic Recording Media

Traditional Heat-assisted magnetic recording uses a single recording layer with other functional layers. HAMR usually requires recording material with high anisotropy. The fabrication process requires high processing temperature. However, high temperature favors grain size growth and bad microstructure (grain size distribution). This challenges the media fabrication process. The potential materials for HAMR are listed in Table 2.1.

Table 2.1 List of properties of high anisotropy magnetic material. [31]

Type	material	K_1 (10^7erg/cm^3)	M_S (emu/cm^3)	H_K (kOe)	T_C (K)	D_P (nm)
Co-alloy	CoCr20Pt15	0.3	330	18.2		14.4
	Co3Pt ($L1_2$)	2	1100	36.4		6.9
	(CoCr)3Pt	1	800	25.0		10.2
	CoPt3	0.5	300	33.3	600	9.7
Multilayer	Co2/Pt9	1	360	55.6	500	6.6
	Co2/Pd9	0.6	360	33.3	500	9.1
$L1_0$	FePd	1.8	1100	32.7	760	7.8
	FePt	7	1140	122.8	750	**2.6**
	CoPt	4.9	800	122.5	840	3.0
R.E.	SmCo5	20	910	439.6	1000	1.4

Figure 2.8 shows one example of the multilayer recording media and the TEM image of a recording layer made by L10 FePt. The firstly reported L10 FePt media is shown in references [32] [33]. The improvements of recording media focus on the microstructure, magnetic properties, thermal stack design and media mechanical performance. These aspects are related to possible noise sources such as grain size distribution, anisotropy distribution, Curie temperature variance and thermal fluctuation [34] [35] [36].

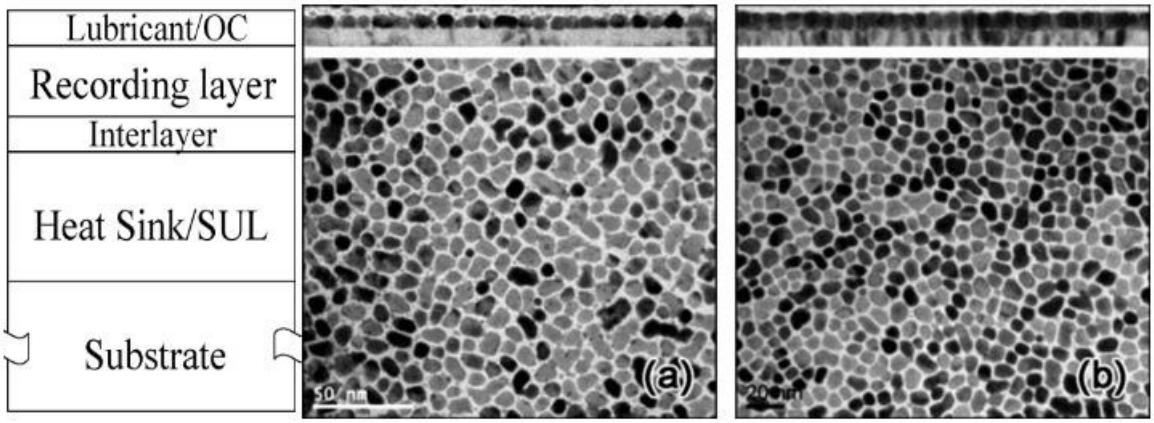

Fig. 2.8 The multilayer structure of traditional HAMR media and the TEM image of the recording layer made by L10 phase FePt.

As we have already known, the Curie temperature variance is caused by chemical ordering and grain size distribution. The grain size distribution and Curie temperature variance are the ones we want to control or evaluate during fabrication process. Therefore, extraction of these information is important. X-ray diffraction and transmission electron microscopy can offer grain size distribution information shown in reference [37]. In terms of the Curie temperature variance, a newly-developed temperature-dependent complex ac susceptibility method is used to extract σT_c information [38].

2.5 Summary

To summarize, the challenges that HAMR systems are facing include developing efficient and robust optical near field transducer (NFT) and designing low noise high-anisotropy magnetic media. The current challenge of the near field transducer will be the reliability, robustness and power delivery. On the other hand, for recording media, challenges lie in aspects of thermal profile, media quality and noise mechanisms. In terms of the media noise, the microstructure, roughness and magnetic properties (distributions) are the essential parameters to consider in order to get high areal density. Ideally, the lollipop Au NFT can provide high thermal gradient to decrease the noise and narrow track pitch to increase the areal density.

Heat Assisted Magnetic Recording has made important process in the past few years. The near field transducer technology and recording media technology are heading to commercialization. Based on my opinion, for future optimization of HAMR media, the noise mechanism needs to be re-investigated due to the completely different recording process occurring in HAMR. New parameters indicating the underlying physics need to be derived. Old metrics like the switching field distribution SFD and effective field gradient should be modified accordingly. New composite media design can be the next research topic about HAMR media.

Chapter 3

Micro-magnetic Simulation

Micro-magnetic theory is a commonly used simulation tool for magnetic materials. Some of the ideas were first applied to the wall structure between two antiparallel domains by Landau and Lifshitz in around 1935 [39]. After Brown published several papers about micromagnetic methods in around 1960. He proposed the first complete formulation of the micro-magnetic method in reference [40]. Micro-magnetic theory can substitute the domain theory used previously. It can describe the evolution of magnetic spins' direction with time. Measurements that can't be achieved experimentally, such as the internal spin direction distribution and energy calculation of nano-scale magnetic structures, can be done by micromagnetic simulation. The dynamic micro-magnetic method is the Landau–Lifshitz–Gilbert equation (LLG) equation. The Landau–Lifshitz term shows the magnetic procession under effective field including applied magnetic field, exchange field, thermal field, anisotropy field and demagnetization field. The Gilbert damping part describes ferromagnetic relaxation. The smallest size of one micro-spin is same with the size of one elementary computation cell. To ensure the accuracy of simulation, the cell size should be

much smaller than the size of domain or domain wall. By using the LLG equation and calculated effective field, the micro-magnetic methods provide one of the best approximations to the magnetic behavior of magnetic spins. Therefore, we can obtain the macroscopic magnetic properties through simulation. With the development of high-speed computers, the micro-magnetic method has the capability to simulate the real-size material so that the simulation results can be comparable to the realistic situations. The renormalized method and parallel computing can further increase the simulation efficiency.

3.1 Landau Lifshitz Gilbert Equation

As mentioned above, the LLG equation includes the magnetic procession part and energy dissipation part. The gyromagnetic ratio and damping constant are two important parameters. Detailed information about these two parts will be given in the following sections.

3.1.1 The gyromagnetic ratio: free procession

Based on quantum theory, the magnetic moment $\vec{M}$ is proportional to its angular momentum $-\gamma\vec{L}$ where γ is the gyromagnetic ratio. The magnetic torque can be calculated by $\vec{T} = \vec{M} \times \vec{H}$. At the same time, Newton's law of motion shows that change rate of angular momentum is equal to a torque $\vec{T}$, which gives $d\vec{L}/dt = \vec{T}$. Simple mathematical derivation by eliminating the torque term gives the free procession of magnetic spin under effective magnetic field (equation 3.1).

$$\frac{d\vec{M}}{dt} = -\gamma \vec{M} \times \vec{H} \tag{3.1}$$

Here, for ferromagnetic materials, the gyromagnetic ratio γ is 17.6 MHz/Oe. The free procession means that the magnetic spin processes around the direction of effective field $\vec{H}$ with angular velocity $\omega = \gamma H$.

3.1.2 The Gilbert Damping Constant: Dissipative Forces

Free procession will be affected by the damping forces under applied field. The magnetic spin has the tendency to align with the direction of the magnetic field $\vec{H}$. The complete LLG expression becomes

$$\frac{d\vec{M}}{dt} = -\frac{\gamma}{1+\alpha^2}\vec{M} \times \vec{H}_{eff} + \alpha\frac{\gamma}{1+\alpha^2}\vec{M} \times \frac{d\vec{M}}{dt} \tag{3.2}$$

By using equation (3.2) and $\vec{M} \cdot \frac{d\vec{M}}{dt} = 0$, we got another expression of the LLG equation, which is more suitable for numerical implementation based on the complete expression of $d\vec{M}/dt$.

$$\frac{d\vec{M}}{dt} = -\frac{\gamma}{1+\alpha^2}\vec{M} \times \vec{H}_{eff} - \alpha\frac{\gamma}{1+\alpha^2}\vec{M} \times (\vec{M} \times \vec{H}_{eff}) \tag{3.3}$$

3.1.3 Numerical Implementation

The equation (3.3) is a system of ordinary differential equations. To solve it numerically, the 4th order Runge Kutta method (well-known RK4) is implemented. The initial conditions include the magnetization, temperature, the direction of each magnetic spin and the applied magnetic field (direction and magnitude). The general expression of RK4 method is shown in equation (3.4) which is based on ordinary differential equation $\dot{y} = f(y,t)$. The initial condition is $y(t_0) = y_0$.

$$y_{n+1} = y_n + \frac{h}{6}(k_1 + 2k_2 + 2k_3 + k_4) \tag{3.4}$$

Here, h is the smallest time step. $t_{n+1} = t_n + h$. k_i can be represented by the following 4 expressions.

$$k_1 = f(t_n, y_n) \tag{3.5}$$

$$k_2 = f(t_n + \frac{h}{2}, y_n + \frac{h}{2}k_1) \tag{3.6}$$

$$k_3 = f(t_n + \frac{h}{2}, y_n + \frac{h}{2}k_2) \tag{3.7}$$

$$k_4 = f(t_n + h, y_n + hk_3) \tag{3.8}$$

Under specific initial conditions and time step, y as a function of t can be obtained. Based on equation (3.3). $\overrightarrow{M}$ can be represented by three vectors in spherical coordinates.

$$M_x = M_s \sin(\theta)\cos(\varphi) \tag{3.9}$$

$$M_y = M_s \sin(\theta)\sin(\varphi) \tag{3.10}$$

$$M_z = M_s \cos(\theta) \tag{3.11}$$

Therefore, the time derivative of $\overrightarrow{M}$ can be written as equation (3.12)

$$\dot{\vec{M}} = (\dot{\theta}\cos(\theta)\cos(\varphi) - \dot{\varphi}\sin(\theta)\sin(\varphi))\vec{x} + (\dot{\theta}\cos(\theta)\sin(\varphi) + \dot{\varphi}\sin(\theta)\cos(\varphi))\vec{y} - (\dot{\theta}\sin(\theta))\vec{z} \tag{3.12}$$

Equation (3.13) and (3.14) can be obtained after tedious mathematic derivations based on equation (3.3) and (3.12). They are two time evolution expressions for the directions of magnetic spins. The magnitude of the magnetization of each spin is assumed to be constant at specific temperature. Therefore, if we can predict the correct direction evolution with time, we will get the dynamic changes of the magnetic spins based on RK4 method.

$$\begin{aligned}\dot{\theta} = {} & \frac{\gamma}{1+\alpha^2}(\alpha\cos(\theta)\cos(\varphi) - \sin(\varphi))H_x \\ & + \frac{\gamma}{1+\alpha^2}(\alpha\cos(\theta)\sin(\varphi) + \cos(\varphi))H_y - \frac{\gamma\alpha}{1+\alpha^2}\sin(\theta)H_z\end{aligned} \tag{3.13}$$

$$\begin{aligned}\dot{\varphi} = {} & -\frac{\gamma}{(1+\alpha^2)\sin(\theta)}(\cos(\theta)\cos(\varphi) + \alpha\sin(\varphi))H_x \\ & + \frac{\gamma}{(1+\alpha^2)\sin(\theta)}(\cos(\varphi) - \cos(\theta)\sin(\varphi))H_y + \frac{\gamma}{1+\alpha^2}H_z\end{aligned} \tag{3.14}$$

3.2 Effective field H_{eff}

Based on equation (3.13) and (3.14), the next step is calculating the effective field H_{eff} before numerically solving the equation. The effective field is a sum of the anisotropy field H_k, exchange field H_{ex}, thermal field H_{th} and demagnetization field H_d. $H_{eff} = H_k + H_{ex} + H_{th} + H_d$. The basic mechanisms in magnetic thin films, such as switching mechanism under applied magnetic field, are about balancing different energies to minimize the total energy until it reaches a local minima. Therefore, the corresponding energy terms are also introduced.

3.2.1 Anisotropy Field H_k

The anisotropy field determines the measurement results based on different measuring directions. There are several origins of anisotropy energy, including the magneto-crystalline anisotropy and stress anisotropy. The magneto-crystalline anisotropy includes uniaxial anisotropy, shape anisotropy, and cubic anisotropy. The stress anisotropy makes contribution when the atomic structure of materials deform. For micro-magnetic simulation of magnetic recording materials, only uniaxial and cubic anisotropy will be considered for anisotropy field. The uniaxial anisotropy can be calculated by equation (3.15).

$$\vec{H}_k = \frac{2K}{M_s}\vec{m}_z \tag{3.15}$$

For L10 FePt media of HAMR, only the uniaxial anisotropy field will be considered based on direction of easy axis. The other kind of anisotropy, such as the cubic anisotropy field can be calculated by the corresponding energy terms shown as equation (3.16).

$$E_{ani} = K_0 V + K_1(\alpha_1^2\alpha_2^2 + \alpha_2^2\alpha_3^2 + \alpha_1^2\alpha_3^2) + high - order - terms \tag{3.16}$$

Where α is the direction cosine functions. The K_i are material and temperature dependent.

3.2.2 Exchange Field and Thermal Field

The exchange field can be calculated by equation (3.17)

$$\vec{H}_{ex} = \frac{2A}{M_s^2}(\nabla^2 M_x \hat{x} + \nabla^2 M_y \hat{y} + \nabla^2 M_z \hat{z}) \tag{3.17}$$

The second-order derivative in the expression of (3.17) can be approximated in terms of the size of computational cell. This is shown as equation (3.18).

$$\vec{H}_{ex}(i,j,k) = \frac{2A}{M_s^2}\begin{bmatrix} \dfrac{M_s(i+1,j,k) + M_s(i-1,j,k)}{(\Delta x)^2}\hat{x} + \\ \dfrac{M_s(i,j+1,k) + M_s(i,j-1,k)}{(\Delta y)^2}\hat{y} + \\ \dfrac{M_s(i,j,k+1) + M_s(i,j,k-1)}{(\Delta z)^2}\hat{z} \end{bmatrix} \tag{3.18}$$

Here, i, j, k stands for the index of the 3D position of each computational cell. A is the exchange stiffness. $\Delta x, \Delta y \; and \; \Delta z$ represent the cell dimension.

The thermal field can be calculated following the concept in reference [41]. Equation (3.19) shows the expression of field values. It follows Gaussian distribution in 3D space.

$$H_{thermal} = \sqrt{\frac{2k_B \times T \times \alpha}{M_s \times \Delta t \times (\Delta x)^3} \frac{1+\alpha^2}{\gamma}} \tag{3.19}$$

Here, α is the damping constant. γ is the gyromagnetic constant. Δt is the time step. k_B is the Boltzmann constant. T is the temperature.

3.2.3 Shape Anisotropy and Demagnetization Field

The calculation of magnetostatic energy and demagnetization field has an important role in micromagnetic simulation. The demagnetization field has long-range nature which means one magnetic spin is affected by all the other magnetic spins. Assuming the total number of magnetic spins is n, the computational cost will be $O(n^2)$. However, for anisotropy field and exchange field, the computational cost is only O(n). Therefore, most of the simulation time will be spent on the demagnetization field calculation. The magnetostatic interaction induces the shape anisotropy. The shape anisotropy causes the demagnetization field H_d which can be written as equation (3.20).

$$\vec{H}_d = N_d \vec{M} \tag{3.20}$$

Here, N_d is a second-order tensor related to shape anisotropy shown by equation (3.21).

$$N_d = \begin{bmatrix} N^{xx} & N^{xy} & N^{xz} \\ N^{yx} & N^{yy} & N^{yz} \\ N^{zx} & N^{zy} & N^{zz} \end{bmatrix} \tag{3.21}$$

Here, $N^{xx} + N^{yy} + N^{zz} = 4\pi$. Therefore, the general expression for demagnetization field is shown as equation (3.22).

$$\vec{H}_d(\vec{r}) = -\sum_r N_d(\vec{r}, \vec{r}')M(\vec{r}') \tag{3.22}$$

If we transform (3.22) into Fourier space, the discrete convolution of N_d and M can be transferred to a direct product of these two parameters in k space. Details of this implementation can be found in reference [42]. The Fourier transform or inverse Fourier transform is practical but still time consuming. The parallel computing in CUDA/C based on Nvidia graphic architecture can greatly improve the FFT calculation efficiency. Even the recording simulation with realistic media dimension becomes possible [43].

The architectures of GPU and CPU are listed in Figure. 3.1. The CPU has powerful cores which can finish complex logic operation with the help from RAM. However, the number of cores is limited by CPU architecture. 4~8 cores are commonly implemented in current CPUs. This causes the critical efficiency limitation when the system is large. However, the GPU has a huge number of computing cores that can finish basic logic operations. This is

enough for the fast Fourier transform in 3D space. The huge number of cores greatly increases the computational speed. For recording simulation, the recording media represented by Voronoi cells is usually discretized into regular shapes, which has been described in renormalized method section. This is perfect for parallel implementation.

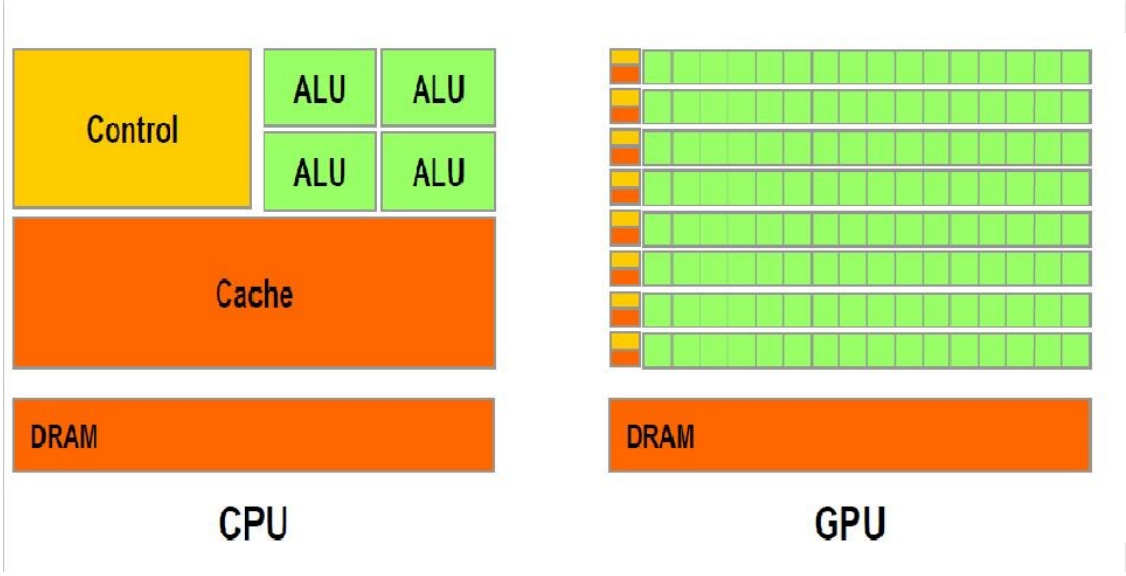

Fig. 3.1 Comparison between CPU and GPU architecture.

3.3 Renormalized Method for HAMR

Renormalization theory [44] indicates that, for a multi-spin system with exchange coupling among spins, larger spin blocks can substitute for several atomistic spins. Therefore, the renormalization method can greatly increase the simulation efficiency. This method is guaranteed by the fact that the correlation length of spin fluctuations becomes large at high temperatures near T_c. A large spin block is called a renormalized cell. The PMR usually works at room temperature at which the magnetic properties have less length-scale

dependence. However, HAMR usually works at high temperature region at which the magnetic properties greatly depend on the length-scale. The atomistic simulation will be impractical due to large number of atomistic spins. To represent the HAMR emdia with renormalized spins, the magnetic properties need to be re-derived under specific renormalized cell size.

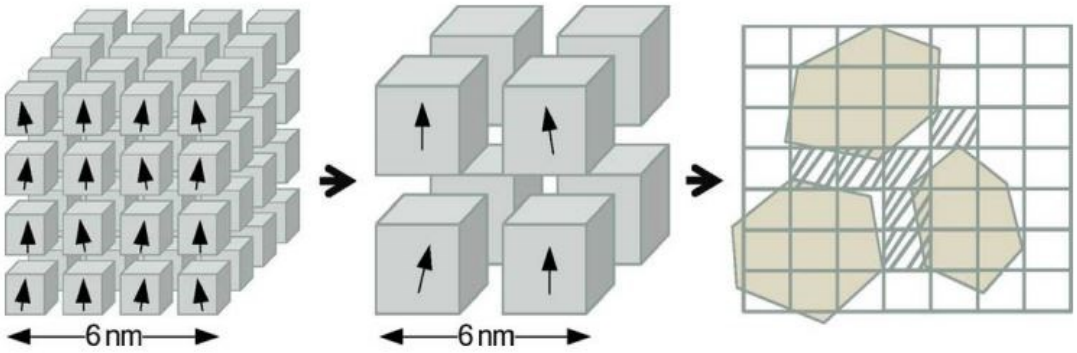

Fig. 3.2 The atomistic spin are coarsened into renormalized spin. The Voronoi grains are used to mimic recording grains. The Voronoi grains including non-magnetic boundary (the shaded region) are divided into cubic cells in 3 dimension.

To get the renormalized parameters, a system which is a 6 nm^3 cube is used to calculate the macroscopic magnetic properties including the average and variance of anisotropy field and magnetization. The "average" here means taking statistical average over space and time. The atomistic spins use the atomistic magnetic properties without the effects from thermal fluctuations. Then the atomistic spins are aggregated into renormalized cubic cells. The magnetic properties of renormalized cells are chosen to produce the same macroscopic magnetic properties or minimize the difference between atomistic system and renormalized system (equation (3.23-3.26)).

$$(\delta H_k)_{atomistic} = \left\lfloor \delta H_k(M_s, K_u, A_{xy}, A_z) \right\rfloor_{renormalized} \tag{3.23}$$

$$\left\langle H_k \right\rangle_{atomistic} = \left\langle H_k(M_s, K_u, A_{xy}, A_z) \right\rangle_{renormalized} \tag{3.24}$$

$$(\delta M)_{atomistic} = \left\lfloor \delta M(M_s, K_u, A_{xy}, A_z) \right\rfloor_{renormalized} \tag{3.25}$$

$$\left\langle M \right\rangle_{atomistic} = \left\langle M(M_s, K_u, A_{xy}, A_z) \right\rangle_{renormalized} \tag{3.26}$$

The damping constant is calculated by (3.27) following the ideas in reference [46].

$$\frac{\alpha_{block}}{1+\alpha_{block}^2} = \frac{-M_{i,atom}\left\langle \sum_i^{agg} \frac{d\vec{M}_{i,atom}}{dt} \cdot \vec{M}_{i,atom} \times \vec{M}_{i,atom} \times \vec{H}_i^{eff} \right\rangle}{\gamma \left\langle \sum_i^{agg} (\vec{M}_{i,atom} \times \vec{M}_{i,atom} \times \vec{H}_i^{eff})^2 \right\rangle_t} \tag{3.27}$$

L10 FePt is chosen as the recording media for HAMR. Here, the input of atomistic scale magnetic parameters for micromagnetic simulation include M_s=1100 emu/cm^3, $K_u = 7 \times 10^7\ erg/cm^3$, $A_{ex} = 1.1 \times 10^{-6}\ erg/cm$ and time step of 4 ns. Renormalization parameters under different temperatures for FePt have been obtained by assuming the exchange interaction is isotropic [43].

However, reference [45] obtained exchange constants in 5 different directions within a single lattice structure, which means the L10 FePt has anisotropic exchange stiffness. Reference [47] shows the renormalized parameters under the situation of anisotropic exchange coupling. Basically, we redo the isotropic process but introducing additional ratio

of A_{xy}/A_z where "xy" means in-plane direction and "z" stands for easy axis direction. The exchange energy can be calculated by the following (3.28).

$$E = \sum_{i,j} \frac{1}{2} J(\Delta S_{ij})^2 V \tag{3.28}$$

Here, J is exchange constant. V is the volume of single crystal lattice. "j" stands for all the nearest neighbors in five different directions. Equation (3.28) can also be represented by $E = 1/V\left[J_{ex,xy}(\Delta S_{xy})^2 + J_{ex,z}(\Delta S_z)^2\right]$ Based on the atomistic value of five different exchange constants in reference [45], the analytical derivation shows that $J_{ex,xy}/J_{ex,z} = 1.32$.

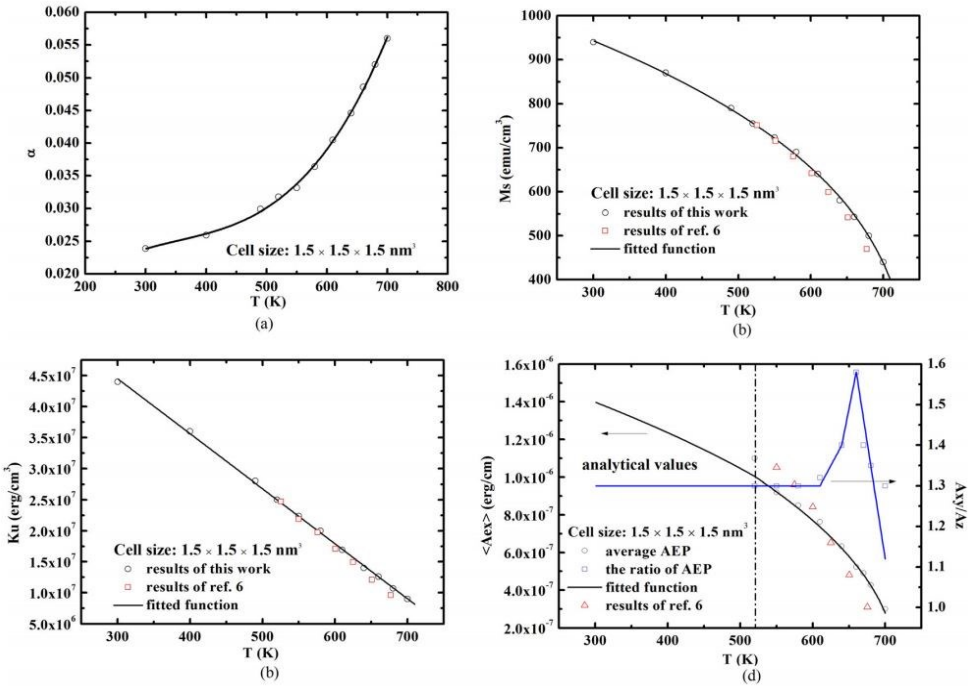

Fig. 3.3 Renormalized parameters as functions of temperature. Circles are the new results based on renormalized anisotropy. Cubic points are from reference [43]. Solid lines shows the fitted functions.

The micromagnetic simulation provided the temperature profile of magnetic properties based on renormalized anisotropy (Figure. 3.3). At high temperature close to T_c, we found that the ratio A_{xy}/A_z has a peak value at around 640–680 K shown as blue curve in Figure 3.3 (d). Reference [47] attributes this to thermal fluctuations. At low temperature, the simulated ratio matches the analytical values calculated from the continuum theory of micromagnetism for $<A_{ex}>$ and A_{xy}/A_z [47].

Now, we have all the magnetic profiles of renormalized cells under different temperatures for both isotropic and anisotropic cases. Therefore, the HAMR dynamic recording process can be fully investigated by using these profiles. On the other hand, the renormalization method and parallel computing will greatly improve the simulation efficiency.

3.4 Summary

The history of LLG equation is introduced. The complete expression include the free procession part and dissipative part. The calculation process of effective field is summarized with corresponding energy terms. The numerical implementation of micromagnetic simulation uses RK4 method to get the evolution of magnetic spins with time. In the end, for HAMR media, the renormalization method is talked about specifically.

Chapter 4

Media Noise and Thermal Switching Probability

The total noise of the HAMR system limits the highest areal density that can be achieved. It includes head noise, media noise and head-disk interface noise. The head-disk interface noise is mainly from mechanical vibration. Media noise is the parameter that should be considered when designing new media structures or optimizing the media. In this chapter, transition noise of the media is firstly introduced. Then, one important distribution named thermal switching probability distribution is described. To measure transition noise, transition jitter is one of the most important parameters for evaluating potential areal density of Heat Assisted Magnetic Recording (HAMR). However, it is time consuming to obtain either experimentally or through micro-magnetic simulation. Here, we show that the more easily calculated thermal switching probability distribution (SPD) can serve as a substitute to evaluate transition noise. In particular, we provide an equation relating the standard deviation of write temperature to jitter. The equation is verified for three critical noise sources: T_c variance, H_k variance and grain size distribution. In addition, the SPD

subject to cooling at various cross-track positions is investigated. A method to determine the magnetic grain size is proposed.

4.1 Transition Noise and Transition Jitter

Besides of the total signal-to-noise ratio (SNR), decoupling of two different kinds of SNR, transition SNR and remanence SNR, is important in either PMR or HAMR media. To calculate transition SNR, the transition noise needs to be calculated. Figure 4.1 shows the remanence region and transition region. [48]

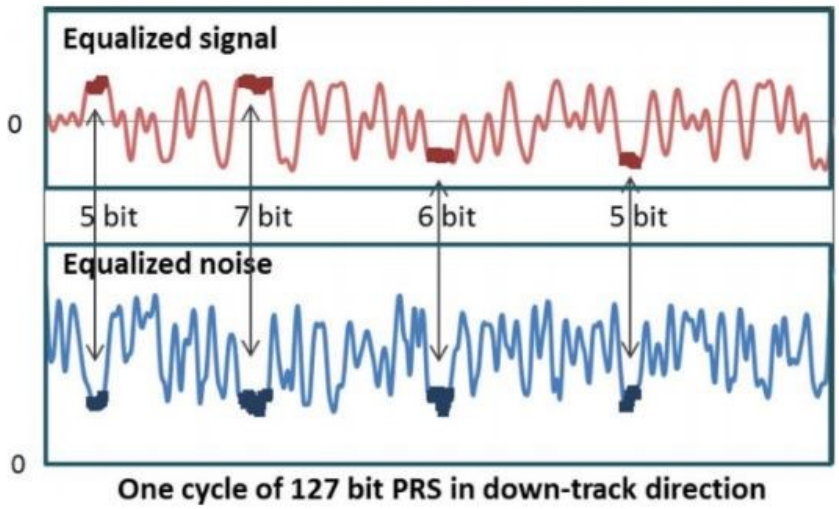

Fig. 4.1 The equalized signal and corresponding equalized noise.

Here, the transition noise means media transition noise. However, in order to extract it, we must get the play-back signal which means there are reader averaging effects. [49] Once we got the play back signal, there are several different methods to define the transition

region and remanence region. For example, in terms of pseudo random bit sequence PRBS, the long bit region is the remanence region. The total noise can be found by subtracting different play-back signals from the noise-free one. [50]. Then, the remanence noise can be found easily. The transition noise can be obtained by subtracting remanence noise from total noise.

To evaluate transition noise, there is one important parameter called transition jitter. It is the standard deviation of zero-crossing locations along down-track direction with unit "nm". One example is shown in Figure 4.2. The transition jitter is calculated based on hundreds of transitions in the region enclosed by red rectangle.

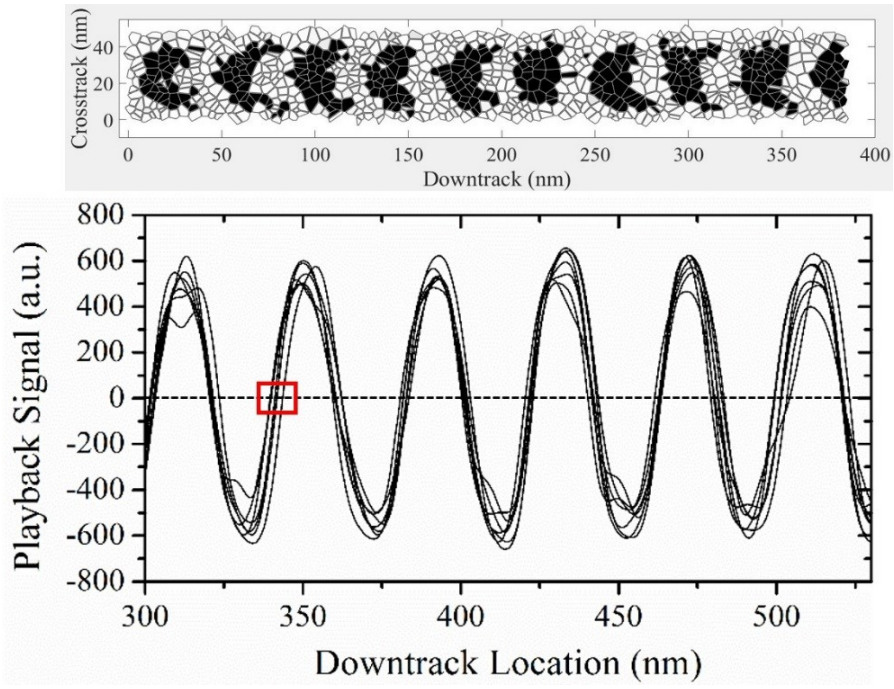

Fig. 4.2 One recording pattern on HAMR media and the corresponding play-back signal

As we have discussed in the previous section, many researchers contribute to the development of transition jitter equation. Reference [23] introduce the field gradient and field distribution effects. Reference [24] considered the effects from realistic grain size distribution. Reference [25] take reader average effects into account. The final complete expression for transition jitter is shown as equation (4.1).

$$\sigma_{jitter} = \sqrt{\frac{\frac{\delta H_c}{dH_c/dx} + \frac{(\langle D \rangle + Bnd)^2}{12}\beta}{\frac{RW}{\langle D \rangle + Bnd}}} \tag{4.1}$$

Here, <D> is the average grain diameter. Bnd is the non-magnetic grain boundary width. β is a function of grain size distribution. [24]. RW stands for reader width. H_c is the coercivity field. The down track direction is same with x direction. Either for HAMR or PMR, thermal fluctuation affects the coercivity. [51] Therefore, the expression in terms of coercivity gradient and distribution includes the thermal fluctuation effects shown as equation (4.2).

$$H_c(t) = H_0\left\{1 - \left[(k_B T / KV)\ln(At)\right]^n\right\} \tag{4.2}$$

Here, $H_0 = H_k$. Anisotropy field H_k is also a function of temperature below the Curie temperature. Therefore, the Curie temperature variance σT_c can cause H_c variance which

will also contribute to the transition jitter. Therefore, two important noises (thermal fluctuation and Curie temperature variance) are both considered in equation (4.1).

4.2 Thermal Switching Probability Distribution of FePt

L10 phase FePt is one of the promising media candidate for Heat Assisted Magnetic Recording (HAMR). The media noise during magnetic recording include transition noise and remanence noise. As we have already talked about, the noise of FePt media mainly derives from H_k variance σH_k, T_c variance σT_c, grain size distribution (GSD), and thermal fluctuations. [52][53] Several research groups have published results about different noise sources of FePt media. [54][55] For example, the dominating effect of T_c variance and erasure-after-write effects from H_k variance have been examined. [55] The thermal switching probability distribution (SPD) has also been examined previously. [56][57] The concept is proposed by R. H. Victora and Michael Mallary. These two references use similar process to get the relationship between switching probability and reverse temperature. The recording media is first heated to peak temperature. Then, a linear cooling rate is applied to the media. At the same time, the applied magnetic field remains in the upward direction. When the temperature reaches reverse temperature T_{rev}, we change the direction of the applied field to be downward. Then we continue to decrease the temperature to room temperature. At room temperature, the switching status of each grain can be known so that we can calculate the switching probability P (or P_{sw}). The curve obtained can be treated as error function shown as red curve in Figure 4.3.

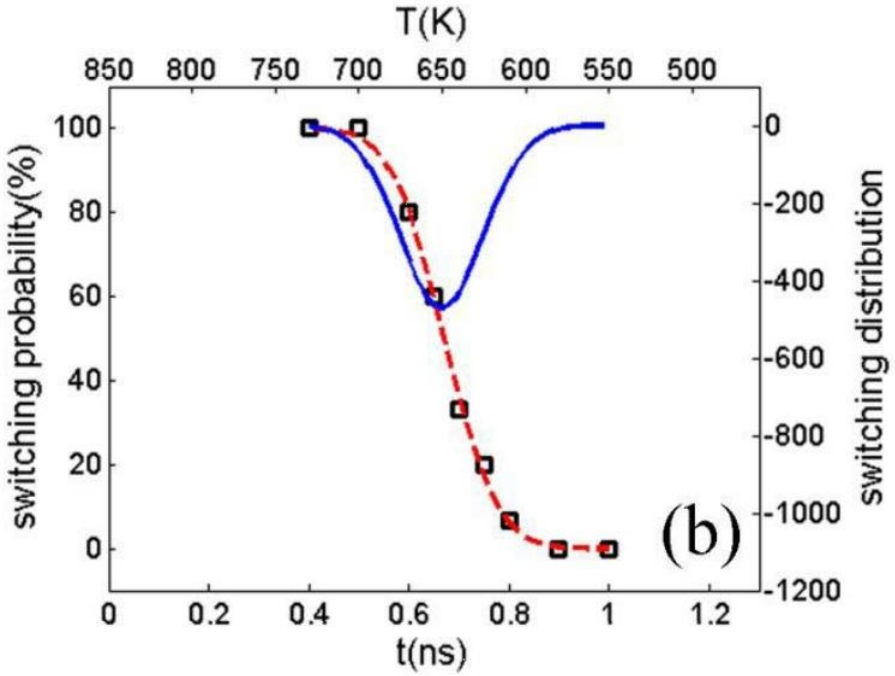

Fig. 4.3 red curve shows an error function that can describe the relationship between switching probability and temperature. Blue curve is the first derivative of switching probability

The blue curve is the temperature derivative of the red curve which is a Gaussian distribution. This distribution is defined as the switching probability distribution (SPD). Two important parameters can be extracted from the blue curve in Figure 4.3. One is the average write temperature defined as the one at which switching probability is 50%. The other one is the transition width which equals full-width-at-half-maximum FWHM of the Gaussian distribution. There is also another simple way to define the transition width which is the temperature difference between switching probability with 10% and 90%.

The micromagnetic simulation uses the LLG (Landau-Lifshitz-Gilbert) equation. The renormalized method developed for FePt is implemented with $1.5nm \times 1.5nm \times 1.5nm$ renormalized cells. [43] In terms of magnetic properties used for FePt, at temperature of

300K, $M_s = 920 emu/cm^3$, $K_u = 4.2 \times 10^7 erg/cm^3$ and $A_{ex} = 1.1 \times 10^{-6} erg/cm$. The Curie temperature T_c of FePt is 700 K. The full-width half-maximum FWHM of SPD is usually used to estimate the transition noise. Regarding details the calculation process, the peak temperature $T_{peak} = 850K$. The linear cooling rate is 100K/ns. The number of recording grains on the media is around 400 grains. The grains have no magnetostatic interactions (no grain-to-grain interaction). The applied magnetic field is 8000 Oe and canting angle is 22.5°. The resulting switching probability is shown as the black curve in Figure. 4.4-4.6.

4.3 Effects from σT_c, σH_k and GSD on SPD

As we have talked in section 4.1, at room temperature, the switching status of each grain is collected to get the switching probability P_{sw} as a function of T_{rev}. Ideally, $P_{sw}(T_{rev})$ can be treated as an error function. The SPD is the T_{rev} derivative of P_{sw} and often follows a Gaussian distribution. [57] The micromagnetic simulation model allows us to investigate the effects of different noise sources on SPD independently. Results indicate that the calculated SPD curves affected by different variances doesn't always fit the Gaussian distribution well. Further analysis was done and an evaluation method based on the SPD is proposed.

Uniform grains (GSD=0%) with average diameter $\langle D \rangle = 6.0nm$ (4×4 renormalized 1.5 nm cells in x-y plane) were used to investigate the effects from σH_k. The thickness of the FePt layer is 9 nm. Here, x is along down-track direction and y is along cross-track

direction. $\sigma T_c = 0\%$. We add different H_k variance into the uniform media. Therefore, the results in Figure 4.4 show the effects on SPD and $P_{sw}(T_{reve})$ only from H_k variance. Comparing to an error function, the variance mainly affects the P_{sw} at the low temperature region. This makes $P_{sw}(T_{rev})$ deviate from the error function. Therefore, SPD can't be fitted by the Gaussian distribution well. To maintain the nature of Gaussian distribution and reveals the skewness of the results, we use an exponentially modified Gaussian distribution (EMG) from probability theory. The EMG can capture the correct trend to fit the dP_{sw}/dT (SPDs). Its probability density function PDF follows equation (4.3).

$$PDF = \frac{\gamma}{2} \times \exp\left(\frac{(\gamma \times \sigma)^2}{2} - \gamma \times (x - \mu)\right) \times erfc\left(\frac{\gamma \times \sigma^2 + \mu - x}{\sqrt{2} \times \sigma}\right) \tag{4.3}$$

Here, γ, μ and σ are parameters of the PDF. "erfc" stands for complementary error function. "x" equals temperature.

The number of simulation data points at various reversal temperatures is limited. Equation (4.3) can offer estimates of σ_{SPD}, average writing temperature and asymmetry. Same as the definitions for ideal case, the average writing temperature T_w is defined as the temperature at which dP_{sw}/dT reaches its peak value. It can be calculated by $\mu + 1/\gamma$. The standard deviation of write temperature σ_{SPD} is calculated by $\sqrt{\sigma^2 + 1/\gamma^2}$. The asymmetry of the SPD is evaluated by $T_w - T_{median}$. T_{median} is the temperature at which the switching probability is 50%.

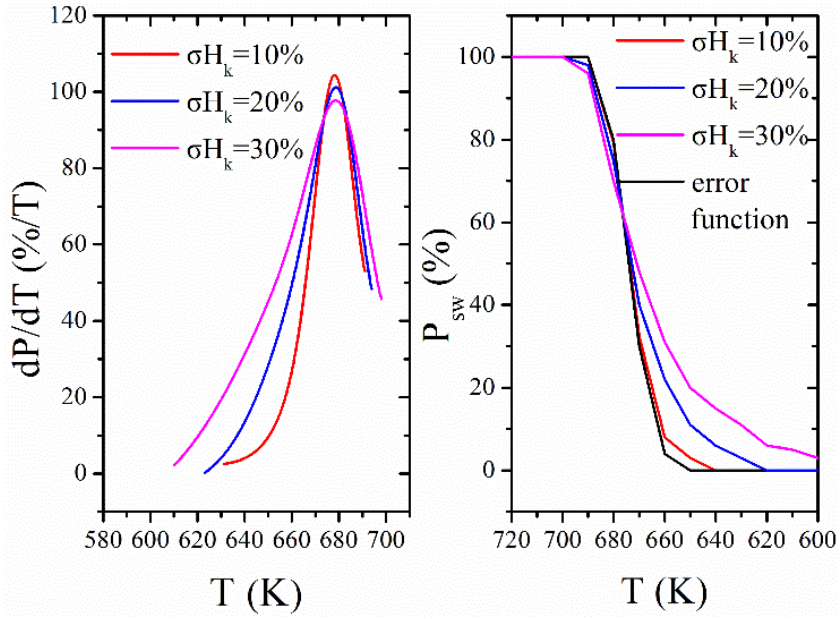

Fig. 4.4 SPD and $P_{sw}(T_{rev})$ for FePt with various H_k variance. Here, $T = T_{rev}$. Different colors corresponds to different σH_k. The e1rror function (black curve) is for the $P_{sw}(T_{rev})$ of FePt under ideal conditions (GSD=0%, $\sigma H_k = 0\%$ and $\sigma T_c = 0\%$).

The SPD results based on different H_k variance are shown as the colored curves on the left part in Fig. 1. $P_{sw}(T_{rev})$ is the corresponding cumulative distribution function. The H_k variance rows in Table I shows that H_k variance does not affect the average writing temperature. The positive asymmetry values and broadening SPD at lower temperatures provide further evidence that the H_k variance's effects on the SPD mainly falls in the low temperature region. This may generate noise in both cross track and down track directions. Larger σH_k results in larger asymmetry and σ_{SPD}, which indicates larger noise during the recording process.

Under different T_c variance of FePt media, the SPDs were calculated (Fig. 4.5) using the same uniform grains (GSD=0%) as in Fig. 1, but with $\sigma H_k = 0\%$. Both the high and low temperature regions are affected by σT_c. Based on the standard deviation σ_{SPD} of the SPD in Table I, the effects of σT_c on σ_{SPD} is larger than those of σH_k. With 3% T_c variance, the σ_{SPD} is increased by almost 3 times. According to the "mean" in Table 4.1, the average writing temperature is higher with larger σT_c. The asymmetry is small and can even be neglected comparing to σ_{SPD}. Therefore, the SPD modified by the T_c variance can still fit the Gaussian distribution well. Furthermore, larger σT_c will reduce the asymmetry of the SPD.

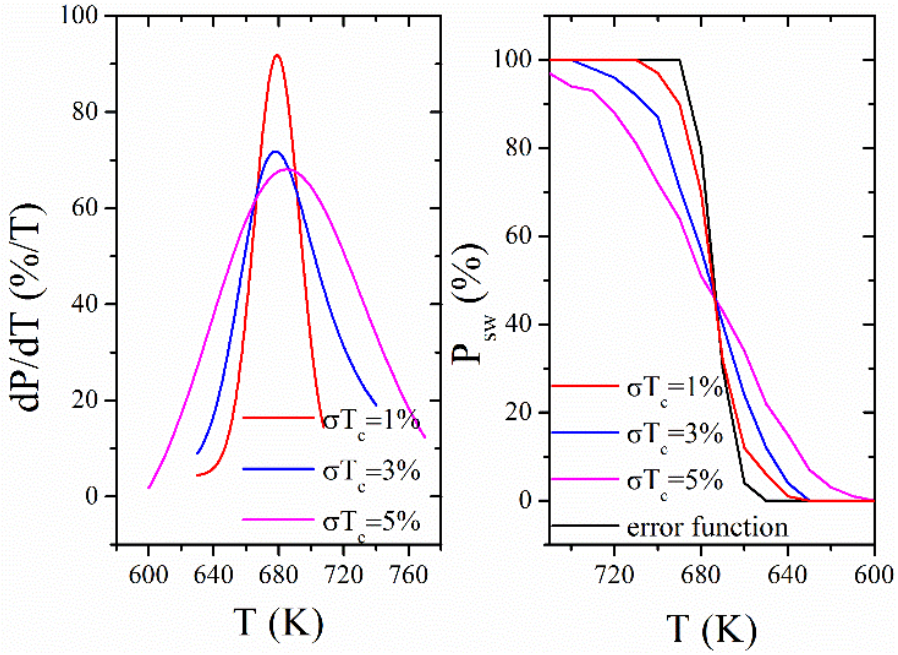

Fig. 4.5 SPD and $P_{sw}(T_{rev})$ for FePt with various T_c variance. Different colors corresponds to different σT_c. Here, $T = T_{rev}$.

Table 4.1 evaluation parameters for different noise sources

σ (%)	mean (K)	σ_{SPD} (K)	asymmetry (K)
σH_k (10%)	677	10.3	3.0
σH_k (20%)	677	16.1	7.0
σH_k (30%)	678	24.0	9.0
σT_c (1%)	670	13.9	2.6
σT_c (3%)	676	35.7	2.0
σT_c (5%)	682	56.2	1.0
GSD (10%)	668	9.7	4.0
GSD (20%)	671	15.0	5.0
GSD (30%)	673	16.0	6.0

We use Voronoi cells to represent the actual recording grains of FePt media instead of the uniform grains used in the previous two cases. This allows us to implement different grain size distributions to the FePt media. We use the same mapping rule [43] to construct the 3 dimensional (3D) configuration of the media using Voronoi patterns. The σH_{K} and σT_{c} are set to zero. The average diameter of Voronoi grains is fixed at 6 nm, which remains consistent with those used for the H_{K} variance and T_{c} variance cases, but with different grain size distribution (GSD). The SPD are calculated for GSD=10%, 20% and 30% (Fig. 4.6). The GSD only affects the low temperature region with less effect than H_{K} variance. Based on the GSD part in Table 4.1, with bigger GSD, the writing temperature tends to be higher and σ_{SPD} is larger. If the variance is smaller than 20%, very similar effects on σ_{SPD} are seen from GSD and H_{K} variance. However, when variance is bigger than 20%, σ_{SPD} caused by H_{K} variance is larger than that of GSD.

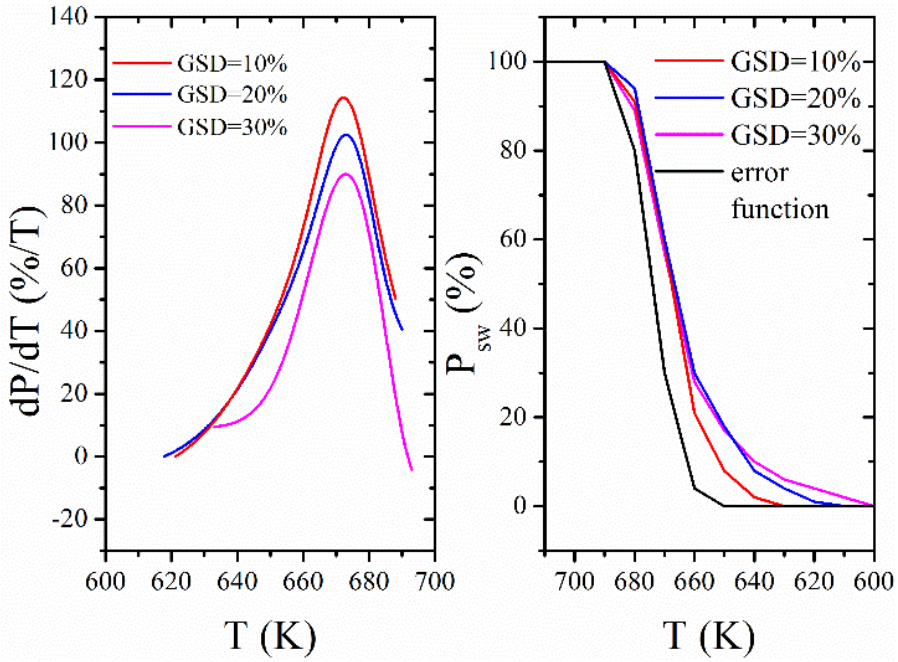

Fig. 4.6 SPD and $P_{sw}(T_{\mathrm{rev}})$ for FePt with various GSD. Different colors corresponds to different GSD. Here, $T = T_{rev}$.

4.4 Relationship between transition noise and σ_{SPD}

The transition noise is one of the important noise sources to be considered in HAMR magnetic recording. σ_{SPD} is considered to be a parameter to estimate the transition noise. [56][57][58] The Tc variance is believed to play a more important role than H_k variance. The GSD is also a noise source. To relate the transition noise to the SPD curves, we set up a magnetic recording simulation model as described in reference. [43] The media dimension is 48 nm along the cross track and 384 nm along the down track. The FePt media thickness is 9 nm. We use Voronoi cells to represent the magnetic recording grains. For

different H_k variance and T_c variance, the grain size distribution is fixed to be 20%. The average grain pitch of grains is 6 nm with 1 nm non-magnetic grain boundaries.

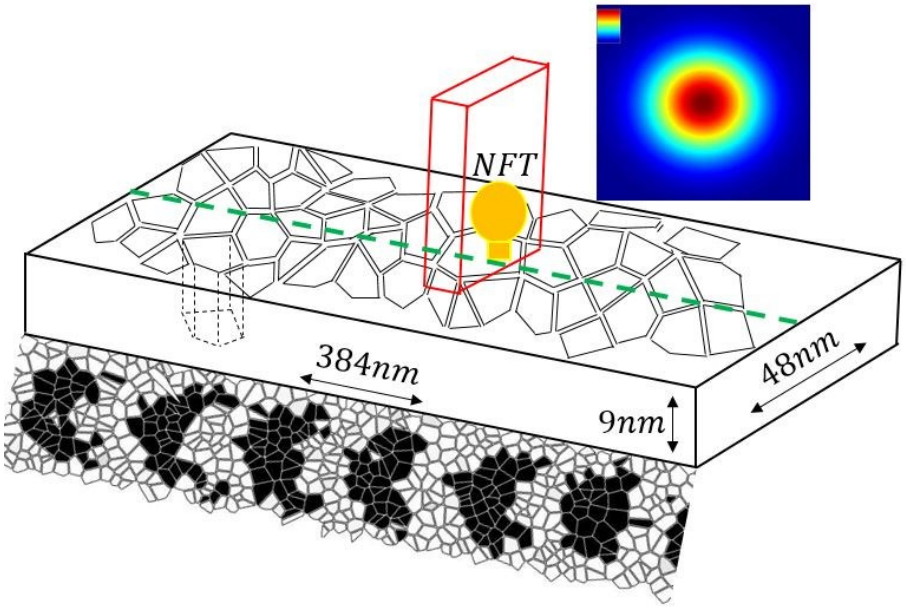

Fig. 4.7 The schematic view of the magnetic recording simulation model. The figure on top right is the temperature profile generated by NFT. The bottom shows the recording patterns gotten by recording simulation.

The magnetic head integrated with near field transducer (NFT) moves with a speed of 20 m/s. The applied magnetic field is 8000 Oe with uniform distribution on the media. The canting angle is 22.5°. The heat profile generated by the NFT can be treated as a 2D Gaussian distribution in the media plane. It is shown as equation (4.4).

$$T(\mathrm{x}) = 300 + \Delta\mathrm{T} \times \exp(-(x^2 + y^2)/(2 \times \delta^2)) \quad (4.4)$$

Here, $\Delta T = 550K$ and $\delta = 17\ nm$. The top-right figure in Fig. 4.7 shows the top view of the in-plane temperature distribution on the recording media. The green line is the track center which is also the center line of the temperature profile.

By using a magnetoresistive reader with 20 nm reader width and 21 nm shield-to-shield distance, the play back signal is obtained for over 200 transitions. The standard deviation of zero crossing locations along down track direction is defined as the transition jitter (noise). We vary media Tc, H_k and GSD separately and calculate the transition jitter. Figure 4.8 shows the comparison between the calculated transition jitter and σ_{SPD} in Table 4.1.

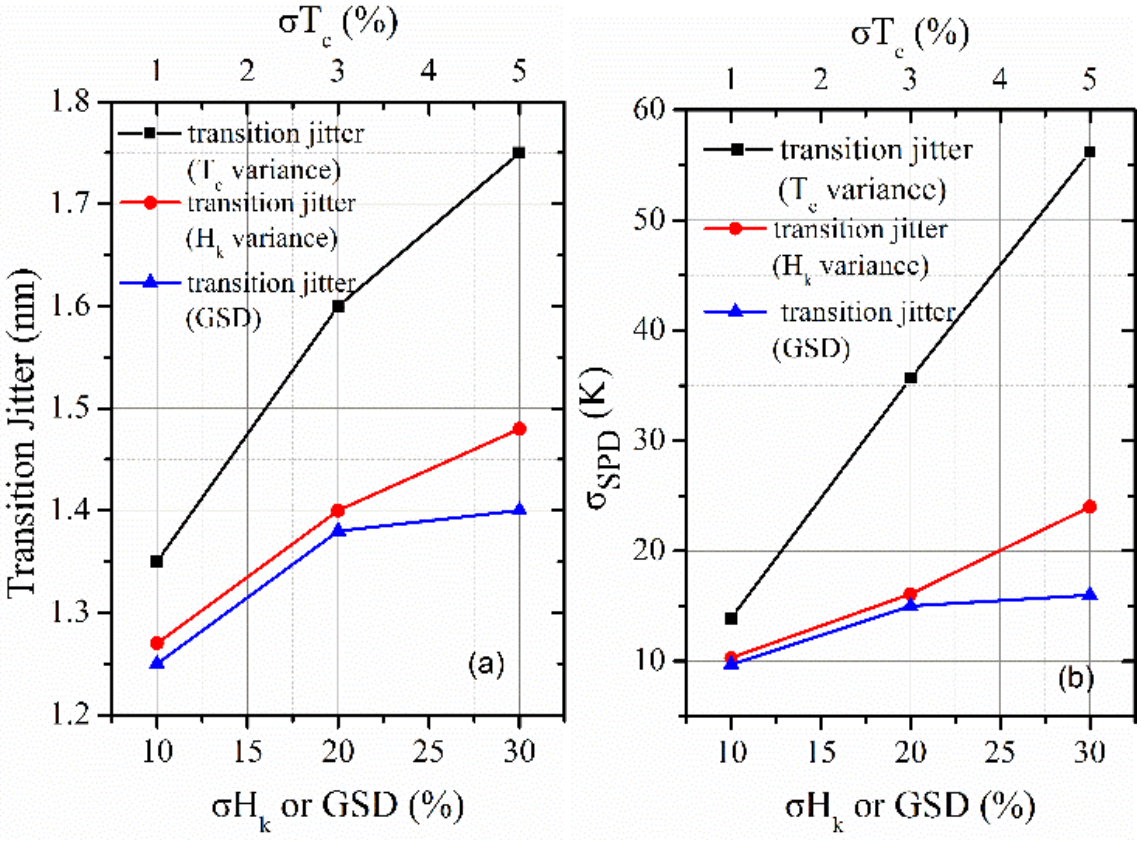

Fig. 4.8 The comparison of effects from Tc variance, Hk variance and GSD on transition jitter and σ_{SPD}.

The transition jitter (left figure in Fig. 4.8) shows that larger H_k variance, GSD and Tc variance causes larger transition jitter (noise). However, the effects from Tc variance is more severe than those of H_k variance and GSD. The transition jitter is increased by 30% for 3% Tc variance but only 12% for 20% H_k variance. This is consistent with the conclusion made in the reference. [54] By fitting 9 pairs of $(\sigma_{SPD}, \sigma_{jitter})$, a relationship between transition jitter σ_{jitter} and σ_{SPD} is found to follow equation (4.5).

$$\sigma_{jitter} \approx 1.83 \times {\sigma_{SPD}}^{0.11} - 1.07 \tag{4.5}$$

Here, 1.07 is around the grain size limit. [58] Therefore, σ_{SPD} can be used to calculate transition jitter of the magnetic recording process. This characterization method is easier to be implemented than magnetic recording tests. Furthermore, for HAMR media, the SPD can take the role of switching field distribution (SFD) which is widely used in characterization of perpendicular magnetic recording (PMR) media.

4.5 SPD in cross-track and down-track direction

For the simulations of Fig. 4.4-4.6 and Table 4.1, the applied magnetic field changed its direction from $+\hat{z}$ to $-\hat{z}$ at a specific temperature T_{rev}. The peak temperature can always reach 850K. This cooling process mainly mimics the transition regions (along the green line in Fig.4.7) between two adjacent bits with different magnetic polarity. Fig. 4.8 verifies that σ_{SPD} is proportional to transition noise. However, for the recording grains inside each recording pattern, the applied field won't change its direction until the cooling process

finishes. Furthermore, the peak temperature that can be reached for grains is different along the cross track direction. It will decrease with increasing distance from the track center based on top-right insert in Fig. 4.7.

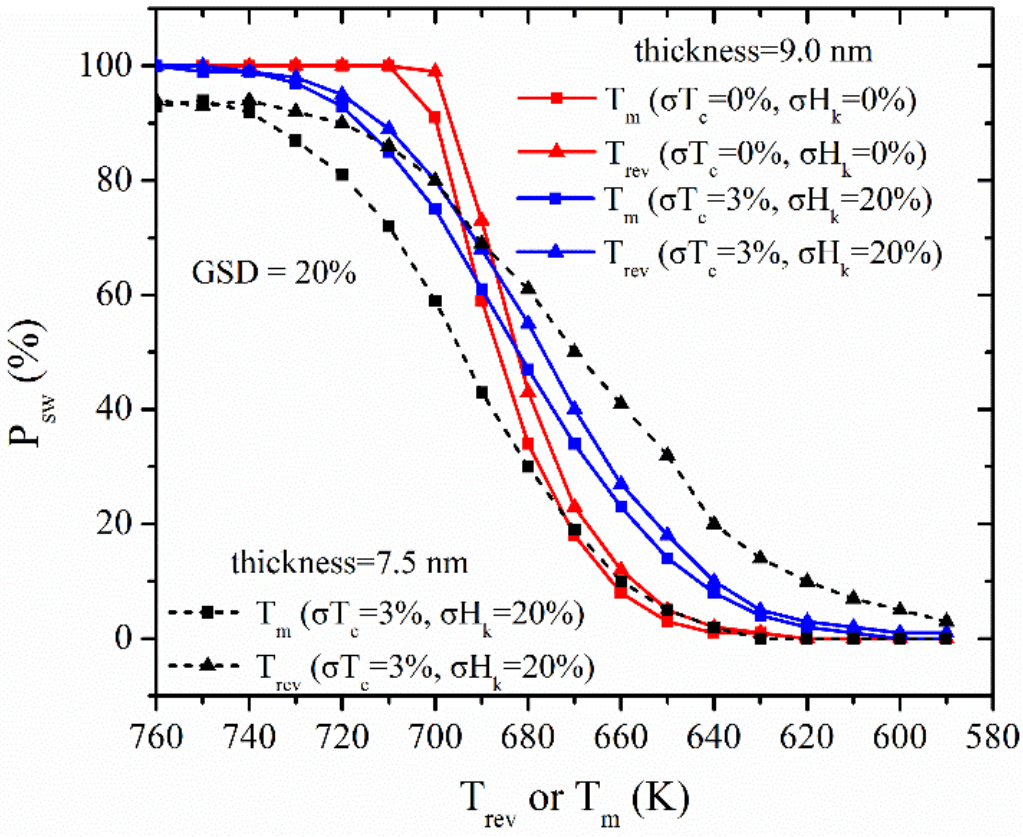

Fig. 4.9 The relationship between switching probability and temperature for T_{rev} and T_m. The cooling rate for black curves is 250 K/ns.

Therefore, we design another cooling process to investigate the switching probability of these grains with lower peak temperature and unchanged magnetic field direction. The temperature of FePt media is linearly increased from room temperature to T_{m} before decreasing. The temperature T_m is the peak temperature that a recording grain can reach during the recording process. The direction of applied magnetic field always aligns with

$-\hat{z}$ direction during the whole process. When the temperature reaches room temperature, thermal switching probability is calculated. Then we get $P_{sw}(T_m)$ instead of $P_{sw}(T_{rev})$.

To make comparison between these two different cooling processes, let $T_{\mathrm{m}} = T_{\mathrm{rev}}$ and the linear cooling rate remains 100 K/ns. The actual recording media always has grain size distribution. Therefore, we assume GSD=20%. The average grain pitch is 6.0 nm. The thermal switching probability is calculated under different T_{rev} and T_{m}. Two different cases are considered: one has no Tc variance and H_k variance and the other one has 3% Tc variance and 20% H_k variance.

The red curve only includes the effects from thermal fluctuation and GSD. Due to the effects from Tc variance and H_k variance, the FWHM of blue curves turns out to be 2 times wider than that of red curves (red curves ~ 32 K and blue curves: ~ 66 K). For both blue curve and red curve, the thermal switching probability at T_{rev} is larger than that at T_m. Analysis of the cooling processes indicate that, comparing to T_m case, the recording grains experience an additional process from 850 K to T_{rev} before the applied magnetic field changes its direction. Even though the magnetic field hasn't changed its direction, at high temperature, the thermal fluctuation can switch the magnetic grains to oppose the direction of applied magnetic field. Therefore, the thermal fluctuation of the additional temperature region increases the thermal switching probability of T_{rev} curves. To further verify this argument, we calculate the thermal switching probability for FePt with 7.5 nm thickness, 3% Tc variance and 20% H_k variance. The average volume of recording grains is smaller than that of blue (red) curve. Both the thermal stability and Zeeman energy are lower based on $K_u V/k_B T$ and $HM_s V/k_B T$. H is the applied magnetic field. The maximum switching

probability of black curves can't reach 100% due to thermal fluctuation. The difference of these two curves become larger unsurprisingly. We believe the difference of these two curves becomes smaller with increasing volume of recording grains. Therefore, T_m may be an easier metrology method to characterize the HAMR media without changing the direction of the applied magnetic field. Furthermore, these two kinds of curves describe the switching probability at transition region and remanence region. The relationship between these two curves with DC and AC noise requires further investigation. A decoupling method similar to the one in the reference needs to be developed for HAMR. [48]

To summarize, σ_{SPD} is verified to be a parameter that can yield the transition jitter (noise) of HAMR media. The effects on the switching probability distribution from T_c variance, H_K variance and grain size distribution are compared under the assumption that they are not correlated with each other. T_c variance is demonstrated to dominate σ_{SPD}. The asymmetry of SPD is mainly caused by H_K variance and GSD. In terms of σ_{SPD}, the order of effects, from large to small, are σT_c, σH_K and GSD. In terms of asymmetry, the order of effects are σH_K, GSD and σT_c. Both σ_{SPD} and asymmetry of the SPD should be considered to evaluate the noise of HAMR media. The exponentially modified Gaussian distribution is demonstrated to represent the switching probability distribution faithfully.

4.6 Grain volume dependence of SPD

L10 FePt is one promising recording media candidate for HAMR as discussed above. The effects from all the possible noise sources are investigated in section 4.4 and 4.5. The simulations were done for FePt grains with specific average grain volume. However, the average grain size and grain volume are both parameters that need to be considered during media design and fabrication. Here, we want to know the volume dependence of switching probability distribution of FePt grain. To gain more freedom of the volume choice, we abandon the renormalized cell with $1.5nm \times 1.5nm \times 1.5nm$ size and choose renormalized cell size $1.0nm \times 1.0nm \times 1.0nm$. Fig. 4.10 (a) and (b) show the temperature profile for the $M_s(T)$ and K(T) at the atomistic scale and at two different renormalized scales ($1nm \times 1nm \times 1nm$ represents new results and $1.5nm \times 1.5nm \times 1.5nm$ is from reference [47]). The new set of parameters is calculated by minimizing the difference of magnetic properties between FePt calculated atomistically and calculated using renormalized cells [43]. Anisotropic exchange was also used (reference [47]). The black curve in Fig. 4.10 (a) represents the function $M_s(T) = M_0 \cdot (T_c - T)^{0.33}$ fitted to the atomistic results. The black curve in Fig. 4.10 (b) shows the temperature profile $K(T) = K_0 \cdot (T_c - T)$. Here, $M_0 \approx 136\ emu/cm^3$, $K_0 \approx 1 \times 10^5\ erg/cm^3$ and $T_c = 710K$. Reference [57] suggests that a simple analytical model can accurately describe the dependence of the thermal switching probability distribution (SPD) on key parameters such as grain volume, applied field strength, damping constant and the cooling rate. It suggests that switching under recording conditions can be approximated as one single spin. Both an analytical model and simulation are proposed and compared.

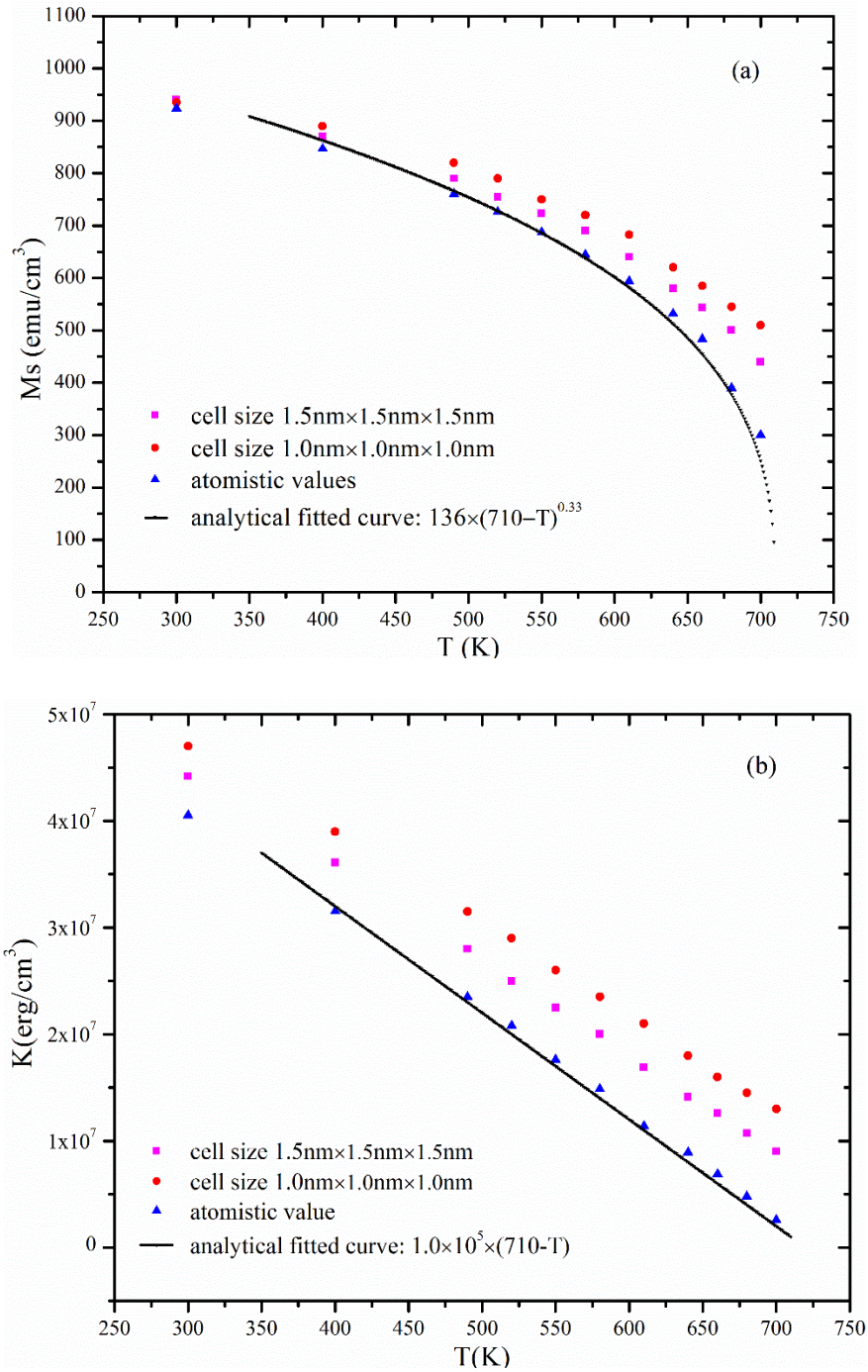

Fig. 4.10 Renormalized magnetic parameters (magenta cubes and red dots) and corresponding atomistic values (blue triangles). Black curves represent functions fitted to the atomistic value.

For a storage layer with volume V, the total magnetic energy can be calculated by $E_{tot} / V = Ksin^2(\theta) - H \cdot M \cdot \cos(\alpha - \theta)$. α is the angle between H and $\hat{z}$ direction. θ is the angle between M and $\hat{z}$ direction. Two assumptions were made to simplify the analytical derivation process: $K \gg M_s \cdot (\vec{H} \cdot \hat{z})$ and $\theta = 0°$. The energy barriers that the system needs to overcome were calculated: $\Delta E_{sw} / V = K(T) - M_s(T) \cdot H$ and $\Delta E_{unsw} / V = K(T) + M_s(T) \cdot H$(more details in [59]). ΔE_{sw} is the energy barrier if the magnetization needs to be switched to align with the applied field. ΔE_{unsw} is the energy barrier if the magnetization is already aligned with the applied field. The probability of each switch becomes: $P_{sw} = e^{-\Delta E_{sw}/k_B T}$ and $P_{unsw} = e^{-\Delta E_{unsw}/k_B T}$. The probability P of field alignment evolves with time as equation (4.6):

$$\mathrm{dP/dt} = \mathrm{A} \cdot \mathrm{P_{sw}} \cdot (1 - \mathrm{P}) - \mathrm{A} \cdot \mathrm{P_{unsw}} \cdot \mathrm{P} \tag{4.6}$$

In equation (4.6), A is the attempt frequency ($A \sim 1 \times 10^{10}\ Hz$). We can transform the temperature profiles of $P_{sw}(P_{unsw})$ to functions of cooling time using equation (4.7):

$$\mathrm{T} = \mathrm{T_{peak}} - \mathrm{CLR} \cdot \mathrm{t} \tag{4.7}$$

In equation (4.7), T is the temperature when the direction of applied field was reversed. CLR stands for the cooling rate (CLR=100 K/ns in the analytical model). $\mathrm{T_{peak}}$ is the peak temperature from which the system's temperature was cooled linearly. Cooling time t is the time taken cooling from T_{peak} to the field reversal temperature T.

We take the switching probability to be an error function of time:

$$\mathrm{P} = \mathrm{a} \cdot \mathrm{erf}\big(\mathrm{b} \cdot (\mathrm{t} - \mathrm{CTM})\big) + \mathrm{d} \tag{4.8}$$

The first derivative of equation (4.8) is the thermal switching probability distribution shown as equation (4.9):

$$dP/dt = 2ab/\sqrt{\pi} \cdot \exp\left(-b^2 \cdot (t - CTM)^2\right) \tag{4.9}$$

CTM stands for the mean value of cooling time. The second derivative of equation (3) is shown as equation (4.10):

$$d^2P/dt^2 = 4ab^3/\sqrt{\pi} \cdot (CTM - t) \cdot \exp(-b^2 \cdot (t - CTM)^2) \tag{4.10}$$

Detailed numerical analysis shows that magnetization switching out of the global minimum can be neglected, implying that the derivative of equation (4.6) is equation (4.11):

$$d^2P/dt^2 = (P_{sw} + n(t)) \cdot V \cdot (-dP/dt) \tag{4.11}$$

For FePt, $n(t)$ is shown as (4.12):

$$n(t) = [(1 \times 10^7 - 0.33 \times 6.2 \times 10^6 \cdot t^{-0.67}) \cdot (710 - 100t) + (1 \times 10^7 t - 6.2 \times 10^6 \cdot t^{0.33}) \cdot 100 \cdot V]/(k_B \cdot (\mathrm{T_{peak}} - \mathrm{CLR} \cdot \mathrm{t})^2) \quad (4.12)$$

Based on calculations and plots of P_{sw} and equation (4.12), $n(t) \gg P_{sw}$ is satisfied for FePt. Therefore, we neglect P_{sw}. Plots of $n(t)$ shows that it can be approximated by a linear function L(t). Based on the calculation of FePt, $\mathrm{L(t)} = 5.538 \times 10^{19} \cdot t + 4.523 \times 10^{19}$. This yields equation (4.13):

$$d^2P/dt^2 = (-dP/dt) \cdot \mathrm{L(t)} \cdot \mathrm{V} \quad (4.13)$$

If we combine equation (4.9) and equation (4.13), we obtain equation (4.14):

$$d^2P/dt^2 = \left(-2ab/\sqrt{\pi} \cdot \exp(-b^2 \cdot (t - CTM)^2)\right) \cdot \mathrm{L(t)} \cdot \mathrm{V} \quad (4.14)$$

Now, we have two different forms of d^2P/dt^2, namely equation (4.10) and equation (4.14). Upon combining equation (4.10) and equation (4.14), we obtain $b^2 = (\mathrm{c_1} \cdot \mathrm{V} + \mathrm{c_2})$and mean cooling time $CTM(V)$ shown as equation (4.16). Based on the Gaussian distribution in equation (4.9), FWHM (full-width-half-maximum) can be calculated by b (shown as equation (4.15)).

$$\mathrm{FWHM} = 2.35482/\sqrt{2} \cdot \sqrt{(\mathrm{c_1} \cdot \mathrm{V} + \mathrm{c_2})} \approx 508.3/\sqrt{V} \quad (4.15)$$

$$\mathrm{CTM} = c_3/V + c_4 \approx 31.41/V + 1.747 \quad (4.16)$$

These two functions can apply to general HAMR (heat assisted magnetic recording) material if the temperature profile for M_s and K follows $K(T)/K(0) \propto [M_s(T)/M_s(0)]^3$. As shown by the second terms of equation (4.15) and (4.16), the SPD depends strongly on the volume of the FePt grains.

To verify the analytical results for volume dependence of thermal switching field, a micro-magnetic simulation model was established. Using renormalized cells, the thermal switching probability distribution was calculated for FePt storage layers with different volumes. For each calculation, the storage layer was first heated to the peak temperature $T_{peak} = 850K$, then the temperature was decreased linearly with a cooling rate of 100 K/ns. At specific temperatures, the direction of applied magnetic field was reversed. Then the temperature continued decreasing to room temperature (350K). This process was repeated 100 times in order to get the switching probability at a specific reversal temperature. The standard deviation of the basal area of each grain, i.e., standard deviation of volume, was assumed to be zero. The whole procedure was implemented for different reversal temperatures. The SPD can be calculated from the P(T). The same process was implemented to get the SPD of a single writing layer, single storage layer and composite multilayers. The resulting knowledge of the volume dependency of SPD greatly aided the design of the composite structure because it allowed us to quickly narrow the scope of our micromagnetic search, particularly for variables such as layer thickness.

Fig. 4.11 shows the calculated SPD ($\mathrm{dP/dt}$) of FePt storage layers with different volumes. The applied field is $8000\ Oe$ with canting angle 22.5°, the cooling rate is the same as the one used in the analytical model, which is $100\ K/ns$. The peak temperature is 850 K

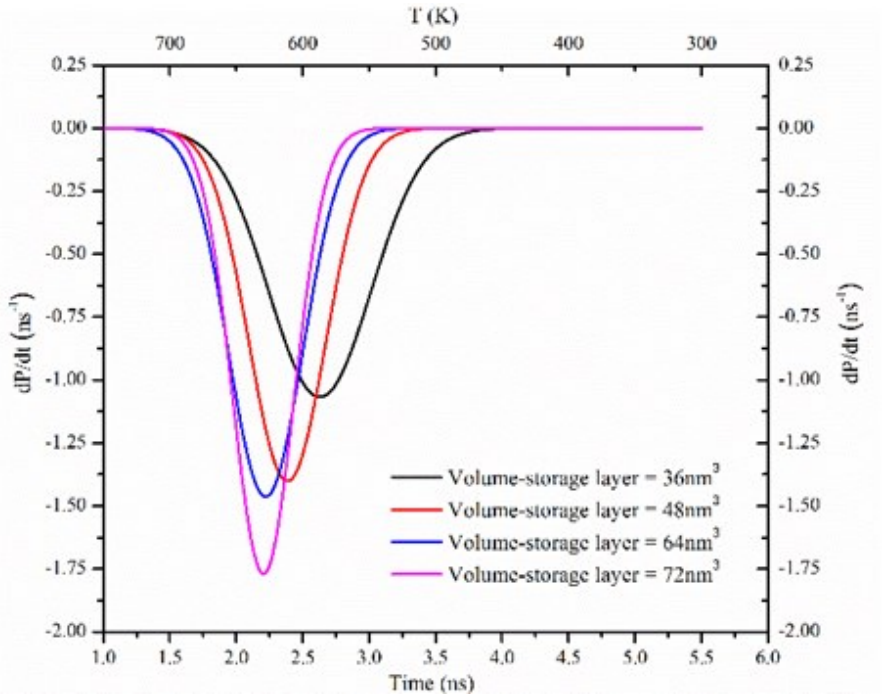

Fig. 4.11 Different colors and symbols represent FePt storage layers with different volumes. It shows the corresponding thermal switching probability distribution

Table 4.2 FWHM and mean under different grain volume

V (nm^3)	FWHM (K)	Mean (ns)
36	90	2.629
48	68	2.385
64	66.4	2.221
72	54.3	2.205
96	45	2.1

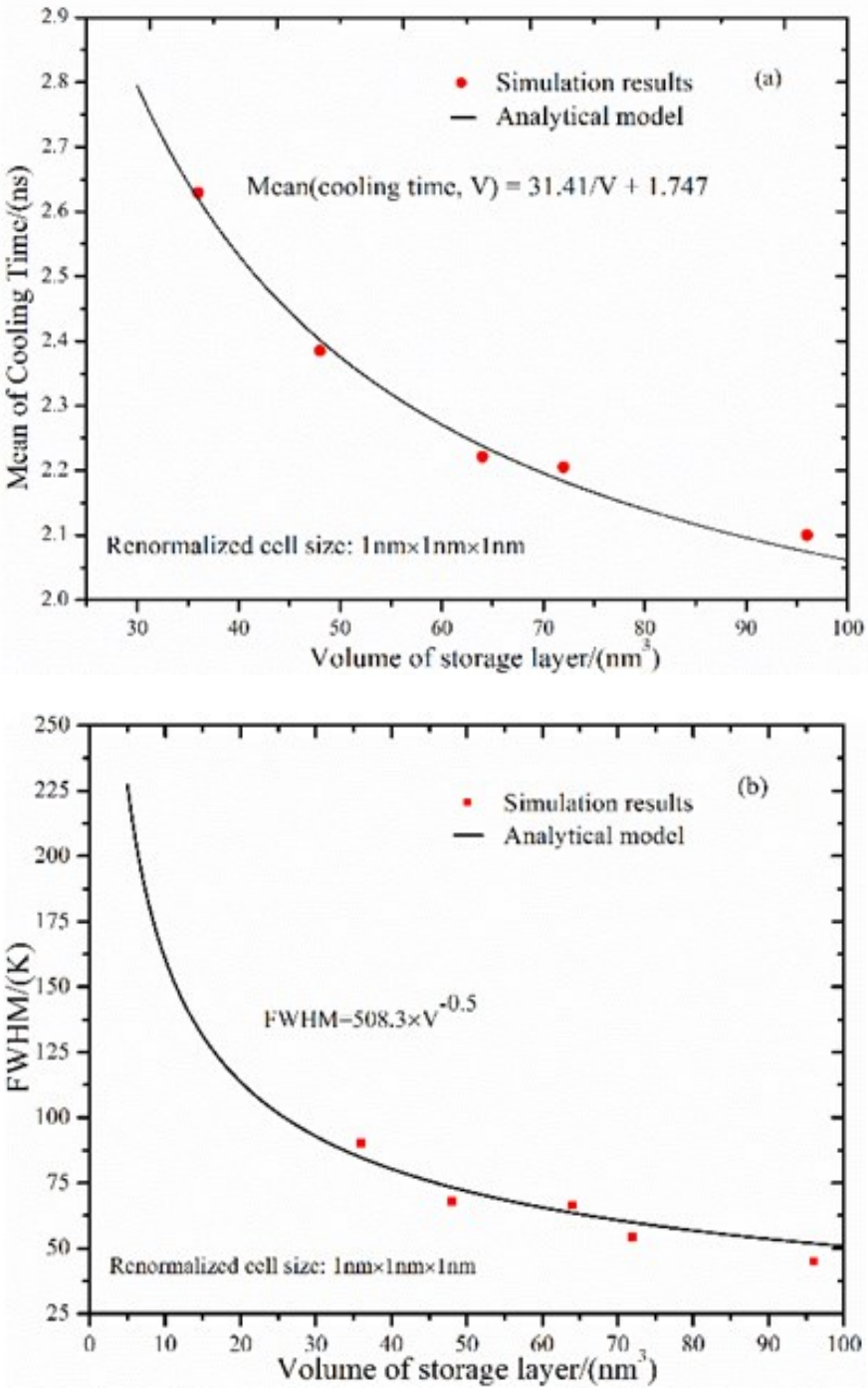

Fig. 12 (a) Mean of cooling time as a function of storage layer volume. Black curve is plotted according to the analytical model. The red circles represent the simulation results (as shown in Table 4.2). (b) Full width at half maximum (FWHM) as a function of storage layer volume. Black curve is plotted according to the analytical model. FWHM=$508.3/V^{0.5}$. The red cubes represent the simulation results (as shown in Table 4.2).

The volume dependency of the mean cooling time and the FWHM calculated by simulation are shown in Table 4.2. The switching temperature (temperature when dP/dt reaches minimum) can be calculated based on the cooling time. The analytical model also indicated that the FWHM and the cooling time mean value should be a function of volume as shown in equation (4.15) and (4.16).

Fig. 4.12 (a) and Fig. 4.12 (b) show the comparison of the results between the analytical model and the simulation using renormalization. The simulated value fitted the functions developed by the analytical model well. With increased storage layer volume, the switching temperature becomes higher and the FWHM is narrower. According to the results in Fig. 4.12 (b), the thermal switching probability distribution of a conventional perpendicular media with 7 nm diameter grains will have FWHM of 30K if the thickness is 10 nm. Further simulation shows that adding a 3% T_c distribution in FePt yields FWHM of 55 K when subjected to a normal HAMR writing process.

4.7 Summary

To summarize this chapter, the thermal switching probability distribution of L10 FePt is fully investigated by using the renormalized method under different renormalized scales. Two important parameters, including FWHM and average write temperature, are obtained to represent each distribution. The recording grain volume dependence of SPD are found: $1/V$ and $1/\sqrt{V}$ law. On the other hand, different noise effects on the SPD are investigated by defining a parameter called σ_{SPD}. It has been verified to have a relationship with transition noise during HAMR recording.

Chapter 5

Composite Media with High Areal Density

Heat Assisted Magnetic Recording (HAMR) is often considered to be the next-generation technology of the information storage industry. Unlike Perpendicular Magnetic Recording, HAMR recording media is not only recorded by a magnetic field but also assisted by heat. HAMR is greatly affected by the Curie temperature (Tc) distribution because writing occurs at temperatures near the Tc of FePt media. To increase the areal density capacity (ADC) of HAMR, noise mitigation is crucial. A HAMR composite media with a superparamagnetic writing layer is proposed. The recording process is initiated in the write layer that is magnetically softer than the long term storage layer. Upon cooling, the composite structure copies the information from the writing layer to the lower Curie temperature (Tc) storage layer, e.g. doped FePt. Advantages include insensitivity to Tc variance in the storage layer, and thus the opportunity to significantly lower the FePt Tc without the resulting Tc distribution adversely affecting performance. The composite structure has small jitter within 0.1 nm of the grain size limit owing to the sharp transition width of the optimized superparamagnetic writing layer. The user density of the composite

structure can reach 4.7 Tb/in^2 for a Gaussian heat spot with Full-Width-At-Half-Maximum of 30nm, 12 nm reader width, and optimized bit length of 6nm

5.1 Previous Composite Media

Different composite structures have been proposed to control the noise caused by the Tc variance. The idea is to utilize phenomena that can provide narrower transition width than that generated by typical Tc variance. For example, FeRh/FePt exchange coupled media benefits from a sharp FeRh phase transition. [61]

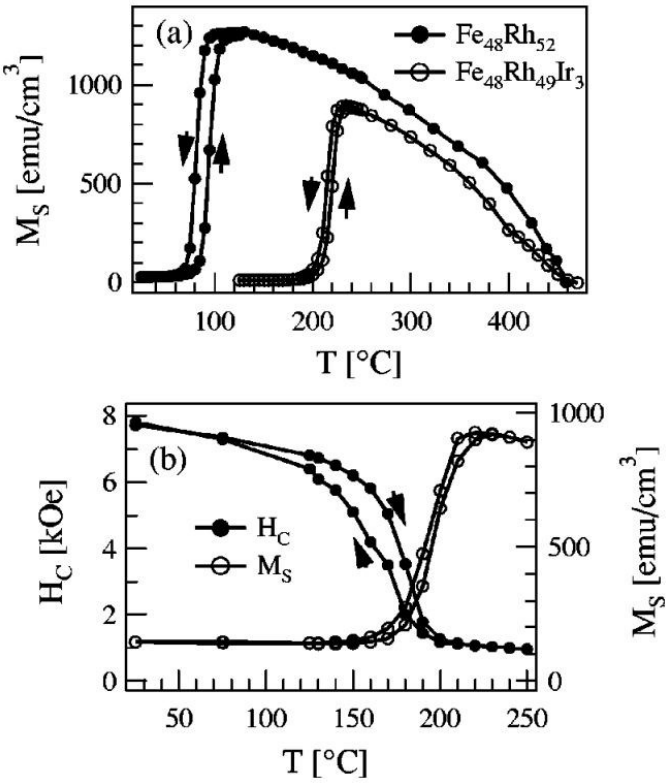

Fig. 5.1 (a) Temperature dependence of saturation magnetization upon heating and cooling of $Fe_{48}Rh_{52}$ and $Fe_{48}Rh_{52}Ir_3$. (b) H_c and M_s of composite FeRh/FePt composite media

This composite media utilizes the FeRh phase transition which is from ferromagnetic phase to antiferromagnetic phase during cooling process. Furthermore, the composite media can work at temperatures considerably lower than the Curie point of FePt. Lower write temperature usually indicates less effects from Curie temperature variance.

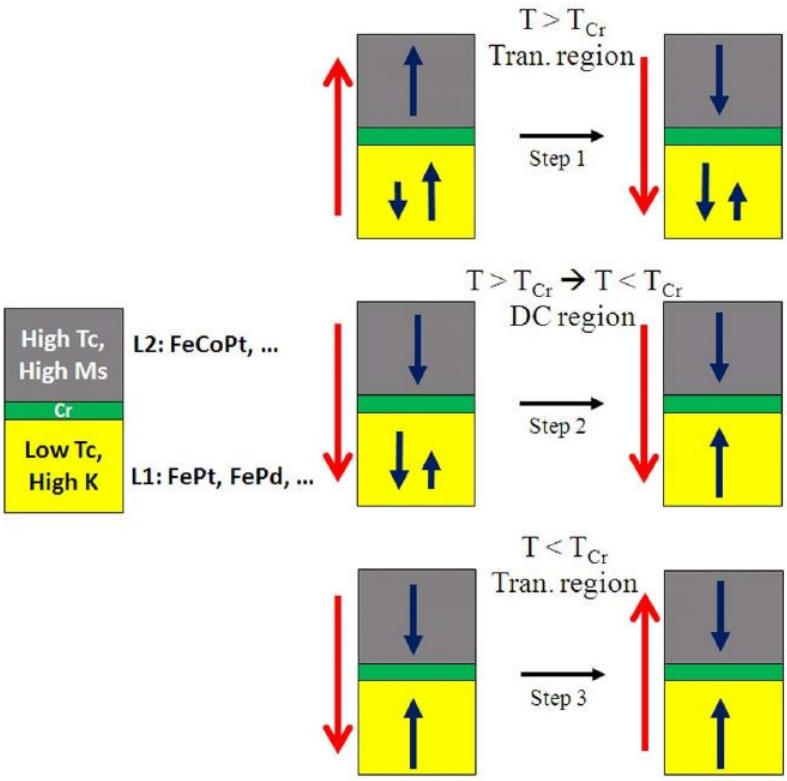

Fig. 5.2 Composite grain with two magnetic layers, L1 and L2, sandwiching a very thin (a few monolayers) Cr layer. The HAMR writing process with this composite grain is shown in three steps. Arrows in the grains show the spin directions in the layers. Multiple arrows in the same layer indicate superparamagnetism. Red arrows by the grains are the head field directions. (Taken from [62])

It is a well-known phenomenon that bulk Cr has an AF ground state due to incommensurate spin-density-wave (SDW) magnetic ordering, with Neel temperature T_N of 311K. The SDW effects is so strong that the magnetic correlations among Cr spins still exist over

several bcc unit cells. [63] This indicates that the state of coupling and non-coupling can be tuned by the thickness of Cr layer. The Neel temperature can also be tuned by doping Mn or V as shown by the reference [64]. Figure 5.2 shows that the FePt/Cr/X/FePt composite structures [62] make use of the sharp AFC (antiferromagnetic coupling) transition provided by the Cr layer. The details of the working process of this composite media can be found in reference [62].

A bilayer structure making use of high Tc material is shown by D. Suess. [65] It consists of a high T_c Fe layer exchanged coupled to a FePt layer. The schematic view of this bilayer structure is shown by Figure 5.3.

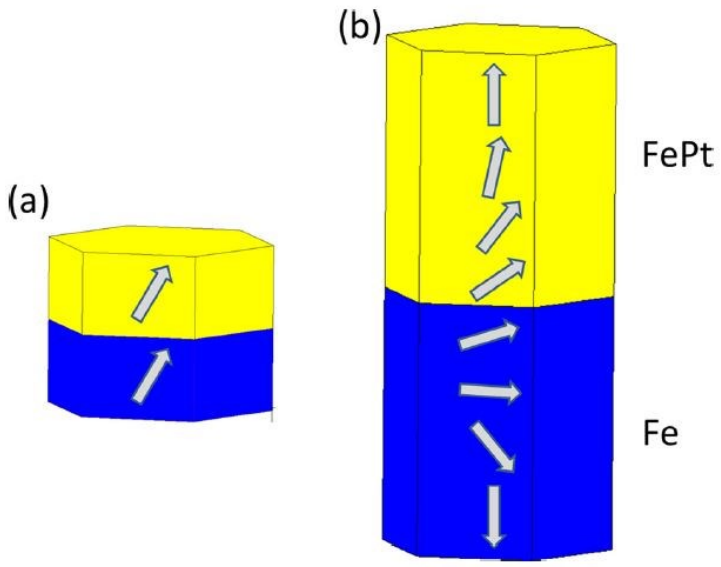

Fig. 5.3 (a) shows the bilayer structure with single domain (two thin layers with thickness less than the calculated domain wall thickness) (b) the bilayer exchange spring media with thickness which is larger than the exchange length (domain wall thickness).

This structure has been verified to benefits from lowering the average write temperature. Lower write temperature indicates less effects from thermal fluctuation and Curie temperature variance. Simulations showed these structures do yield smaller jitter compared to FePt media with varying Tc. [56][65] However, owing to intrinsic experimental variations during fabrication, none of these structures will likely have narrower transition width besides of the Fe/FePt composite media. However, Fe will have problem with demagnetization field and switching speed.

5.2 A New Composite Media Design

A design idea is to decouple the recording problem from the long-term storage issue. This idea relies on a composite structure that has a superparamagnetic writing layer and a (doped) FePt storage layer. The decoupling process requires the composite structure to later copy information (by exchange coupling) to the storage layer from the writing layer during the recording process. To avoid the effects of Tc variance in the FePt storage layer, the recording process must happen at a higher temperature than the writing temperature of the storage layer. To achieve the goal, the Curie temperature of the writing layer should be higher than that of the storage layer. [57][66] At the same time, the anisotropy of the writing layer should be substantially large and the magnetic moments of the write layer must exceed that of the storage layer until writing is completed. In addition, the temperature dependence for the magnetic properties of the writing layer should be optimized to provide a sharp transition width. Thermal switching probability distribution (SPD) has been investigated for FePt media. [57] The results in this paper will examine the potential of the

composite structure to provide a narrower transition width than that found in FePt media with typical Tc variance.

Based on this design idea, a possible case was simulated with the renormalized method. The resulting knowledge of the volume dependency of SPD greatly aided the design of the composite structure because it allowed us to quickly narrow the scope of our micromagnetic search, particularly for variables such as layer thickness. [66] The SPD of the composite media exampale is shown in Figure 5.4.

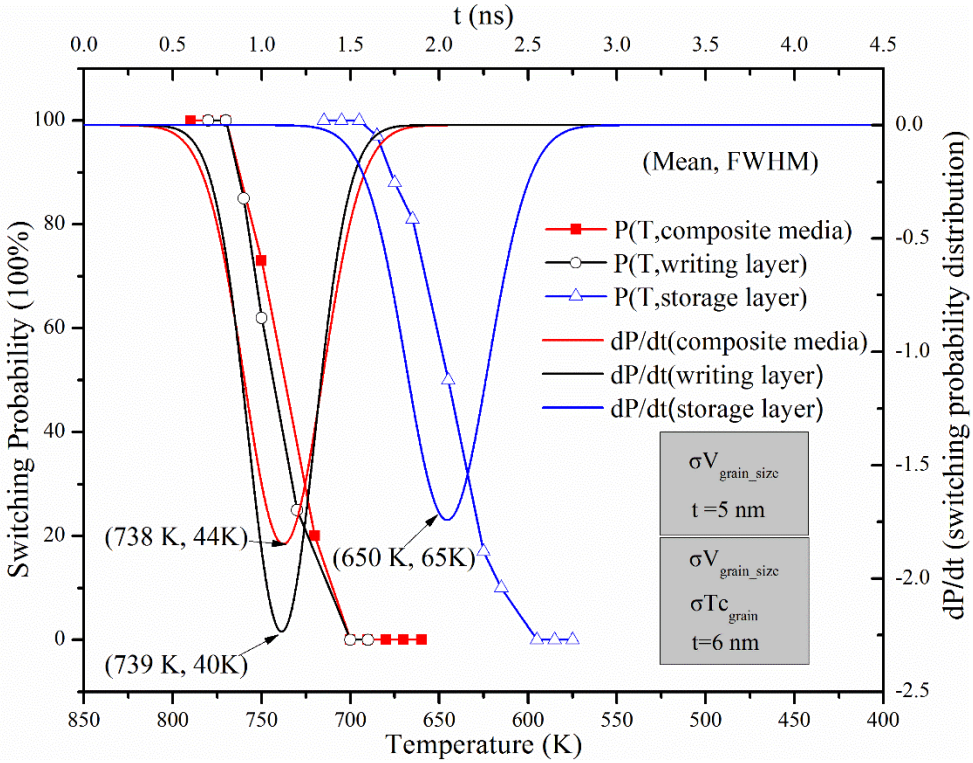

Fig. 5.4 Switching probability (P(T)) calculated for single writing layer, single storage layer and composite structure shown as the different color error-function-like curves. The corresponding thermal switching probability distribution (SPD) has the same color as the P(T). (Mean, FWHM) shows the switching temperature and FWHM for each case. The conceptual figure on bottom right shows the configuration of the composite structure.

Table 5.1 The FWHM and average write temperature under different cooling rate

Cooling Rate (K/ns)	FWHM (K)	Switching Temperature (K)
100	45	738
200	64	720
250	75	714

The FWHM of the single storage layer as shown by the blue curve is 65 K. Black curves show that the writing layer with 6 nm diameter grains (20% grain size distribution added) can yield a narrower FWHM of 40K. The configuration of the composite structure is shown in the bottom right. The thickness of superparamagnetic writing layer is 5 nm ($t_w = 5\ nm$, w stands for "writing layer"). $M_{s,w}(350\text{K}) = 700\ \text{emu}/cm^3$ and $K_{u,w}(350K) = 1.0 \times 10^7\ erg/cm^3$. For FePt storage layer with 6 nm diameter grains, the parameters are $t_s = 6\ nm$, $M_{s,s}(350\text{K}) = 920\ \text{emu}/cm^3$ and $K_{u,s}(350K) = 4.3 \times 10^7\ erg/cm^3$ (s stands for "storage layer"). The storage layer has 20% grain size distribution and 3% Tc variance. We assume both layers have zero H_k distribution. The exchange constant for FePt is $A_{ex,s} = 1.23 \times 10^{-6}\ erg/cm$ which yields a Curie temperature of 710 K. The exchange constant for writing layer is $A_{ex,w} = 1.42 \times 10^{-6}\ erg/cm$ which yields a Curie temperature of 800K. The exchange between the storage layer and writing layer was calculated by the geometric mean of these two exchange constants: $A_{interlayer} = \sqrt{Aex_s \cdot Aex_w}$. The applied field for the simulation is 8000 Oe. The cooling rate is 100 K/ns. The red curves showed that the composite structure successfully copied information

from the writing layer (similar SPD). The final FWHM of the composite structure turned out to be 44 K, which is narrower than 65 K of the conventional FePt HAMR media.

Table 5.1 shows the SPDs of the composite structure calculated under different cooling rates 100 K/ns, 150K/ns and 250K/ns. The FWHM of the SPD varied linearly with cooling rate. Qualitatively, this is the same result as found in reference [56] for the storage layer alone, but the dependence is less severe. The conclusion is that larger cooling rate is detrimental to the superparamagnetic writing process.

To sum up the basic principle of this new composite media design, Figure 5.5 is included.

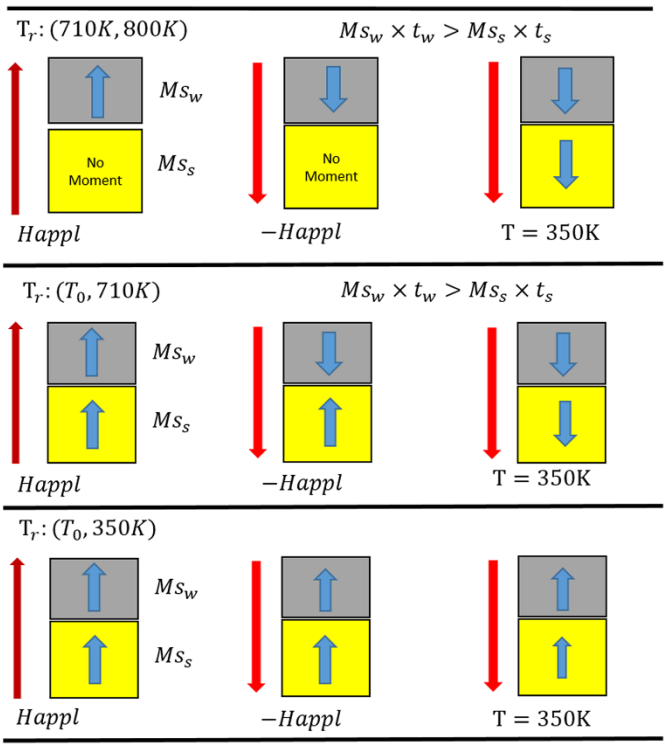

Fig. 5.5 The writing process of the composite media with superparamagnetic writing layer. The writing temperature is higher than the Curie temperature of FePt (about 710K).

T_0 is the temperature at which the composite structure has zero switching probability. For temperatures between the writing temperature T_0 and 800K, it is crucial that the relationship $Ms_w \times t_w > Ms_s \times t_s$ be satisfied. This guarantees that the composite structure will have the same SPD as the writing layer. The substantial anisotropy of the writing layer allows this to occur above the pure FePt write temperature and thus remove the dependence on the Tc variation within the FePt layer. It also significantly lessens the constraints on the writing layer magnetization and thickness. This contrasts with the use of a soft write layer, such as Fe, where the write temperature is very close to the FePt write temperature and its moment (magnetization multiplied by thickness) must be higher [65][67].

5.3 New Composite Media: Magnetic Property

The design of the writing layer with substantially large anisotropy and high Curie temperature is one aspect that distinguishes the bilayer structure from the other bilayer structure designs with different Curie temperatures. [65] The other aspect is that the writing process explicitly uses superparamagnetic writing, which means writing with thermal fluctuations. The writing layer in the composite structure offers another direction of optimization to reduce the noise in the recording media, and reduces the demands on the FePt layer. These distinctive features potentially allow higher user areal density with lower write temperatures than previously demonstrated.

To futher optimize the magnetic properties of the composite media, micromagnetic simulation based on the Landau-Lifshitz-Gilbert (LLG) equation is implemented. [43][47]

The renormalized cell size is$1.5nm \times 1.5nm \times 1.5nm$. The composite structure has two layers, e.g., a 3nm superparamagnetic writing layer and 6nm FePt storage layer. The Curie temperature of the writing layer is 900K. The Curie temperature of the FePt layer is 700K. The Tc variance within the composite structure distributes as $\sigma T_{c,wl} = 0\%$ and $\sigma T_{c,sl} = 3\%$ ("sl" stands for storage layer and "wl" stands for writing layer). Hk variance is assumed to be zero. The Gilbert damping constant of the composite structure is 0.02 at 350K. $M_{s,sl}(350K) = 922.3\ emu/cm^3, K_{u,sl}(350K) = 4.11 \times 10^7 ergs/cm^3$ and $A_{ex,sl}(350K) = 1.1 \times 10^{-6} ergs/cm$. The magnetic profiles of the writing layer are given by equation (5.1), (5.2) and (5.3).

$$M_{s,wl}(\frac{T}{T_{c,wl}})/M_{s,sl}(\frac{T}{T_{c,sl}}) = M_{s,wl}(350K)/M_{s,sl}(350K) \tag{5.1}$$

$$K_{u,wl}(\frac{T}{T_{c,wl}})/K_{u,sl}(\frac{T}{T_{c,sl}}) = K_{u,wl}(350K)/K_{u,sl}(350K) \tag{5.2}$$

$$A_{ex,wl}(\frac{T}{T_{c,wl}})/A_{ex,sl}(\frac{T}{T_{c,sl}}) = T_{c,wl}/T_{c,sl} \tag{5.3}$$

The exchange coupling between these two layers is taken to be $\sqrt{A_{ex,wl} \cdot A_{ex,sl}}$. Different magnetic profiles of the writing layer are produced by various combinations of $M_{s,wl}(350K)$ and $K_{u,wl}(350K)$. Therefore, by changing the magnetization and anisotropy of the writing layer, different writing temperatures (T_w) and FWHMs are obtained from the

calculated SPD. [66] Results for average grain diameter of 5.6nm with 20% standard deviation of diameter are shown in Fig. 5.5.

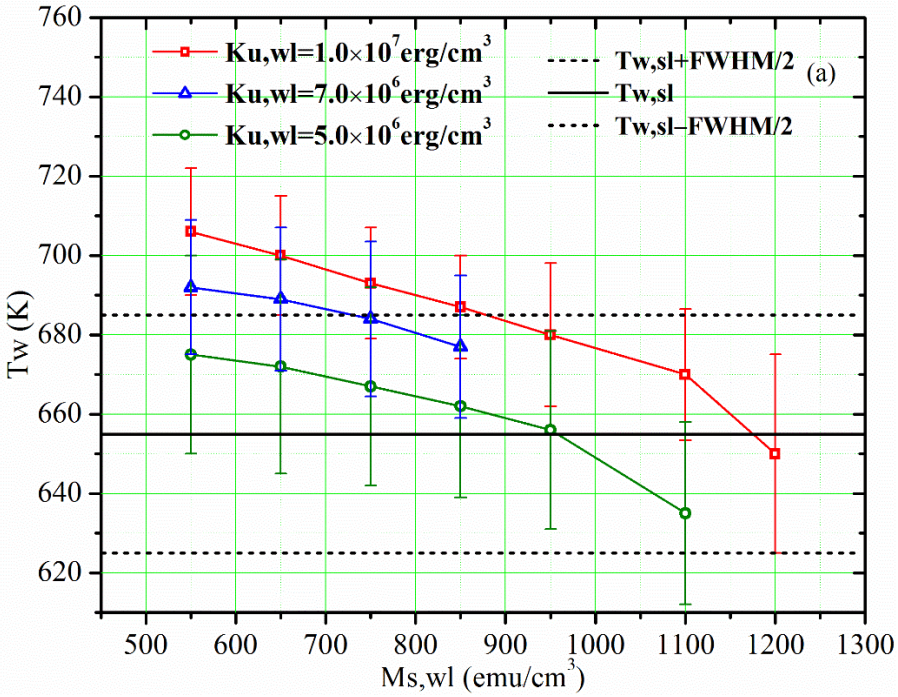

Fig. 5.6 Relationship between Tw of the composite structure and $M_{s,wl}$ for $T_{c,wl}$=900K, cooling rate 100 K/ns.

The error bars represents the FWHM ($T_w \pm FWHM/2$). Based on the results shown in Figure 5.6, writing temperature of the composite structure decreases with increasing magnetization of the writing layer. The composite structure has higher writing temperature when the writing layer has larger anisotropy. The writing temperature is (at most) 710K when $T_{c,wl} = 900K$ and $K_{u,wl} = 1.0 \times 10^7 erg/cm^3$. Therefore, $T_{peak} = 850K$ is sufficiently high to ensure good recording. Protecting the a-C (amorphous carbon) overcoat

constrains the Tc choices of the writing layer. [68] The black lines are based on the SPD of the single FePt layer with 6nm thickness and 3% Tc variance.

The solid line shows the writing temperature of the FePt layer is 655K. The FWHM of the FePt layer is 60K. The dashed lines represent 655K+FWHM/2 and 655K-FWHM/2. In Fig. 5.5, the composite structure has narrower FWHM (small transition jitter) if the writing layer has higher anisotropy. [57][66] The FWHM of the composite structure decreases with increasing magnetization of the writing layer and becomes larger when Tw is lower than 685K. These results contrast the use of a soft layer, such as Fe, where the anisotropy is zero and its moment (magnetization multiplied by thickness) must be higher. [65] Considering the anisotropy and FWHM, the optimized composite structure chosen has 6nm FePt storage layer and 3nm writing layer with $M_{s,wl} = 550\ emu/cm^3$, $K_{u,wl} = 7 \times 10^6\ erg/cm^3$ and $T_{c,wl} = 900$. Potential materials for the superparamagnetic writing layer include variations on conventional perpendicular media. The writing temperature of the chosen composite structure is 692K. The FWHM of it is 37K, which is 38% less than 60K of the FePt media.

5.4 New Composite Media: Transition Jitter Performance

Transition jitter of the functional composite media is calculated by implementing a previously developed Heat-Assisted-Magnetic-Recording simulation that uses CUDA/C based on NVIDIA graphics to accelerate the computation of the magnetic recording process. [43] The write head field is 8000 Oe. The angle between applied field and z direction is 22.5°. The thermal field delivered by the near field transducer on the media is modeled by a 2-D Gaussian distribution. [69][70] The FWHM of the thermal profile is

40nm in cross-track and down-track direction. The equivalent thermal gradient is about 15K/nm. The bit length is 21 nm and the recording pattern is a single tone. The peak temperature (T_{peak}) of thermal field is 850K. The head velocity is 20 m/s. The σHk distribution and σT_c distribution are the same that were used in the SPD calculation. The transition jitter of the composite structure is calculated based on 200 zero crossings of the play back signal. The nonmagnetic grain boundary (Bnd) is assumed to be 1nm. The reader width WR=20 nm. The magnetic flying height is 6nm. The shield to shield distance is 11nm. The noise from the reader is assumed to be zero. The results are shown in Fig. 5.6 (a). The blue curve represents the jitter of the composite structure optimized by SPD calculation. For comparison, the transition jitter of 6nm FePt media and 9nm FePt media are also calculated. The dashed curve is the grain-size theoretical limit, [25] which follows equation (5.4).

$$\sigma^2{}_{jitter,theory} = \frac{1}{WR/D} \cdot \frac{D^2}{12} \tag{5.4}$$

In equation (5.4), D stands for the grain pitch, which is <D>+Bnd (<D>: grain diameter). The jitter of single FePt media shows that 3% Tc variance is detrimental to the recording process. For example, the gap between single FePt layers and theoretical value is 0.4-0.5 nm. The blue curve shows that the jitter of the media is greatly reduced by introducing the superparamagnetic writing layer. The difference with theoretical limit is only 0.2nm. However, the jitter deviates from the expected value when the recording grain pitch is

smaller than 4.8nm. This is due to thermal fluctuations of the small grains causing DC noise. The DC noise can be mitigated by increasing the thickness of both layers.

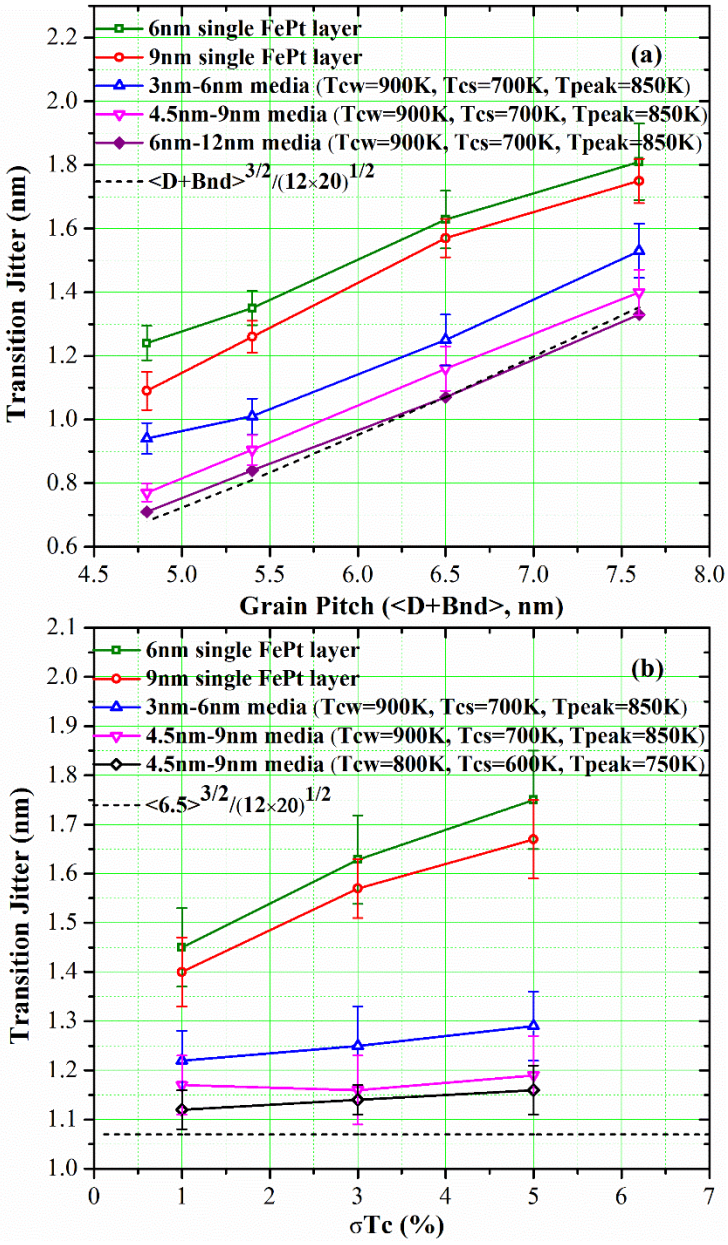

Fig. 5.7 (a) The relationship between transition jitter and grain pitch. The curves with different colors correspond to different structures. The black dashed line represents the grain size limited jitter values under different grain pitches (based on equation (4)). (b) Relationship between the calculated transition jitter and Tc variance in FePt layer.

At the same time, the ratio of the layer thickness remains unchanged (3nm/6nm=0.5). This ensures the relationship between magnetic moment of two layers is identical to that of 3nm-6nm structure (3nm: writing layer, 6nm: FePt layer) during the recording process. Two composite structures with 4.5nm-9nm configuration and 6nm-12nm configuration are examined. With bigger total volume, these two composite media have even smaller jitter.[8] The 4.5nm-9nm one has only 0.1nm bigger jitter than theoretical value and it removes the DC noise existing in 3nm-6nm structure. The 6nm-12nm composite structure approaches the theoretical limit under all grain pitches used. The 4.5nm-9nm composite structure is taken to be the optimized media owing to its reasonable total thickness (13.5nm) and smaller jitter when grain pitch is 4.8nm.

Using the Voronoi grains that have average diameter of 5.5nm and nonmagnetic grain boundary of 1.0nm, results for transition jitter under different Tc variance in the FePt layer are shown in Fig. 5.7 (b). The FePt traditional HAMR media has larger jitter (worse recording density) when σT_c is bigger. The transition jitter of the two composite structures are much smaller than that of single FePt media. The jitter is only 0.1nm~0.2nm bigger than theoretical limit. Furthermore, the transition jitter of the composite structures remains almost unchanged even under different Tc variance in FePt layer. This is due to the superparamagnetic writing process: the composite structure copies information from the writing layer, which make the whole system be impervious to the σT_c in FePt storage layer. Significant doping of FePt can be used to reduce FePt Curie temperature at the cost of reduced archival stability and, typically, increased Tc distribution. However, even reduced anisotropy will still be archival at grain sizes likely to be commercially accessible and our

proposed composite structure removes the jitter dependence on storage layer Tc distribution. The black solid curve in Fig. 5.7 (b) represents the composite media in which the Curie temperatures of both layers and the peak temperature are scaled down by 100K. The magnetic properties of the composite structure are scaled based on the temperature dependence for the anisotropy field of FePt with different Curie temperature (by doping Ni-content). [71] Here, the anisotropy is assumed to be proportional to the Curie temperature. When $T_{peak} = 750K$, the structure still works well with even smaller jitter. In conclusion, besides being unaffected by σT_c in FePt layer, the composite structure can also decrease the writing temperature. Thus, two major HAMR media concerns are addressed.

5.5 New Composite Media: User Density

The proposed composite structure increases the storage capacity due to the decreased transition jitter. To achieve higher storage capacity, small grain pitch, e.g., recording grains with 3.8nm diameter and 1nm nonmagnetic grain boundary, should be used. The functional composite structure chosen is 4.5nm-9nm owing to the good jitter performance even using very small grains. The user density is defined as an evaluation parameter to optimize the whole HAMR system, including the recording media design, recording process and reader configuration. The recording parameters that affect the user density are FWHM of the heat profile and the recording bit length (BL). The Shannon Capacity (C) is calculated based on bit error rate (BER). [72][73] The EBR (effective bit ratio) is defined by C/BL. User density (UD) can be defined as EBR/FWHM. [72]

Table 5.2 SNR, BER and EBR under Different BLs and FWHMs

BL (nm)	FWHM (nm)	SNR(dB)	BER	C/BL (nm^{-1})
4	30	8.6($\pm$1.1)	0.1492	0.098
4	40	9.1($\pm$0.7)	0.1254	0.114
6	30	11.2($\pm$0.7)	0.0077	0.156
6	40	12.3($\pm$0.5)	0.0058	0.158
8	30	13.7($\pm$0.4)	0.0052	0.119
8	40	13.5($\pm$0.8)	0.0049	0.119
10	30	14.6($\pm$0.7)	0.0044	0.096
10	40	15.2($\pm$1.0)	0.0039	0.096

To calculate the bit error rate (BER), a pseudo random bit sequence (PRBS) is recorded. The noise from the reader is assumed to be zero. The SNR is calculated based on $SNR = \int \overline{V(x)^2}dx / \int \overline{\delta V(x)^2}dx$. The V(x) stands for the play back signal voltage along down track direction. The BER is calculated using a 1-D MMSE (minimum mean square error) equalizer and improved Viterbi detector. [74][75] The target function $G = [g_0, g_1, \dots, g_{L-1}]^T (g_0 = 1, L = 3)$ and the equalizer function $F = [f_{-K}, f_{-K+1}, \dots, f_0, \dots, f_K]^T$ are determined by minimizing the difference between the equalized signal and the ideal signal. The total equalizer length is (2K+1)BL, which should remain constant (around 80nm) for different BL. The Viterbi detector and decoder are used to determine the states ("0" or "1") of the signals. [76] The results of BER, SNR and EBR under different recording parameters are shown in Table 5.2. The reader width is taken to be ½ of the FWHM. Table 5.2 shows the composite structure can reach maximum user density when FWHM of heat profile is 30nm and recording bit length is 6nm. Based on EBR/FWHM, the maximum user density is 3.4 Tb/in^2.

Table 5.3 User Density Under Different CTCD using 15nm Reader Width

CTCD (nm)	SNR (dB)	BER	C/BL (/nm)	UD (Tb/in^2)
30	11.2(±0.7)	0.0077	0.1558	3.4
27	11.1(±0.5)	0.0083	0.1551	3.7
24	11.1(±0.6)	0.0113	0.1518	4.1
21	11.1(±0.7)	0.0106	0.1525	4.7
18	10.2(±0.7)	0.0521	0.1175	4.2

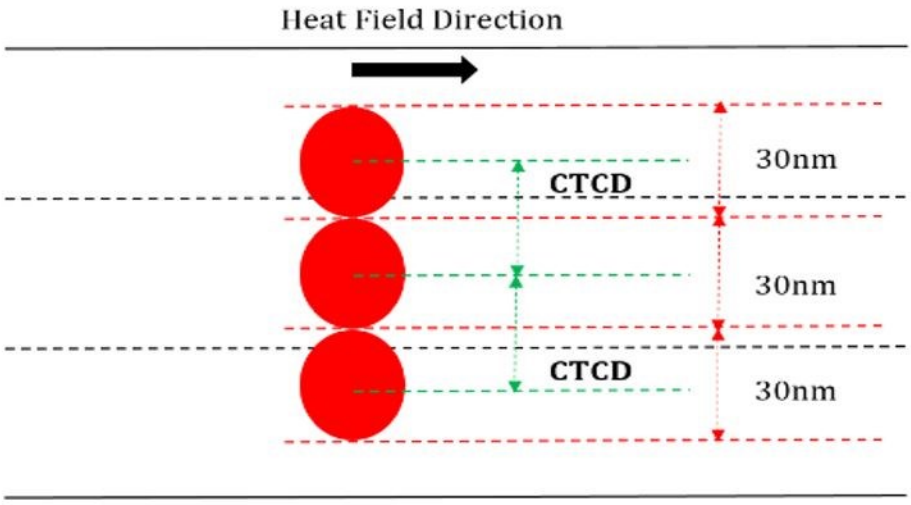

Fig. 5.8 Illustration of overlapping adjacent tracks to maximize the user density. The extent of squeezing is specified by the CTCD (center to center distance). The red spot represents the heat profile with 30nm FWHM. The head direction is along the down track. The recording patterns of central track are used for playing back.

In order to continue to maximize the user density of the composite structure, the adjacent tracks are allowed to overlap each other. This idea is illustrated in Fig. 5.8. The FWHM of the heat profile and the recording bit length are set to be the optimal case in Table 5.2. The three tracks use the same heat profile, but different pseudo random bit sequence, to mimic recording on adjacent tracks. The CTCD stands for center to center distance of two adjacent tracks. The smaller CTCD means larger overlap of two adjacent tracks. Using different

CTCD values, SNR, BER, and effective bit ratio (EBR) are calculated in order to find the optimal CTCD that maximizes the user density. The results for reader width of 15nm are shown in Table 5.3. To calculate the user density, the FWHM should be changed to CTCD. The overlap of two adjacent tracks can be as large as 9nm for the composite structure before the user density starts to decrease.

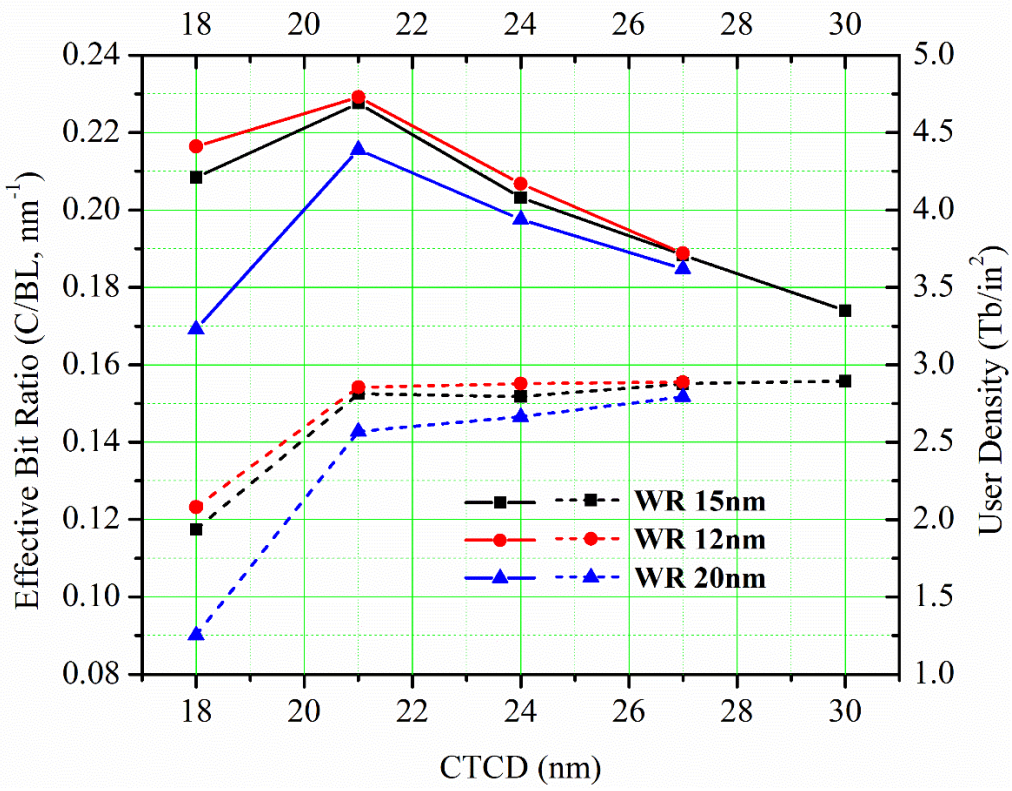

Fig. 5.9 The effective bit ratio (C/BL, dashed) and user density (solid) under different CTCD. Different colored curves corresponds to three different reader widths (WR).

To optimize the reader configuration under different CTCD, the effective bit ratio and user density are calculated as Table 5.3 under different reader width, including 12nm, 15nm and 20nm. The results are shown in Fig. 5.9. The dashed lines show the results for effective bit

ratio. The abrupt decrease of all three dashed curves when CTCD is smaller than 21nm is due to the recording patterns of the central track being distorted by the adjacent tracks as shown in Fig. 5.10.

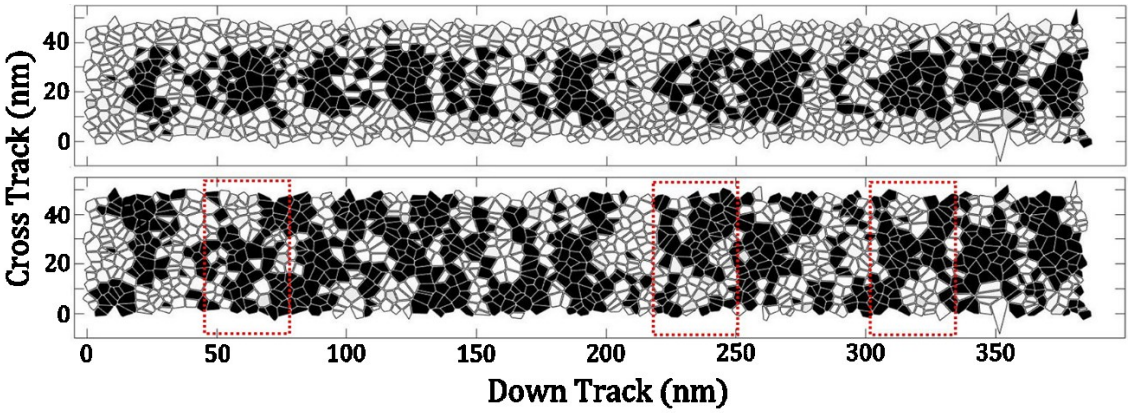

Fig. 5.10 Recording patterns of central track under no overlap (top one) and CTCD=18nm (bottom one). These two cases use the same PRBS pattern for central track. Regions enclosed by red rectangles illustrate the distortion of the patterns on the central track.

This also results in decreased user density. The solid lines show the results of user density. It continues to increase with decreasing CTCD due to almost unchanged effective bit ratio, when CTCD is bigger than 21nm. Both the user density and effective bit ratio show that the results saturate when the reader width continue to decrease. For example, the results under reader width of 15nm and 12 nm are almost the same. The maximum user density can reach 4.7 Tb/in^2. Thus, using this technique, the user density can be increased by 40% without making any changes to the original HAMR recording head configuration.

In conclusion, a composite structure with a 4.5nm superparamagnetic writing layer and a 9nm FePt storage layer is proposed. The transition jitter of the proposed composite structure approaches the grain-size theoretical limit and is impervious to the Tc variance in

FePt layer. A reduced writing temperature is demonstrated. Under 30nm FWHM of heat profile, 6nm bit length, 21nm CTCD, and 12nm reader width, the user density of the proposed composite structure can reach 4.7 Tb/in^2.

5.6 New Composite Media: Interlayer Exchange Coupling

Micromagnetic simulation is used to calculate the temperature derivative of the switching field dH_{sw}/dT for a composite media with a superparamagnetic writing layer. The results show that dH_{sw}/dT is reduced for a defined probability of switching, and switching field line width remains almost unchanged. An analytical two-spin model is established to relate exchange coupling between the two layers J_{ex} to energy barrier and the switching probability distribution (SPD). Both the analytical model and micro-magnetic simulation show that the full-width half-maximum $FWHM \propto (J_{ex})^{-0.5}$ and writing temperature $T_{sw} \propto (J_{ex})^{-1}$. It is also found that the writing layer leads the storage layer during switching.

Both the switching field gradient dH_{sw}/dT and switching field line width σH_{sw} can affect the transition noise. [77] To enable comparison with FePt and Fe/FePt composite media, these two parameters were evaluated using a renormalization approach. [43] The renormalized cell size is $1.5nm \times 1.5nm \times 1.5nm$. The micro-magnetic simulation is based on the Landau-Lifshitz-Gilbert (LLG) equation. The thicknesses of the layers are $(t_w = 4.5nm,\ t_s = 9.0nm)$ or $(t_w = 3.0nm,\ t_s = 6.0nm)$ where "w" stands for the writing layer and "s" stands for the storage layer. $Ms_w(350K) = 550emu/cm^3$, $Ms_s(350K) = 922\ emu/cm^3$, $Ku_w(350K) = 7.0 \times 10^6 erg/cm^3$ and $Ku_s = 4.11 \times$

$10^7 erg/cm^3$. The Curie temperature of writing and storage layer are 900K and 700K. We use the same scaling approach as described in reference [58]. The exchange coupling between these two layers is $A_o = \sqrt{Aex_s(T) \cdot Aex_w(T)}$.

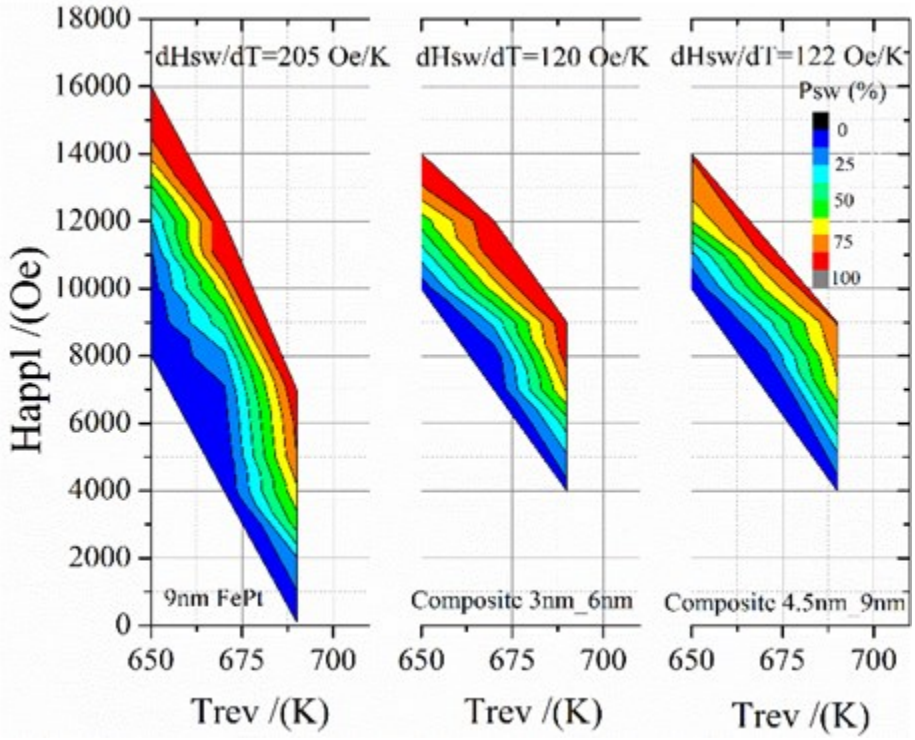

Fig. 5.11 dH_{sw}/dT for single FePt layer, 3nm-6nm composite media and 4.5nm-9nm composite media.

The thermal switching probability (P) is calculated using the same single grain approach ($\sigma T_c = 0$) as references [57] and [66]. The composite media is first heated to a peak temperature ($T_{peak} = 850K$). Then a linear cooling (CR=100K/ns) is applied to the system to reach room temperature. At the specific temperature T_{rev}, the applied field reverses its direction. The process is repeated 100 times to get the switching probability P for each T_{rev} and applied magnetic field H_{appl}. We can get a contour plot based on H_{appl}, T_{rev} and P

(Fig. 5.10). The dH_{sw}/dT is calculated as the slope of two points in the contour plot where the switching probability is 50%. The dH_{sw}/dT of both composite media are about $120\ Oe/K$, which is 5 times larger than that of Fe/FePt. [65] The single layer FePt with 9nm thickness has larger dH_{sw}/dT but almost equal distance between the 10th and 90th switching percentiles which means similar σH_{sw} for a collection of grains with no Tc dispersion. [78]

5.6.1 Analytical Model for Interlayer Exchange Coupling Effects

A quick estimate of transition noise (jitter) in Heat Assisted Magnetic Recording (HAMR) is FWHM (full-width half-maximum) of thermal switching probability distribution (SPD). [58][66] To set up an analytical model of SPD, the energy barrier calculation is critical. [66] Several different approaches have been used to calculate the energy barrier in composite media for perpendicular magnetic recording (PMR). [79][80][81][82] To investigate the exchange coupling effects on HAMR composite media, the energy barrier is calculated with a two-spin model that is similar to that for PMR. [82]

In the proposed two-spin model, each grain is represented by a single spin. Both the writing grain and storage grain have perpendicular easy axis. Therefore, the total energy E_d of the composite grain with a uniform applied external field H is shown as equation (5.5).

$$E_d(T) = -J_{ex}(T) \cdot \cos(\theta_s - \theta_w) + K_s(T) sin^2(\theta_s) \cdot V_s + K_w(T) sin^2(\theta_w) \cdot V_w + M_s(T) \cdot H \cdot cos\theta_s \cdot V_s + M_w(T) \cdot H \cdot cos\theta_w \cdot V_w \quad (5.5)$$

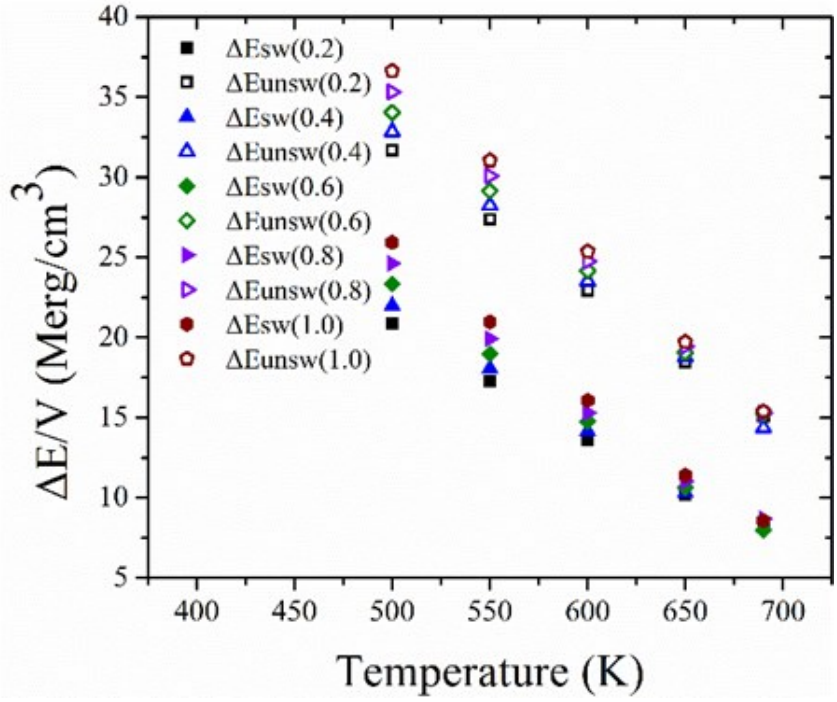

Fig. 5.12 Relationship between energy barrier ΔE and temperature for both switching (sw) and unswitching (unsw) for various Jex/Jo from 0.2 to 1.0. Different color corresponds to different exchange coupling constant.

Here, V is the total volume ($V_s + V_w$). The ratio of layers thicknesses remains as $t_s/t_w = 2$. $\theta_s(\theta_w)$ are the angles between $M_s(M_w)$ and H. The magnetic properties of the storage layer (FePt) are taken from our previous single layer analytical model. [66] $M_s(T) = 136 \times (710 - T)^{0.33} emu/cm^3$ and $K_s(T) = 1.0 \times 10^5 \times (710 - T)\ erg/cm^3$. We use the same scaling model in reference [58] to get the magnetic properties of writing layer. Our reference exchange coupling is $J_o(350K)/V = 9.0 \times 10^6\ erg/cm^3$.

The variation of magnetic properties under different temperature makes the energy barrier calculation more complex. By changing θ_w and θ_s from 0 to π, different energy contour plots at temperature T can be found by using different Jex in equation (5.5). [82] For each contour plot, there are one energy maximum (E_{max}) and two different energy minima

(E_{min1}, E_{min2}). $\Delta E_{sw} = E_{max} - E_{min1}$ is the energy barrier if the magnetization needs to be switched to align with the applied field. [83] $\Delta E_{unsw} = E_{max} - E_{min2}$ is the energy barrier if the magnetization opposes the applied field. This is repeated at different temperatures to get Fig. 5.12.

Fig. 5.12 shows that, if the temperature is higher than 500K, these two energy barriers $\Delta E_{sw,unsw}$ have linear dependence on the temperature with different exchange coupling J_{ex}/J_o. Therefore, we obtained equation (5.6) and (5.7) by linearly fitting the data in Fig. 5.11. Temperature (T) and cooling time (t) are related by $T = T_{peak} - CR \cdot t$.

$$\Delta E_{sw} = (a_{sw}T + c_{sw}) \cdot V = k_{sw}t + b_{sw} \tag{5.6}$$

$$\Delta E_{unsw} = (a_{unsw}T + c_{unsw}) \cdot V = k_{unsw}t + b_{unsw} \tag{5.7}$$

Here, $a_{sw,unsw}$ and $c_{sw,unsw}$ are fitting parameters taken from Fig. 5.11, and $k_{sw,unsw} = -a_{sw,unsw} \cdot CR \cdot V$, and $b_{sw,unsw} = (a_{sw,unsw} \cdot T_{peak} + c_{sw,unsw}) \cdot V$. The total volume V, peak temperature T_{peak} and cooling rate CR remain constant.

When the magnetic field is switched at a particular time t, the probability of each switch becomes $P_{sw} = e^{-(k_{sw}t + b_{sw})/k_B T}$ and $P_{unsw} = e^{-(k_{unsw}t + b_{unsw})/k_B T}$. The probability P of field alignment evolves with time as

$$dP/dt = A \cdot P_{sw} \cdot (1 - P) - A \cdot P_{unsw} \cdot P \tag{5.8}$$

Where A is the attempt frequency ($A \sim 1 \times 10^{10}\ Hz$).

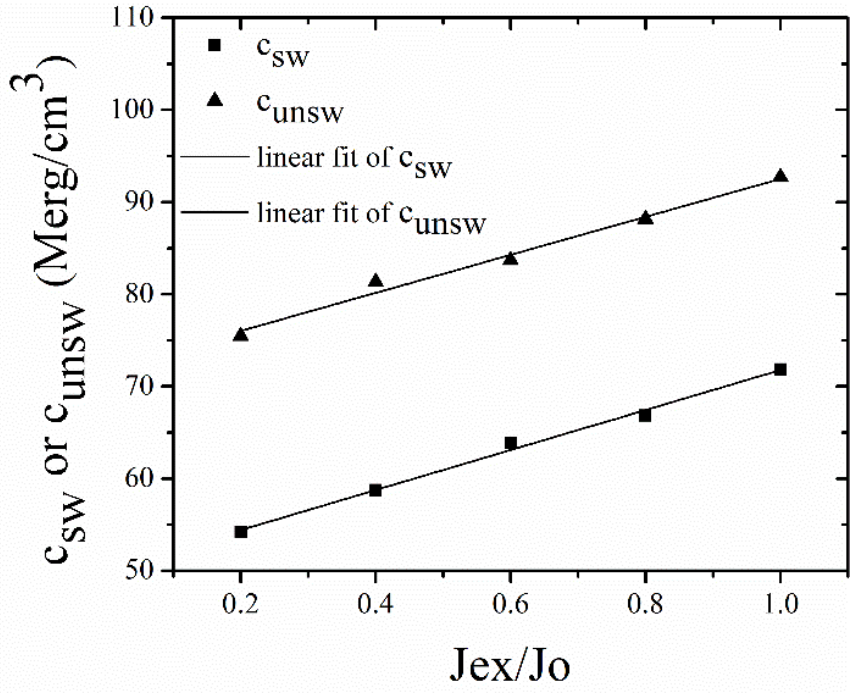

Fig. 5.13 Relationship shows linear dependence of C_{sw} and C_{unsw} on exchange coupling strength J_{ex}/J_o.

Based on Fig 5.12, $b_{sw} < b_{unsw}$. The plots show that $P_{sw} \gg P_{unsw}$ can be satisfied for different Jex/Jo. Therefore, the first derivative of (5.8) can be written as

$$d^2P/dt^2 = (-dP/dt) \cdot f(t) \tag{5.9}$$

$$f(t) = 10^2 e^{-\frac{k_{SW}t + b_{SW}}{k_B(T_{peak} - CR \cdot t)}} + 10\left[\frac{k_{sw} \cdot T_{peak} + b_{sw} \cdot CR}{k_B(T_{peak} - CR \cdot t)^2}\right]\text{GHz} \tag{5.10}$$

By using equations which relate k_{sw} (b_{sw}) to $a_{sw}(c_{sw})$, numerical experimentation under different k_{sw} and b_{sw} (different Jex/Jo) shows that $f(t)$ can be written as:

$$f(t) = c_{sw}(J_{ex}/J_o) \cdot l(t) \tag{5.11}$$

Fig. 5.13 shows $c_{sw} \propto J_{ex}/J_o$ and is independent of time. Numerical results also show that $l(t)$ is an identical linear function which is independent of k_{sw}, b_{sw} and J_{ex}. To get another expression of d^2P/dt^2 instead of equation (5.9), previous experience shows P(t) can be taken as an error function. Therefore, dP/dt is the SPD and follows the Gaussian distribution:

$$dP/dt = m \cdot \exp(-n \cdot (t - mean)^2) \tag{5.12}$$

Here m and n are constant parameters. The "mean" stands for mean value of cooling time. The first derivative of equation (5.12) is shown as

$$d^2P/dt^2 = 2n \cdot (t - mean) \cdot (-dP/dt) \tag{5.13}$$

Thus, we have two different expressions of d^2P/dt^2 shown as equation (5.9) and (5.13). By equating the right parts of (5.9) and (5.13), we can relate "n" or "mean" to Jex/Jo by using equation (5.11). $FWHM = 2.35482/\sqrt{2n}$ based on Gaussian distribution and the

writing temperature is defined as $T_{sw} = T_{peak} - CR \cdot mean$. In the end, FWHM and T_{sw} can be written as functions of Jex/Jo shown as equation (5.14) and (5.15).

$$FWHM \approx 7.9 + 10.6/\sqrt{(J_{ex}/J_o)} \tag{5.14}$$

$$Tsw \approx 698 - 17.8/(J_{ex}/J_o) \tag{5.15}$$

5.6.2 Simulation Results of Interlayer Exchange Coupling Effects

To verify the analytical results, a micro-magnetic simulation is applied to the composite media. All the parameters are the same as the dHk/dT calculation. The applied magnetic field is 8000 Oe. With different exchange coupling, we can get the FWHM and T_{sw} from the corresponding SPD of HAMR composite media by using the same method in reference [84]. The results are shown as the black points in Fig. 5.13. The simulated value matches the functions developed by the analytical model well. Both of them tell us that larger exchange coupling gives narrower FWHM. However, higher writing temperature will induce more noise caused by Tc variance. Therefore, to reduce the transition noise, exchange coupling should be optimized to balance the FWHM and writing temperature. If we continuously increase the exchange coupling, the effects from it tends to saturate according to the analytical functions shown in Fig. 5.13. The results of the analytical model are shown as red curves in Fig. 5.13 (a) and 5.13 (b).

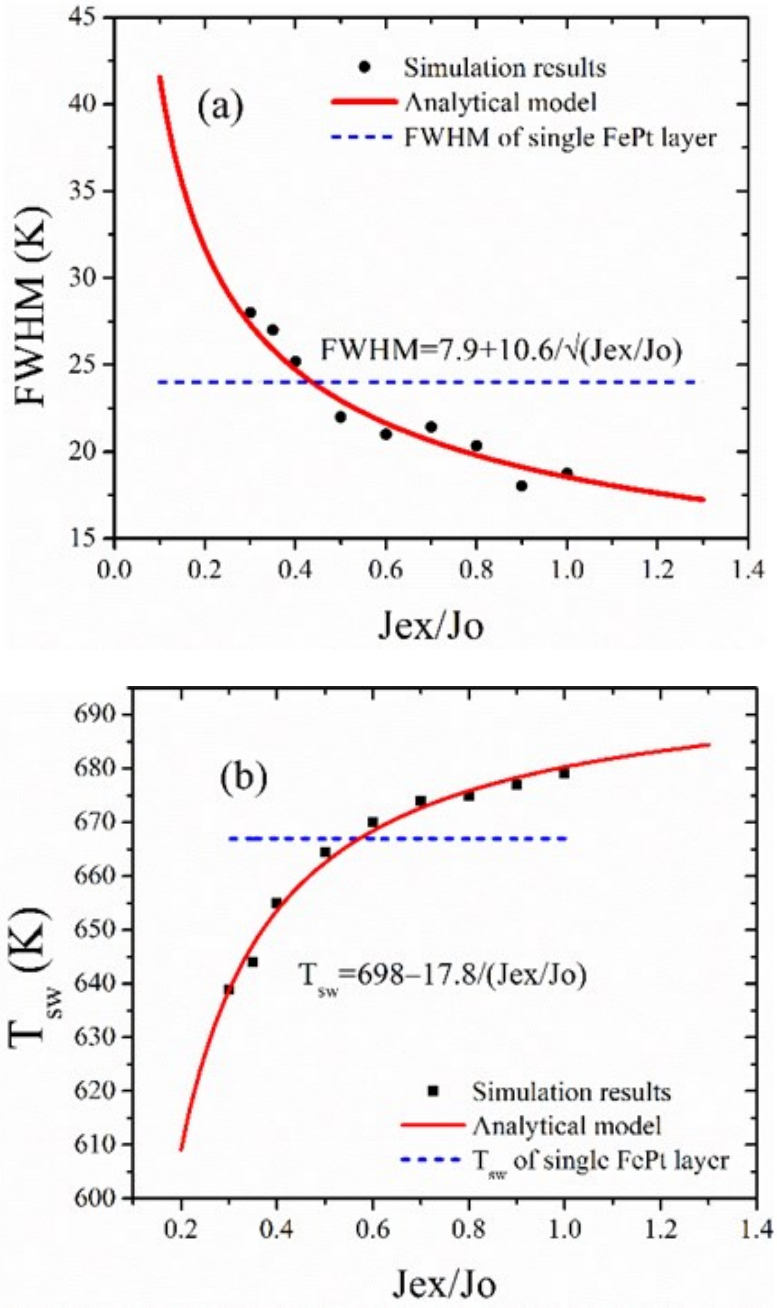

Fig. 5.14 (a) shows the relationship between FWHM and exchange coupling strength. (b) shows the relationship between T_{sw} and exchange coupling strength. The thickness of single FePt layer is 9.0nm.

We also investigated the detailed switching process of both layers during micro-magnetic simulation. One example is shown in Fig. 5.14. M_z is the angle between magnetic moment and easy axis. $\langle M \rangle$ is calculated by $\sqrt{\langle M_x \rangle^2 + \langle M_y \rangle^2 + \langle M_z \rangle^2}$. The evolution of θ_z with time shows that the writing layer leads the storage layer during switching. Fig. 5.15(b) reveals a very brief (0.05ns) dip in the magnetization of the storage layer near 650K. This precedes the actual switch that occurs at full magnetization and appears to be coherent. This interesting effects needs further investigation.

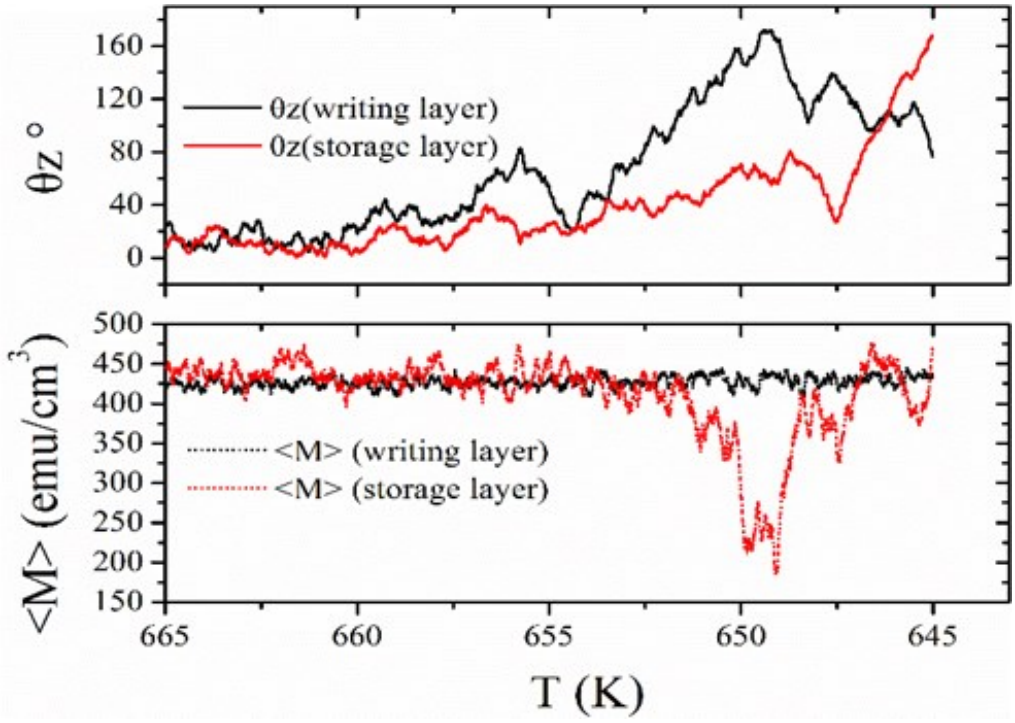

Fig. 5.15 The switching process of magnetic moment (θ: angle between magnetic moment and easy axis). $T_{rev} = 660K$.

5.7 Summary

A composite media design with a superparamagnetic write layer and L10 FePt storage layer is proposed to mitigate the noise. The simulation results show that this structure can greatly decrease the transition noise and be insensitive to the Curie temperature variance in the L10 FePt storage layer. The areal density can reach as high as 4.7 Tb/in^2 for a Gaussian heat spot with a full-width-at-half-maximum of 30 nm, a 12 nm reader width, and an optimized bit length of 6 nm [1]. Further investigation also finds that the interlayer exchange coupling plays an important role in tuning the average write temperature and effects from thermal fluctuation.

Bibliography:

[1] H. J. Richter, “The Transition from Longitudinal to Perpendicular Recording”, J. Phys. D: Appl. Phys. 40 (2007).

[2] H. N. Bertram and K. Z. Gao, “Magnetic recording configuration for densities beyond 1 Tb/in2 and data rates beyond 1 Gb/s”, IEEE Trans. Magn. vol. 38, p. 3675 (2002).

[3] J. P. Wang, Y. Y. Zhou, C. H. Hee, T. C. Chong, and Y. F. Zheng, “Approaches to tilted magnetic recording for extremely high areal density”, IEEE Trans. Magn. vol. 39 p. 1930 (2003).

[4] R. H. Victora and X. Shen, “Exchange Coupled Composite Media”, Proceedings of the IEEE vol. 96, no. 11 (2008).

[5] R. H. Victora and X. She, “Composite Media for Perpendicular Magnetic Recording”, IEEE Trans. Magn. vol. 41 p. 537 (2005).

[6] J.-P. Wang, W. Shen and J. Bai, “Exchange Coupled Composite Media for Perpendicular Magnetic Recording”, IEEE Trans. Magn. vol. 41, issue 10 (2005).

[7] D. Suess, T. Schrefl, S. Fahler, M. Kirschner, G. Hrkac, F. Dorfbauer, and J. Fiedler, “Exchange Spring Media for Perpendicular Recording”, Appl. Phys. Lett., vol. 87, p. 012 504, (2005).

[8] W. F. Brown, “Virtues and weaknesses of the domain concept”, Rev. Mod. Phys., vol. 17, no. 15, (1945).

[9] A. Aharoni, “Reduction in coercive force caused by a certain type of imperfection”, Phys. Rev., vol. 119, p. 127, (1960).

[10] H. Kronmuller and D. Goll, “Micromagnetic Theory of The Pinning of Domain Walls at Phase Boundaries”, Physica B 319 p. 122-126 (2002).

[11] P. N. Loxley and R. L. Stamps, “Theory of Domain Wall Nucleation in A Two Section Magnetic Wire”, IEEE Trans. Magn. vol. 37, no. 4 (2001).

[12] A. Yu. Dobin and H. J. Richter, “Domain Wall Assisted Magnetic Recording”, Appl. Phys. Lett. 90, 062512 (2006).

[13] A. Yu. Dobin and H. J. Richter, “Domain Wall Assisted Magnetic Recording (invited)”, J. Appl. Phys. 101, 09K108 (2007).

[14] D. Suess, T. Schrefl, S. Fahler, M. Kirschner, G. Hrkac, F. Dorfbauer, and J. Fidler, “Exchange Spring Media for Perpendicular Recording”, Appl. Phys. Lett. 87, 012504 (2005).

[15] D. Suess, J. Lee, J. Fidler, T. Schrefl, “Exchange-coupled Perpendicular Media”, J. Magn. Magn. Mater. 250 p.12 (2002).

[16] H. J. Richter, G. Choe, and B. D. Terris, “Recording Behavior of Exchange Coupled Media”, IEEE Trans. Magn. vol. 47, no. 12 (2011).

[17] M. H. Kryder, E. C. Gage, T. W. MacDaniel, W.A. Challener, R. E. Rottmayer, G. Ju, Y. T. Hsia, and M. F. Erden, “Heat Assisted Magnetic Recording”, Proceedings of The IEEE, vol. 96, no. 11, (2008).

[18] W. A Challener, C. Peng, A.V. Itagi, D. Karns, W. Peng, Y. Peng, X. Yang, X. Zhu, N. J. Gokemeijer, Y. T. Hsia, G. Ju, et. al., “Heat-assisted Magnetic Recording by A Near-Field Transducer with Efficient Optical Energy Transfer”, Nature Photonics 3, 220-224 (2009).

[19] R. F. L Evans, R. W. Chantrell, U. Nowak, A. Lyberatos, and H. J. Richter, "Thermally Induced Error: Density Limit for Magnetic Data Storage", Appl. Phys. Lett. 100, 201402 (2012).

[20] Seagate 2016 TMRC Talk Stanford University

[21] D. Weller and A. Moser, "Thermal Effect Limits in Ultrahigh Density Magnetic Recording", IEEE Trans. Magn. 35(6) p. 4423-4439 (1999).

[22] H. N. Bertram, "Theory of Magnetic Recording", Cambridge University Press.

[23] X. Wang and H. N. Bertram, "Simple Transition Parameter Expression including Grain Size and Intergranular Exchange", J. Appl. Phys. vol. 93, p. 7005 (2003).

[24] X. Wang, B. Valcu, and N-H Yeh, "Transition Width Limit in Magnetic Recording" Appl. Phys. Lett. 94, 202508 (2009).

[25] B. F. Valcu and N-H Yeh, "Jitter in a Voronoi Pattern Media-Effect of Grain Size Distribution and Reader Width", IEEE Trans. Magn. vol. 46 issue:6 (2010).

[26] R. F. L Evans, R. W. Chantrell, U. Nowak, A. Lyberatos, and H.-J. Richter, "Thermally Induced Error: Density Limit for Magnetic Data Storage", Appl. Phys. Lett. 100, 102402 (2012).

[27] T. Thomson, G. Hu, and B. D Terris, "Intrinsic Distribution of Magnetic Anisotropy in Thin Films Probed by Patterned Nanostructures", Phys. Rev. Lett. 96, 257204 (2006).

[28] C. Rong, D. Li, V. Nandwana, N. Poudyal, Y. Ding, Z. Wang, H. Zeng, and J. Liu, "Size-Dependent Chemical and Magnetic Ordering in L10-FePt Nanoparticles", Adv. Mater., vol. 18, no. 22, pp. 2984-2988, (2006).

[29] A. Lyberatos, D. Weller, G. J. Parker, and B.C. Stipe, “Size Dependence of the Curie Temperature of L10-FePt nanoparticles”, J. Appl. Phys. 112, 113915 (2012).

[30] H. N. Bertram, M. Marrow, J. Ohno, and J. K. Wolf, “Analysis of DC noise in Thin Film Media”, IEEE Trans. Magn. vol. 40, no. 4, (2004).

[31] T. Klemmer, D. Hoydick, H. Okumura, B. Zhang, and W. A. Soffa, “Magnetic Hardening and Coercivity Mechanisms in L10 Ordered FePd Ferromagnets”, Scripta Metallurgica et Materialia, vol. 33, pp. 1793-1805, (1995).

[32] Y. Peng et al., “Heat assisted magnetic recording on high anisotropy nanocomposite media,” in Proc. IEEE Conf. Nanotechnol. (NANO), pp. 603–604 (2008).

[33] T. Klemmer, Y. Peng, X. Wu, and G. Ju, “Materials processing for high anisotropy L10 granular media,” IEEE Trans. Magn., vol. 45, no. 2, pp. 845–849, (2009).

[34] Y. Kubota et al., “Thermal design for heat assisted magnetic recording media,” in Proc. TMRC, paper D-2, (2014).

[35] R. Acharya et al., “Challenges and recent development of heat assisted magnetic recording media,” in Proc. TMRC, paper D-3, (2014).

[36] D. Weller, O. Mosendz, G. Parker, S. Pisana, and T. Santos, “L10 FePtX–Y media for heat-assisted magnetic recording,” Phys. Status Solidi A, vol. 210, no. 7, pp. 1245–1260, (2013).

[37] O. Mosendz, S. Pisana, J. W. Reiner, B. Stipe, and D. Weller, “Ultra-high Coercivity Small-grain FePt Media for Thermally Assisted Recording (invited)”, J. Appl. Phys. 111 07B729 (2012).

[38] G. Ju, Y. Peng, E.K.C. Chang, Y. Ding, A. Q. Wu, X. Zhu, Y. Kubata, T. J. Klemmer, H. Amini, and L. Gao et. al, "High Density Heat-Assisted Magnetic Recording Media and Advanced Characterization — Progress and Challenges", IEEE Trans. Magn. vol. 51, no. 11 (2015).

[39] L. Landau and E. Lifshits, "On the Theory of the Dispersion of Magnetic Permeability in Ferromagnetic Bodies," Phys. Zeitsch. Der Sow., vol. 8, pp. 153–169, 1935. Reprinted in Ukr. J. Phys., vol. 53, Special Issue, (2008).

[40] W. F. Brown, Jr. 1963 Micro-magnetics 18 John Wiley & Sons, New York.

[41] W. F. Brown, "Thermal Fluctuations of A Single-domain Particle", Phys. Rev., vol. 130, pp. 1677-1686 (1963).

[42] P-W Huang, "Micromagnetic Study of Heat Assisted magnetic Recording Using Renormalized Media Cells", A Dissertation of University of Minnesota (2014).

[43] R. H. Victora and P-W Huang, "Simulation of Heat-Assisted Magnetic Recording Using Renormalized Media Cells", IEEE Trans. Magn. vol. 49, no. 2 (2013).

[44] S. K. Ma, "Modern Theory of Critical Phenomena" Reading, MA: Benjamin, (1976).

[45] R. F. L Evans, "Atomistic Modelling of Nanogranular Magnetic Materials", A Dissertation of University of York, (2008).

[46] X. Feng, and P. B. Visscher, "Coarse-graining Laudau-Lifshitz Damping", J. Appl. Phys., vol. 89, pp. 6988-6990, (2001)

[47] Y. Jiao, Z. Liu and R. H. Victora, "Renormalized Anisotropy Exchange for Representing Heat Assisted Magnetic Recording Media", J. Appl. Phys. 117(17), 17E317-1 (2015).

[48] N-H Yeh, Z. Zhang, and P. Steiner, “From Component SNR to System SNR”, (2012).

[49] C. Rea, P. Subedi, H. Zhou, D. Saunders, M. Cordle, P-L Lu, S. Granz, P. J. Czoschke, S. Hernandez, J. Jury et. al., “High Track Pitch Capability for HAMR Recording”, IEEE Trans. Magn. vol. 53, no. 2, (2017).

[50] I. Ozgunes and W. R. Eppler, “Synchronization-free Dibit Response Extraction From PRBS Waveforms”, IEEE Trans. Magn. vol. 39, issue 5 (2003).

[51] M. P Sharrock, “Time Dependence of Switching Fields in Magnetic Recording Media (invited)”, J. Appl. Phys. 76 (10), 15 (1994).

[52] O. Hovorka, S. Devos, Q. Coopman, W. J. Fan, C. J. Aas, R. F. L. Evans, X. Chen, G. Ju, and R. W. Chantrell, “Distribution of Switching Fields in Magnetic Granular Materials”, Appl. Phys. Lett. 101, 052406 (2012).

[53] A. Chernyshov, T. Le, B. Livshitz, O. Mryasov, C. Miller, R. Acharya, and D. Treves, “Measurement of Curie Temperature Distribution Relevant to Heat Assisted Magnetic Recording”, J. Appl. Physics 117, 17D111 (2015).

[54] S. Pisana, S. Jain, J. W. Reiner, G. J. Parker, C. C. Poon, O. Hellwig and B. C. Stipe, “Measurement of The Curie Temperature Distribution in FePt Granular Magnetic Media”, Appl. Phys. Lett. 104, 162407 (2014).

[55] H. Li and J-G Zhu, “Understanding the Impact of T_c and H_k Variation on Signal-to-Noise Ratio in Heat-assisted Magnetic Recording”, J. Appl. Phys. 115 , 17B744 (2014).

[56] P-W Huang and R. H. Victora, “Approaching the Grain-Size Limit for Jitter Using FeRh/FePt in Heat-Assisted Magnetic Recording”, IEEE Trans. Magn. vol. 50 issue: 11 (2014).

[57] S. Wang, M. Mallary and R. H. Victora, “Thermal Switching Distribution of FePt Grains Through Atomistic Simulation”, IEEE Trans. Magn. vol. 50 issue 11 (2014).

[58] Z. Liu, Y. Jiao, and R. H. Victora, “Composite Media for High Density Heat Assisted Magnetic Recording”, Appl. Phys. Lett. 108, 232402 (2016).

[59] S. M. Morgan, H. Sohn, and R. H. Victora, “Use of trapezoidal waves and complementary static fields incident on magnetic nanoparticles to induce magnetic hyperthermia for therapeutic cancer treatment,” J. Appl. Phys. 109, 07B305, 2011.

[60] A. Chernyshov, D. Treves, T. Le, F. Zong, A. Ajan, and R. Acharya, “Measurement of FePt Thermal Properties Relevant to Heat-assisted Magnetic Recording”, J. Appl. Phys. 115, 17B735 (2014).

[61] J.-U. Thiele, S. Maat, and E. Fullerton, “FeRh/FePt Exchange Spring Films for Thermally Assisted Magnetic Recording Media”, Appl Phys. Lett. 82, 2859 (2003).

[62] R. H. Victora, S. Wang, P-W Huang, and A. Ghoreyshi, “Noise Mitigation in Granular and Bit-Patterned Media for HAMR”, IEEE Trans. Magn. vol. 51, no. 4 (2015).

[63] B. H. Grier, G. Shirane, and S. A. Werner, “Magnetic Excitations in Chromium. II,” Phys. Rev. B, vol. 31, no. 5, pp. 2892–2901, 1985

[64] H. Zabel, “Magnetism of Chromium at Surfaces, at Interfaces and in Thin Films,” J. Phys., Condens. Matter, vol. 11, no. 48, pp. 9303–9346, 1999

[65] D. Suess and T. Schrefl, “Breaking The Thermally Induced Write Error in Heat Assisted Recording by Using Low and High Tc Materials”, Appl. Phys. Lett. 102, 162405 (2013).

[66] Z. Liu and R. H. Victora, “Composite Structure With Superparamagnetic Writing Layer for Heat-Assisted Magnetic Recording”, IEEE Trans. Magn. vol. 52, issue 7 (2016).

[67] P. Huang, X. Chen, and R. H. Victora, “Time Dependence of Magnetic Anisotropy at Finite Temperature for Homogeneous and Composite Media,” IEEE Trans. Magn., vol 48, no. 11, (2012).

[68] N. Wang, K. Komvopoulos, F. Rose, and B. Marchon, “Structural Stability of Hydrogenated Amorphous Carbon Overcoats Used in Heat-assisted Magnetic Recording Investigated by Rapid Thermal Annealing”, J. Appl. Physics 113, 083517 (2013).

[69] W. A. Challener, C. Peng, A. V. Itagi, D. Karns, W. Peng, Y. Peng, X. Yang, X. Zhu, N. J. Gokemeijer, Y.-T. Hsia, G. Ju, et al, “Heat-assisted Magnetic Recording by A Near-Field Transducer with Efficient Optical Energy Transfer”, Nature Photonics 3, 220-224 (2009).

[70] N. Zhou, X. Xu, A. T. Hammack, B. C. Stipe, K. Gao, W. Scholz and E. C. Gage, “Plasmonic Near-Field Transducer for Heat-assisted Magnetic Recording”, Nanophotonics, 3(3):141-155 (2014).

[71] J.-U. Thiele, K. R. Coffey, M. F. Toney, J. A. Hedstrom, and A. J. Kellock, “Temperature Dependent Magnetic Properties of Highly Chemically Ordered $Fe_{50-x}Ni_xPt_{45}$ $L1_0$ Films”, J. Appl. Phys. 91, 6595 (2002).

[72] Y. Jiao, Y. Wang, and R. H. Victora, “A Study of SNR and BER in Heat Assisted Magnetic Recording (HAMR)”, IEEE Trans. Magn. vol. 51, no. 11, 7156123 (2015).

[73] C. E. Shannon, “Communication Theory of Secrecy Systems”, Bell Syst. Tech. J., vol. 27, no. 3, pp. 379-423 (1948).

[74] J. Moon, and W. Zeng, “Equalization for Maximum Likelihood Detectors”, IEEE Trans. Magn. vol. 31, issue 2 (1995).

[75] Y. Wang, M. F. Erden and R. H. Victora, “Novel System Design for Readback at 10 Terabits Per Square Inch Areal Density”, IEEE Magn. Lett. *IEEE Magn. Lett*, vol. 3, (2012).

[76] J. Caroselli, S. A. Altekar, P. McEwen, and J. K. Wolf, “Improved Detection for Magnetic Recording Systems with Media Noise”, *IEEE Trans. Magn*., vol. 33, no. 5, pp. 2779–2781, Sep. 1997.

[77] X. Wang, B. Valcu and N-H Yeh, “Switching field distribution and transition width in energy assisted magnetic recording”, Appl. Phys. Lett. 94 202508 (2009).

[78] Z. Liu and R. H. Victora, “Exchange Coupled Composite Media for Heat Assisted Magnetic Recording”, AIP Advances 7, 056516 (2017).

[79] H. N. Bertram and B. Lengsfield, “Energy Barriers in Composite Media Grains”, IEEE Trans. Magn. vol. 43, issue 6, (2007)

[80] D. Suess, T. Schrefl, S.Fahler, M. Kirschner, G. Hrkac, F. Dorfbauer, and J. Fidler, “Exchange Spring Media for Perpendicular Recording”, Appl. Phys. Lett. 87, 012504 (2005).

[81] R. Wood, M. Williams, A. Kavcic, and J. Miles, “The Feasibility of Magnetic Recording at 10 Terabits Per Square Inch on Conventional Media”, IEEE Trans. Magn. vol. 45, issue 2, (2009).

[82] R. H. Victora and X. Shen, “Composite Media for Perpendicular Magnetic Recording”, IEEE Trans. Magn. vol. 41, no. 2, (2005).

[83] S. M. Morgan, H. Sohn, and R. H. Victora, “Use of Trapezoidal Waves and Complementary Static Fields Incident on Magnetic Nanoparticles to Induce Magnetic Hyperthermia for Therapeutic Cancer Treatment”, J. Appl. Phys., vol 109, no. 7 (2011).

[84] Z. Liu, P.-W. Huang, G. Ju and R. H. Victora, “Thermal Switching Probability Distribution of L10 FePt for Heat Assisted Magnetic Recording”, Appl. Phys. Lett. 110, 182405 (2017).